ABSTRACT

Title of Document: HIGH-FIELD THZ GENERATION AND BEAM CHARACTERIZATION WITH LASER BASED INTENSE THZ SOURCES

Yung-Jun Yoo, Doctor of Philosophy, 2018

Directed By: Professor Ki-Yong Kim
Institute for Research in Electronics and Applied Physics

The main topic of this dissertation is about the generation of intense terahertz (THz) pulses with field strengths up to tens of MV/cm and their characterization with energy, pulse duration, and spot size measurements. As a strong THz source, we used two-color laser mixing in air, which can produce coherent, high energy (> μJ), broadband (0.01~100 THz) THz radiation. In this scheme, 800-nm, 1-kHz, 30-fs laser pulses are weakly focused onto a BBO (Beta Barium Borate) crystal to generate the 2nd harmonic (400 nm) pulses. The original (800 nm) and second harmonic (400 nm) pulses are focused together to generate plasma filaments in air, and this works as a broadband source of THz radiation.

In particular, we have studied THz energy scaling with various focal length conditions and input laser energies up to 10 mJ. With high laser input energy, the THz output energy does not simply increase but rather saturates or even decreases. We find that this occurs due to plasma-induced laser defocusing, which prohibits efficient laser

energy coupling into the plasma. We have overcome this saturation effect by increasing the plasma volume in the longitudinal or transverse direction. At a high repetition rate (1 kHz), we have achieved 2.6 μJ of THz energy with 10 mJ laser energy by elongating the plasma length (~7 cm). This provides a conversion efficiency of 2.6×10^{-4} from optical to THz energy. Also, at a low repetition rate (10 Hz) with high laser input energy (~50 mJ), we increased the plasma volume in the transverse direction by generating a 2-dimensional plasma sheet and obtained 31 μJ of THz energy.

We have also investigated THz generation from two-color laser filamentation in different types of gases (room air, nitrogen, oxygen, carbon dioxide, helium, argon, krypton, and xenon) at various gas pressures. By elongating the plasma length in a long gas cell, we have achieved laser-to-THz conversion efficiency of ~0.1%, one order of magnitude higher than a typical value (0.01%) obtained in two-color laser focusing in air.

To obtain strong THz fields, we have performed tight refocusing of the emitted THz radiation. Previously, it was speculated that a large plasma volume could produce more THz energy but not necessarily assure strong THz field strengths because of its ineffective refocusing of the emitted THz radiation. Contrary to the concern, we have achieved a small THz spot size near its diffraction limit (~40 μm) even with long filamentation. This gives THz field strengths up to ~30 MV/cm in our gas cell experiment.

We have also studied various THz detection methods to cover a broad frequency range of THz radiation. To measure THz energy, we used broadband thermopile and pyro-electric detectors. We have also developed a real-time lock-in

imaging technique to characterize frequency-dependent THz radiation profiles by using an uncooled microbolometer along with THz bandpass filters. We have characterized THz waveforms and spectra with electro-optic (EO) sampling and/or Fourier Transform Infrared Spectroscopy (FTIR). We find that our THz source produces extremely broad electromagnetic (EM) radiation ranging from radio-micro waves to infrared frequencies. This source can be a useful tool to study broadband linear and nonlinear THz spectroscopy.

HIGH-FIELD THZ GENERATION AND BEAM CHARACTERIZATION WITH LASER BASED INTENSE THZ SOURCES

By

Yung-Jun Yoo

Dissertation submitted to the Faculty of the Graduate School of the
University of Maryland, College Park, in partial fulfillment
of the requirements for the degree of
[Doctor of Philosophy]
[2018]

Advisory Committee:
Professor Howard M. Milchberg, Chair
Professor Ki-Yong Kim, Co-chair
Professor Phillip Sprangle
Professor Julius Goldhar
Professor Bong-Tae Han

Dedication

This work is dedicated to my wife Hyunji.

Acknowledgements

First, I would like to give special thanks to my advisor, Kiyong Kim. This dissertation work would not be possible without his mentorship. He has always encouraged me to try many research ideas and also provided a wonderful research environment throughout my Ph.D. years. It was my pleasure time to work with him.

Prof. Howard Milchberg deserves acknowledgment for his insight and efforts in our collaboration. Furthermore, as a co-advisor, he has also guided me to achieve this work as well as provide many administrative help throughout years.

I would also like to express my gratitude to my co-workers, specially Donghoon, Zheqiang, Yan, and also our previous lab members, Taek Il, Yong Sing, Jeff, Vijay, Donggyu, Dongwen, Inhyuk and Dogeun, for helpful discussions and comments in many experiments.

Finally, I want to mention all my loving family here. Without their care, sacrifice, and understanding, I couldn't finish this dissertation successfully. Special thanks to my wife, Hyunji. I also am very grateful to my parents, parents in law.

Table of Contents

List of Tables

List of Figures

Chapter 1 : Introduction and overview

1.1 Introduction to terahertz (THz) science

1.1.1 THz science

Terahertz (1 THz = 10^{12} Hz) science is a study of a specific region of the electromagnetic spectrum sandwiched between the infrared and microwave frequencies. As shown in Fig. 1.1, THz radiation, so called T-ray, is typically referred to the radiation whose frequency lies between 0.1~10 THz with the corresponding wavelength of 30 μm ~ 3 mm. For example, 1 THz of frequency corresponds to the wavelength of 300 μm, period of 1 picosecond (1 ps = 1 × 10^{-12} s), and 4.1 meV in photon energy. Due to the difficulty of detecting and generating radiation at those frequencies, THz has been believed as the most undeveloped region of the electromagnetic spectrum and traditionally called as the THz gap. [6][7]. To bridge the gap between the optical and microwave regions, intensive research has been conducted over many decades, in particular to generate, detect, and characterize THz radiation more efficiently.

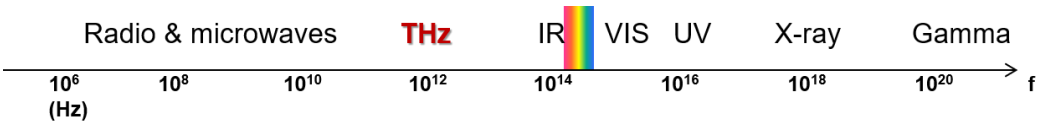

Figure 1.1 Electromagnetic radiation from radio waves to X-rays in wavelength and frequency (adapted and redesigned from BRLABS [8]).

1.1.2 THz application

THz radiation has attracted a lot of interest for various potential applications both in science and technology [9]. Especially, many scientists are interested in characterizing transmission/absorption spectra of materials, and this can be achieved with THz time domain spectroscopy (TDS). This TDS technique is useful for measuring material's own properties such as dielectric coefficient or non-linear refractive index as well as absorption spectrum itself [10]. In industry, a lot of engineers have interests of using THz imaging techniques for non-destructive probing and testing. THz radiation can penetrate through non-polar materials such as paper, cloth and plastics without ionizing the materials. Therefore, THz imaging can be used for detection of weapons or explosives hidden inside envelopes or clothes for security purposes [13] [14]. Also, in these days, THz radiation has been considered as one of solutions to resolve various problems in future wireless communication. [3] At THz frequencies, massive and secure communication can be possible, and that can be used for a lot of wireless applications such as uncompressed broadcasting, military communication and machine to machine (M to M) communication among small devices in Internet of the Things (IOT). [3] As it is shown from the examples stated above, the development of intense THz sources is one of crucial parts in implementing applications for many academic and industrial fields [19–23].

1.1.3 Conventional laser based techniques for high-field THz pulse generation

Recently high field THz science has gained a lot of interest among scientists and engineers. However, there have not been many high field THz sources. However,

there has been a lot of researches in developing tabletop high field (~MV/cm) THz sources by utilizing high power femtosecond lasers [1-2]. Examples include tilted pulse front generation in lithium niobate ($LiNbO_3$) crystals [4] and optical rectification in organic crystals [5], which are two widely used techniques in the strong THz field science community.

First, the THz generation scheme using tilted pulse fronts inside $LiNbO_3$ was proposed by Hebling in 2002. This method has been widely used among many THz scientists because it can deliver high conversion efficiency (~10^{-3}) with favorable phase-matching condition, and this has been reported to generate high energy (> 50 μJ) single cycle THz pulses [17]. Figure 1.2 shows a typical setup diagram of tilted wave front generation. In this method, a femtosecond laser pulse illuminates onto a $LiNbO_3$ prism. Since the velocity of the optical beam is faster than that of THz pulse in $LiNbO_3$, for efficient THz generation, the pump pulse front needs to be tilted by an angle of γ to match the velocity ($v_p^{gr} cos\gamma = v_{THz}$). Here, the tilt angle γ can be implemented by using stacked mirrors or a grating, and is calculated as

$$tan\,\gamma = \frac{m\lambda_0 p}{n_p^{gr}\beta_1 cos\theta_d}. \quad (1\text{-}1)$$

In this equation, m is the diffraction order, λ_0 is the central wavelength of the optical pump beam, and p is the groove density of the grating used for tilting the pulse front. In the denominator, n_p^{gr} is the group refractive index of $LiNbO_3$ at the optical pump wavelength, β_1 is the magnification factor of the grating image onto the crystal, and θ_d is the diffraction angle. Although this method can deliver high output THz energy with high efficiency, this method is not suitable for high field strength (> 10 MV/cm) due to following limitations. Since the pump beam passes through the prism,

it is hard to achieve a femtosecond level of the pulse duration due to dispersion inside the crystal. Also, because of THz absorption inside the crystal and phase matching condition, only low frequency components (< 3 THz) can be generated, and this provides large transform-limited THz spot sizes of > 100 μm [4].

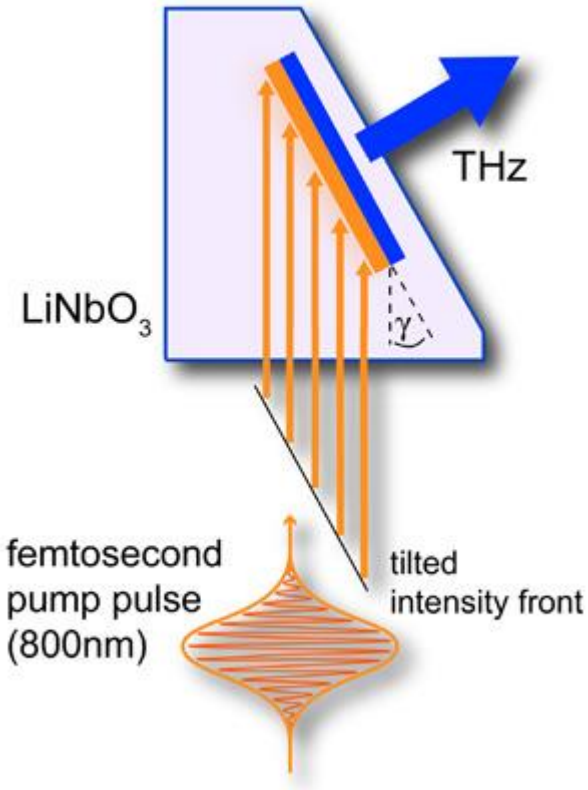

Figure 1.2 THz generation by a tilted pulse front inside a $LiNbO_3$ prism illuminated by a femtosecond laser pulse. (adapted from mpsd-cmd [11])

The other method widely used with femtosecond lasers is optical rectification in non-centrosymmetric organic crystals such as DAST [5]. The process of THz pulse generation in those crystals can be explained by the second order nonlinearity, which is described by the following equation [7] [28],

$$P_2^{nl} = \chi_2 \frac{E_0^2}{2}[\cos(\omega_1 - \omega_2)t + \cos(\omega_1 + \omega_2)t] \quad (1\text{-}2)$$

Here, the difference frequency ($\omega_1 - \omega_2$) in the first term corresponds to the THz frequency which is much lower than the original pump frequency (ω_1, ω_2), and this also corresponds to the rectified frequency of the input pulse envelope, thus called optical rectification. In many previous researches, this mechanism has been widely used along with a non-centrosymmetric crystal such as ZnTe, which is favorably phased matched at 800 nm. But this method provides two major limitations, low conversion efficiencies (~10^{-5}) and narrow bandwidths (<3 THz).

The conversion efficiency can be greatly enhanced when an organic crystal is illuminated by near infra-red (IR) femtosecond laser pulses. With more favorable phase matching in the near IR, much higher conversion efficiency (>10^{-3}) can be achieved with organic crystals.

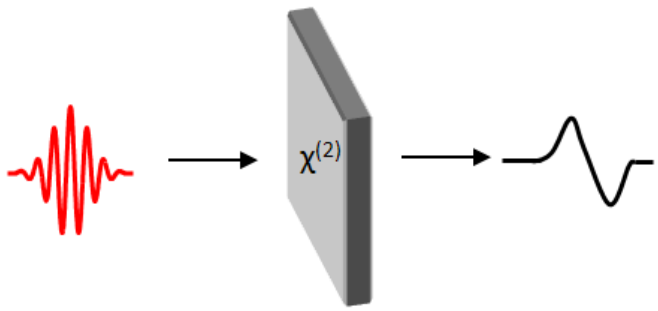

Figure 1.3 THz generation by an ultrashort laser pulse in a nonlinear crystal via optical rectification.

However, this method needs an OPA (Operational Parametric Amplifier) to convert the laser wavelength to the near IR. Here the output IR energy is considerably lower than the original laser energy. Also, due to strong THz absorption inside the crystal, this method has an inherent limitation of the bandwidth (<5 THz). Although, THz generation from the optical rectification process is considered as the simplest way

to generate intense THz pulses, it is not suitable for applications requiring short pulse duration and broadband THz sources. Also for this, development of proper materials which have effective nonlinear coefficients is a key issue.

1.2 THz generation using two-color laser mixing in plasma

Compared to tilted pulse front generation in $LiNbO_3$ or optical rectification in nonlinear organic crystals, two-color laser mixing provides intense, short, and broadband THz pulses with moderate conversion efficiency (~10^{-4})[91]. For example, tilted pulse front generation in a $LiNbO_3$ prism provides high energy, high efficiency radiation, but the radiation spectrum reaches only up to 1.5 THz due to THz absorption and limited phase matching inside the crystal. Because of this, it is challenging to obtain small THz spot sizes (<100 μm). Also femtosecond-level THz pulse durations are hard to achieve. So high THz fields of tens of MV/cm are not easily achievable with the tilted pulse front scheme even with high output THz energy [29]. Similar limitations are also applied to organic-crystal-based optical rectification. On the other hand, two-color laser mixing is reported to provide ultra-broadband radiation up to 200 THz, short pulse durations (~100 fs), small spot sizes (~40 μm), and these can lead to high field strengths up to tens of MV/cm [93]. As high field THz sources, these provide attractive features for nonlinear THz study, THz imaging application and broadband spectroscopic studies. Therefore strong THz field generation via two-color laser mixing in air has attracted considerable attention from many scientists and engineers [30–54].

1.2.1 Mechanisms of two color photoionization

THz generation from two-color photoionization was first reported by D. J. Cook and R. Hochstrasser in 2000 [31]. First this phenomenon was interpreted as a four-wave mixing process in air, but this model did not provide any microscopic origin of such a strong nonlinearity, and therefore it could not explain strong THz radiation as the

output. In 2008, a plasma current model was proposed by K. Y. Kim to explain the THz generation process from two-color photoionization [47]. In this model, when a strong laser field is applied, bound electrons tunnel out and become freed. These freed electrons oscillate at the laser frequencies, and also drift away from their parent ions at velocities determined by the laser field amplitudes and the relative phase between the two-color laser fields. When a single-color laser field is applied, the electron drift motion remains symmetric (a half of electrons drift up, and the other half of electrons drift down) and the net current caused by the electrons vanishes. However, when two-laser fields are applied with the right phase, the symmetry breaks and produce a net directional quasi-DC current. As this current surge occurs on the timescale of the applied laser pulse duration, for femtosecond lasers, it can generate electromagnetic radiation at THz frequencies [47].

1.2.2 Microscopic view of THz radiation in two-color mixing

To explain the THz generation mechanism in two-color laser mixing, two different models have been proposed—four-wave mixing [31] and plasma current model [34]. First, the four wave mixing process can be explained by the third order nonlinearity in air $\chi_3(\Omega = \omega + \omega - 2\omega)$ [31]. On the other hand, one can view the same process as a photocurrent surge, in which a quasi-DC directional current arises from symmetry-broken electron drift motion.

In this chapter, we introduce and describe a theoretical background of the photocurrent model [47]. If two-color laser field (original and its second harmonic) are mixed together at the focus, the combined laser field can be expressed as

$$E_L = E_{\omega e}(t)\cos(\omega t) + E_{2\omega}(t)\cos(2\omega t + \theta)\,. \tag{1-3}$$

Here, $E_\omega(t)$ and $E_{2\omega}(t)$ are the amplitudes of the fundamental and the second harmonic fields, respectively, θ is the relative phase between $E_\omega(t)$ and $E_{2\omega}(t)$ at the focus. At strong laser intensities (around 10^{14} to 10^{15} W/cm^2), tunneling ionization becomes a dominant ionization process in air. In this regime, we use an Ammosov-Delone-Krainov (ADK) model to characterize the ionization rate [56]. Although the ADK model has been mostly used to calculate the tunneling ionization rate for noble gases such as He or Ne, it is also applicable to structureless atomic-like molecules such as N_2 which is the primary component of the air.

For an electron density given by the ADK ionization rate, the local plasma current density can be calculated from [49]

$$J(t) = -\int e v_d(t,t')dN_e(t')\,, \tag{1-4}$$

where $dN(t')$ is the density of free electrons produced by the laser field in the interval between t' and $t' + dt'$, and $v_d(t, t')$ is the drift velocity of those electrons at t.

Here, the drift velocity $v_d(t, t')$ can be calculated as follows when the electron is freed at phase ϕ.

$$v_d = \frac{eE_\omega}{m_e\omega}\sin\phi + \frac{E_{2\omega}}{2m_e\omega}\sin(2\phi + \theta) \tag{1-5}$$

where m_e is the electron mass.

Figure 1.4 shows a better explanation of the mechanism. The left column shows the optical waveform when the relative phase between the fundamental (800 nm) and the second harmonic (400 nm) is zero (θ = 0), and the right column is the case with $\theta = \frac{\pi}{2}$. Here we assume that the intensity of the second harmonic is 20% of the

fundamental intensity. Now the lower parts show the trajectories of electrons freed at four different phases. In general, they oscillate and drift simultaneously. Once the electron is liberated, the electric field determines the drift velocity which is given by Eq. (1-5). From the plot, when $\theta = 0$, we can see two electrons drift up and two electrons drift down with an equal and opposite current. Therefore, the net current becomes zero and no THz radiation would be generated. This situation is similar to the case that the single-color field is applied, and this is why single-color ionization is not efficient for THz generation. However, when $\theta=\frac{\pi}{2}$, this symmetry breaks. Now more electrons drift up, and the net current becomes no more zero. This directional current surge occurs on the timescale of the laser pulse duration (or photoionization) and emits THz radiation ($E_{\mathrm{THz}} \propto dJ(t)/dt$) in the far field [47–50]. For a laser pulse duration of <100 fs, this process can generate electromagnetic radiation at 1-100 THz.

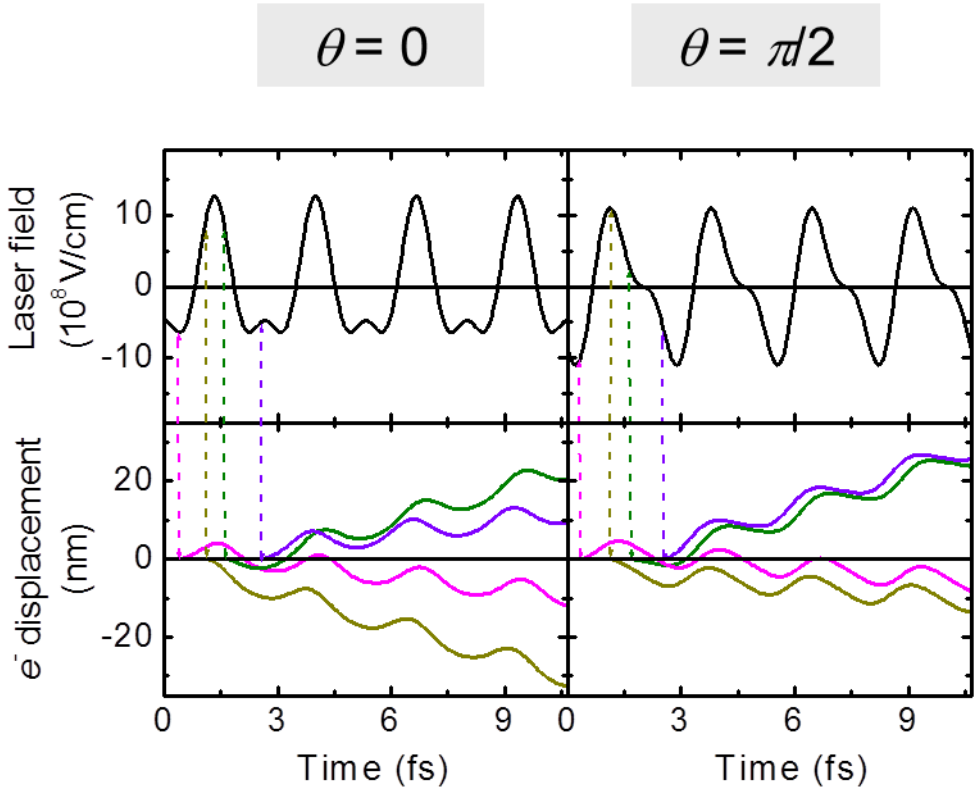

Figure 1.4 Simulation results of free electron drifts for two different relative phases. For simulation parameter, λ = 800 nm, 400 nm with intensity of I_{ω} = 10^{15} W/cm^2 and $I_{2\omega}$ = 2 × 10^{14} W/cm^2 are assumed.

1.3 Real-time THz beam profiling and imaging

Conventionally, THz radiation is detected by a pump-probe scanning method involving electro-optic (EO) sampling or direct measurements using pyro-electric/thermopile detectors. In both schemes, only 1-D information can be obtained in a single measurement. Therefore, with these methods, we need additional scanning to get 2-D information such as beam profiles or images. In general, this scanning usually takes a long time and the obtained data is often vulnerable to shot-to-shot laser

fluctuations. To resolve this problem, 2-D focal plane arrays such as microbolometers have been developed and used for beam profiling and imaging in the longwave length IR regime (7~14 μm).

For THz beam profiling, the microbolometer is placed near the THz focal spot (see Fig. 1.5) and scanned along the beam direction (z-axis). For example, Figure 1.5 shows a series of THz profiles obtained before and after the focal spot with an additional germanium (Ge) filter placed in front of the camera. Those profiles also represent THz emission profiles just after the plasma filament owing to f_1-and-f_2 relay imaging (here, $f_1 = f_2 = 6$ inches). Note that here the object plane does not exactly match with the camera displacement because of $f_1 + f_2 \neq 12$ inches in our case. Nonetheless, the scanning shows how the THz radiation profile varies as it propagates away from the filament. Overall, the profiles are slightly asymmetric due to uncompensated spatial chirps in the laser beam, as observed in our previous report [52].

At $z > 6$ mm, it shows conical THz emission profiles, consistent with previous observations [52, 76, 89-90]. Recent study shows that the conical structure, in general, originates from a combination of Cherenkov-type radiation and off-axis phase matching [52, 89]. Cherenkov-type phase matching arises when the radiation source (filament) moves faster than the speed of THz radiation [89]. Off-axis phase matching occurs when the filament length exceeds the dephasing length, over which the local THz source phase remains at $0 \sim \pi$, and all radiation components from the line source constructively interfere in the off-axis direction [52]. For relatively short filaments, typically less than ~20 mm as in this experiment, Cherenkov-type phase matching is dominant and can explain the conical emission shown in Fig1.5. It is interesting to note

that there is a bright spot surrounded by conical emission at z = -10 mm and -6 mm, but not in the opposite side at z = 6 mm and 10 mm. This bright spot was also previously observed [52] and is believed to be an artifact induced by faulty imaging. In the case of z = -10 mm and -6 mm, the object plane is selected prior to the source, and the profiles shown in Fig. 1.5 do not represent real radiation profiles. This kind of artifact is commonly observed in optical imaging of filaments

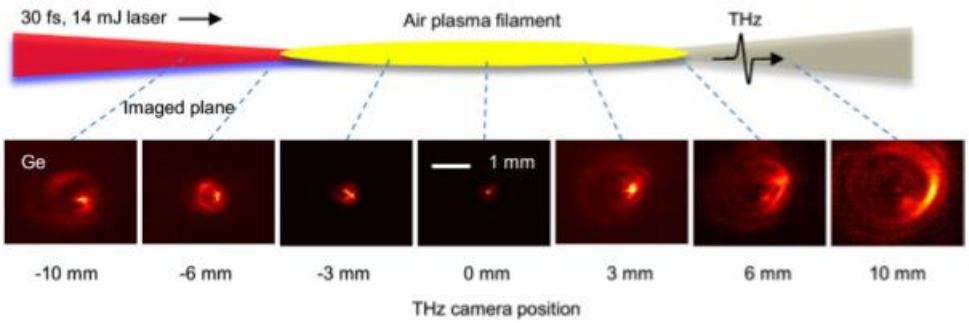

Figure 1.5 THz beam profiles obtained by a microbolometer camera at -10mm, -6mm, -3mm, 0mm, 3mm, 6mm, and 10mm distances away from its best focus with an additional Ge transmission (<10 THz) filter placed in front of the camera.

1.4 Summary of dissertation

The main focus of this dissertation is intense terahertz (THz) field generation using two-color laser mixing in air. This chapter introduces THz science and conventional tabletop high field THz sources, and also describes the photocurrent model that explains a microscopic mechanism of THz generation in two-color laser mixing in a gas.

In chapter 2, a method to generate and characterize high field THz radiation at a high repetition rate (1 kHz) is presented. For the generation of high field THz pulses, a combination of long filamentation and tight refocusing has been applied experimentally. To characterize THz field strengths, three essential parameters (THz energy, THz beam spot size, and THz pulse duration) are measured by various methods. By combining all these, we verify a maximum THz field strength of 16 MV/cm at the focus.

In chapter 3, a new scheme to generate scalable THz radiation is presented. In this method, we perform two-color laser mixing via cylindrical focusing, which creates a 2-D plasma sheet as a scalable THz source. We compare the generated output THz energy with cylindrical vs. spherical focusing at laser input energy up to 50 mJ. Here, we verify that we can avoid a saturation effect caused by plasma-induced laser defocusing, and scalable THz output energy can be obtained with cylindrical focusing.

Chapter 4 studies two-color laser filamentation in various types of gases and their effects on THz generation. In particular, we investigate high-field THz generation by long filamentation inside a gas tube filled with air, Ar, N_2, O_2, CO_2, He, Ne, Kr, or Xe at various gas pressures. Surprisingly, we find that the output THz radiation peaks at very low pressures. We explain this effect with a simple beam walk-off model. With low-pressure Ar, we have achieved laser-to-THz conversion efficiency of >0.1%, which is one order of magnitude greater than a typical value obtained via two-color laser mixing with short-length focusing in air.

Chapter 5 introduces a broadband THz source utilizing optical rectification. We have tested various types of crystals for THz generation and measure the resulting THz

energy, beam spot size, pulse duration and spectrum. Here we demonstrate non-phase-matched optical rectification in a planar lithium niobate, which can give a broadband (0.1~15 THz) spectrum with relatively high conversion efficiency (> 10^{-4}).

Chapter 6 ends up with a conclusion and summary of high-field THz generation via laser-based sources. Lastly, Appendix A details THz imaging tools used in this dissertation, including newly developed real-time, data-taking software and a real-time lock-in THz imaging system including a microbolometer camera and a PCIe frame grabber. Appendix B contains transmission spectrum data of our THz bandpass filters used for radiation characterization.

Chapter 2 : High field terahertz generation and beam characterization in two-color laser filamentation at 1 kHz

2.1 Introduction to high field THz generation from two-color laser mixing

Terahertz (THz) generation by two-color laser mixing in air plasma has attracted considerable interest due to its broadband spectrum and high output pulse energy [30–54]. In this scheme, an ultrashort laser pulse's fundamental and second harmonic pulses are co-focused into air to create a plasma filament, simultaneously emitting an intense, single-cycle THz pulse in the forward direction. The resulting pulse can be collimated and refocused to produce an intense THz field at the focus, and such a strong field can be utilized for further studies of THz-field-induced nonlinearities in various materials. The strongest THz field reported so far is 108 MV/cm and achieved by difference frequency mixing of two near-infrared lasers [24]. Here, the strong field arises mostly from high frequency THz components (20–60 THz) with little or no radiation at the conventional THz region (0.1–10 THz) [24]. Recently, such a strong field has been applied to produce THz-driven high harmonics covering the entire THz-to-visible spectrum at 0.1–675 THz [25]. Accelerator-based sources can also produce single-cycle, high-energy (sub-mJ) THz pulses at 0.1–30 THz using ultrashort electron bunches. In particular, the Linac Coherent Light Source (LCLS) has produced a peak field of 44 MV/cm via coherent transition radiation [26]. Another method of producing strong THz radiation is using optical rectification in lithium niobate ($LiNbO_3$) crystals with tilted pulse front excitation. This method can produce extremely high THz energy (current record 175 μJ [27]), but the radiation spectrum is mostly limited to <1.5 THz [27]. This scheme has produced peak THz fields of 1.2 MV/cm at a 1 kHz repetition

rate [4]. Compared to optical rectification in lithium niobate, two-color filamentation provides typically one-order-of magnitude lower conversion efficiency (former: 10^{-3}, latter: 10^{-4}). However, two-color filamentation can produce a one-order-of-magnitude shorter pulse duration, with a one-order-of-magnitude smaller diffraction-limited spot size. This, in principle, can yield a one-order-of-magnitude higher field strength at the focus for the same laser input energy. To date, two-color filamentation has produced several microjoules of THz radiation [48, 58] and reached a radiation bandwidth of 200 THz using 10 fs laser pulses [30]. So far intense fields exceeding several MV/cm have been produced mostly at low repetition rates (10 Hz or less), and their extension to higher repetition rates is desired for applications requiring both strong THz fields and high average power. In this chapter, we demonstrate high-field (>16 MV/cm), moderate-average-power (2.6 mW) THz generation by using an amplified, 1kHz-repetition-rate femtosecond laser system. Here, we characterize our peak THz field strength by measuring its energy, pulse duration, and focused spot size. In addition, we introduce an uncooled microbolometer camera for real-time THz profiling and imaging.

2.2 Experimental setup and characterization method

A 800-nm, 14-mJ, 30-fs, and 1-kHz laser pulse from a cryogenic cooled amplifier is focused via a lens through a BBO crystal (100 μm thickness) to generate the second harmonic (400 nm) pulse which co-propagates with the fundamental (800 nm) pulse and generates air plasma which is called a filament. This filament works as a source of THz radiation and this can emit broadband THz ranges from 0.1~60 THz. To make the first and second harmonic pulses parallelly polarized and to minimize the walk-off (~9 fs) between them, a thin (~45 μm) dual-wavelength half-wave plate is placed right after the BBO crystal. This maximizes the output THz radiation energy. To block the optical light and maximize THz (linearly polarized) transmission, a Si window is placed in the bema path at the Brewster angle (~74 degrees).

The output THz energy is measured by a pyroelectric (SPI-A-62-THZ, Spectrum Detector Inc.) and a thermopile detector (THz12–3S-VP, Gentec). The maximum energy measured with the pyroelectric detector is 1.44 μJ per pulse with an input energy of 14 mJ. Here the conversion efficiency is 10^{-4}, consistent with many previous measurements [48, 58]. A similar value is obtained with the thermopile detector. Both detectors are expected to provide a flat spectral response over a broad range of THz spectrum (3–30 THz), and the pyroelectric detector is calibrated at 800 nm whereas the thermopile detector is pre-calibrated at 10.6 to 400 μm and includes typical wavelength correction data from 10.6 to 440 μm.

For THz beam profiling and imaging, a vanadium oxide uncooled microbolometer array (Tau 2, FLIR Inc.) is used. Although microbolometer cameras are designed for thermal imaging at 7–14 μm, they have been effectively used for THz

beam profiling and imaging at longer wavelengths (14–300 μm), including THz detection with LiNbO3 [4] and air-plasma [90-94] based THz sources. The microbolometer camera used here provides images with 336x256 pixels (17μm pitch) and can stream 8-bit images at a rate of 30 frames/s or capture and store 14 bit images up to 60 frames. Although the noise equivalent differential temperature (NEDT) is specified as <50 mK at 7.5–13.5 μm, its sensitivity at 0.1–10 THz is unknown. Unlike a NEC microbolometer camera which is designed for THz detection [4] and THz beam profiling [90], our microbolometer has not been tested previously for THz application.

In order to measure the pulse width of emitted THz radiation, a waveform is obtained via ABCD with an additional optical probe pulse (see Fig. 1). Figure 2.1 shows a sample THz waveform with a pulse width of 120 fs, with a corresponding radiation bandwidth exceeding >20 THz as shown in Fig. 2.1. Here, the pulse duration could be overestimated due to our chirped probe pulse and imperfect ABCD implementation. The actual pulse width can be even shorter than 120 fs, possibly 1.5 times shorter based on the comparison of the radiation bandwidths measured by ABCD (20 THz) and Fourier transform infrared (FTIR) interferometry (>50 THz) taken under a similar condition

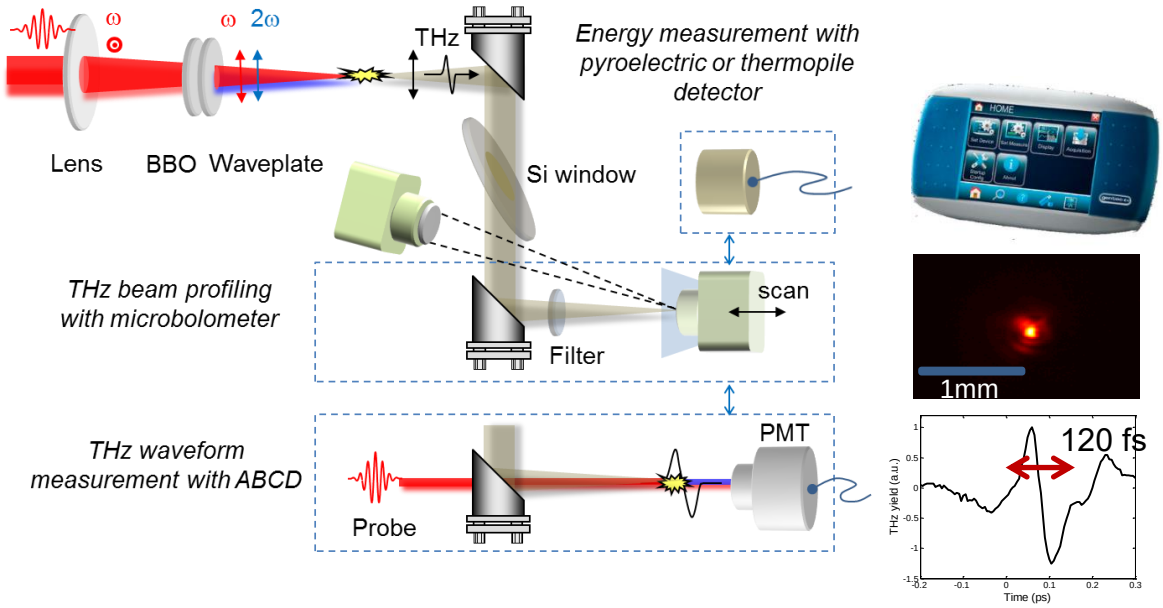

Figure 2.1 Schematic of strong THz field generation via two-color laser filamentation in air and characterization. For maximal THz generation, a combination of a thin dichroic λ/2 waveplate and a large-size (4 in.), Brewster-angled Si window is used. For characterization, THz waveforms, energies, beam profiles are measured to determine the peak THz field strength (> 8 MV/cm). For THz beam profiling, an uncooled microbolometer focal plane array is used with various filters in two different modes. For indirect beam profiling, a Ge lens is attached to the camera for imaging

2.3 Experimental results with long focusing and tight refocusing

Figure 2.2. shows two types of schemes used to refocus THz radiation emitted from the plasma. In the first method, two off-axis parabolic mirrors (6" and 2" focal lengths) are used to collimate and refocus the THz beam, respectively. The first parabolic mirror has a hole in the center to by-pass the optical beam. Since the THz beam has a conical shape, it is not affected by the hole. In our second scheme, the THz beam is refocused by a Ge lens of 2" focal length. Various filters (high-density polyethylene or Teflon) are placed in front of the Ge lens to attenuate the optical beam. The Ge lens gives an energy loss of ~70% due to THz absorption and reflection, but the design is much simpler and alignment is easier compared to the first scheme. For high-field THz generation, however, the first scheme is adopted to avoid THz absorption or loss occurring in transmission-type THz optics.

To determine the field strength of the refocused THz radiation, we measure the THz energy, beam spot size, and pulse duration at the refocus. From these three parameters, we can calculate the maximum field strength at the refocus as [91]

$$\varepsilon = \varepsilon_0 c \int dA \int_{-\infty}^{\infty} E^2(t, A) dt. \quad (2\text{-}1)$$

Here, ε is the measured THz energy, $\varepsilon_0 = 8.854 \times 10^{-12}\ F/m$ is the permittivity of vacuum, c is the speed of light in vacuum, A is the area of detection plane, and $E(t, A) \approx E_{max} \hat{E}_t(t) \hat{E}_s(A)$ is the THz waveform with the normalized temporal waveform $\hat{E}_t(t)$ and spatial profile $\hat{E}_s{}^2(A)$. This can determine the maximum field strength, E_{max}, on the focal plane.

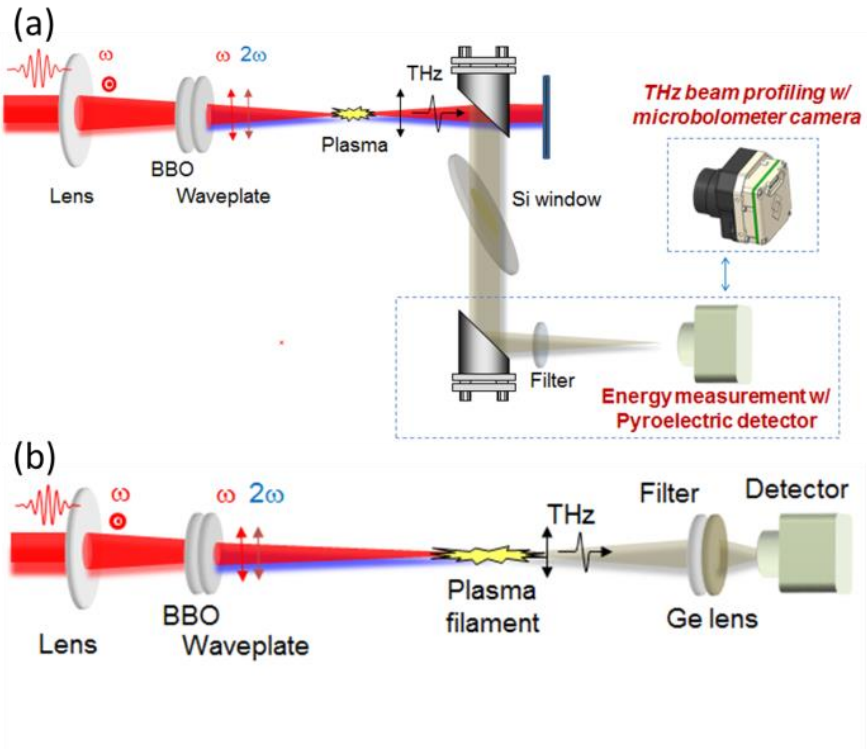

Figure 2.2 (a) Experimental setup of high-field THz generation and refocusing by using two off-axis parabolic mirrors (top) and (b) a Ge lens (bottom). The maximum THz field strength at the refocus is determined by measuring the THz energy, spot size, and waveform

2.3.1 THz energy measurement

In our previous report, a maximum THz energy of 1.4 μJ was produced at 1 kHz via short-focal-length (f = 200 mm) focusing [91]. However, long filamentation can deliver more THz energy by mitigating plasma-induced defocusing and thus providing efficient coupling of laser energy into THz radiation [54]. In practice, the plasma length can be elongated by focusing the incoming laser with a long-focal-length lens. Here we perform a focal-length scan from f = 200 mm to f = 1000 mm to find the optimal focal length for THz generation at various laser energies (0.5~10 mJ).

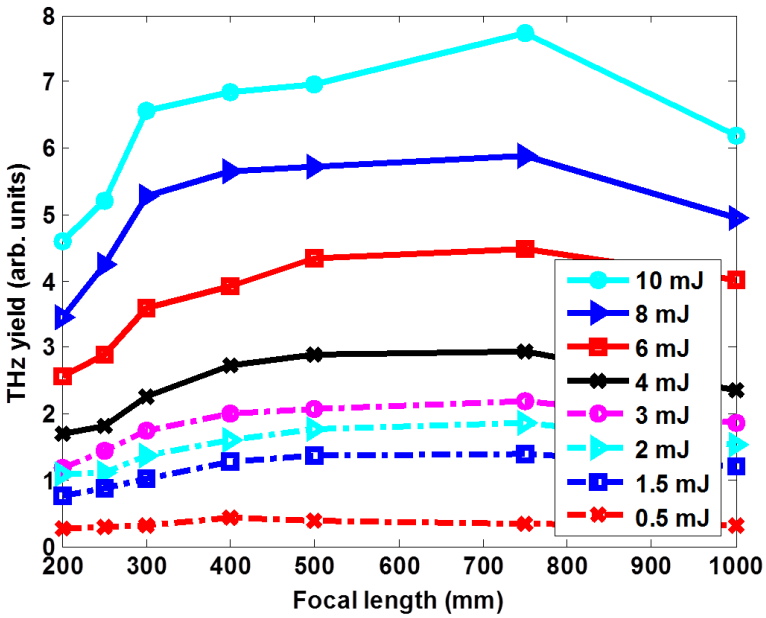

Figure 2.3 THz output energy as a function of lens focal length and laser input energy. With a focal length of 750 mm, the THz yield is almost doubled compared to short-focal-length focusing (f = 200 mm)

Figure 2.3 shows that the output THz energy strongly depends on the focal length f. It shows that f = 400 mm gives the best performance at low energy (0.55 mJ). The peak point, however, shifts toward f = 750 mm as the input laser energy increases. This is due to plasma-induced defocusing. When the laser energy increases, the plasma density at the focus increases but soon saturates because the plasma created by the early part of the laser pulse becomes dense enough to refract the rest part of the pulse away from the focus. This defocusing effect can be mitigated by elongating the plasma length with weak focusing. This increases the plasma (or source) volume, while dropping the plasma density below the saturation limit, and can yield more THz energy. Our

measurement is consistent with previous reports [54, 58, 62]. By generating a long (~6 cm) plasma with *f*=750 mm focusing, the THz output energy almost doubles compared to the short focusing case (*f* = 200 mm). The output energy, however, drops with even longer focusing (*f* = 1000 mm). That is because the plasma density drops significantly with extremely weak focusing, and this yields less THz energy. The maximum THz energy obtained here is 2.6 μJ at 10 mJ of laser energy with *f* = 750 mm focusing. This gives a conversion efficiency of 2.6×10^{-4}, almost 2.5 times higher than that obtained with *f* = 200 mm focusing in our previous report [91].

We note that the pyroelectric sensor is calibrated at wavelengths of 532 nm, 650 nm, and 800 nm, which all provides a similar responsivity of 2.5×10^4 V/W at a chopping frequency of 13 Hz. Our pyroelectric detector provides a flat response over a wide range of wavelengths although the spectral response deviates from its flat line at low THz frequencies (<3 THz) mostly due to reduced THz absorption by organic black coating. This could provide underestimated THz output energy at low frequencies (<3 THz). For the experiment performed here at 1-kHz, the pyroelectric detector provides a calibration value of 0.04 μJ/V per pulse. Here the measurement represents THz energy immediately after the plasma, not after attenuated by the Si and other filters used for THz detection.

2.3.2 THz beam spot size measurement

The refocused THz beam size is measured by an uncooled microbolometer camera (Tau 2, FLIR Inc.). This is a 2-D focal plane array which is designed to detect

radiation at wavelengths of 7~14 μm. This camera, however, can be used to detect THz radiation at lower frequency radiations (<20 THz) as well [91, 94]. More details about the camera are provided in Appendix A.

In our previous study, there was a concern that long filamentation could generate more THz energy but unfavorably increase the spot size of the refocused THz radiation [54]. This could result in no gain in the THz field strength. This concern, however, had not been examined or verified. Here we directly measure the refocused THz spot size. In particular, we use a short (2") focal length optic (off-axis parabolic mirror or Ge lens) to minimize the THz spot size.

Figure 2.4(a) shows the refocused THz beam spot size obtained with different laser input energy and different focal length of lens. It shows the THz spot size can be maintained within 30~50 μm (average of 43 μm) in full width at half maximum (FWHM) in most cases. The corresponding central lineouts are shown in Fig. 3(b) at laser input energy of 4 mJ. Contrary to the previous concern, Figure 3 shows that the refocused THz spot size is insensitive to the laser energy or focal length. This implies that more THz energy can be obtained by increasing the plasma length, and this does not significantly affect the refocused THz spot size. Therefore the refocused THz field strength can be enhanced with increasing filament length until the plasma density drops significantly with extremely weak focusing.

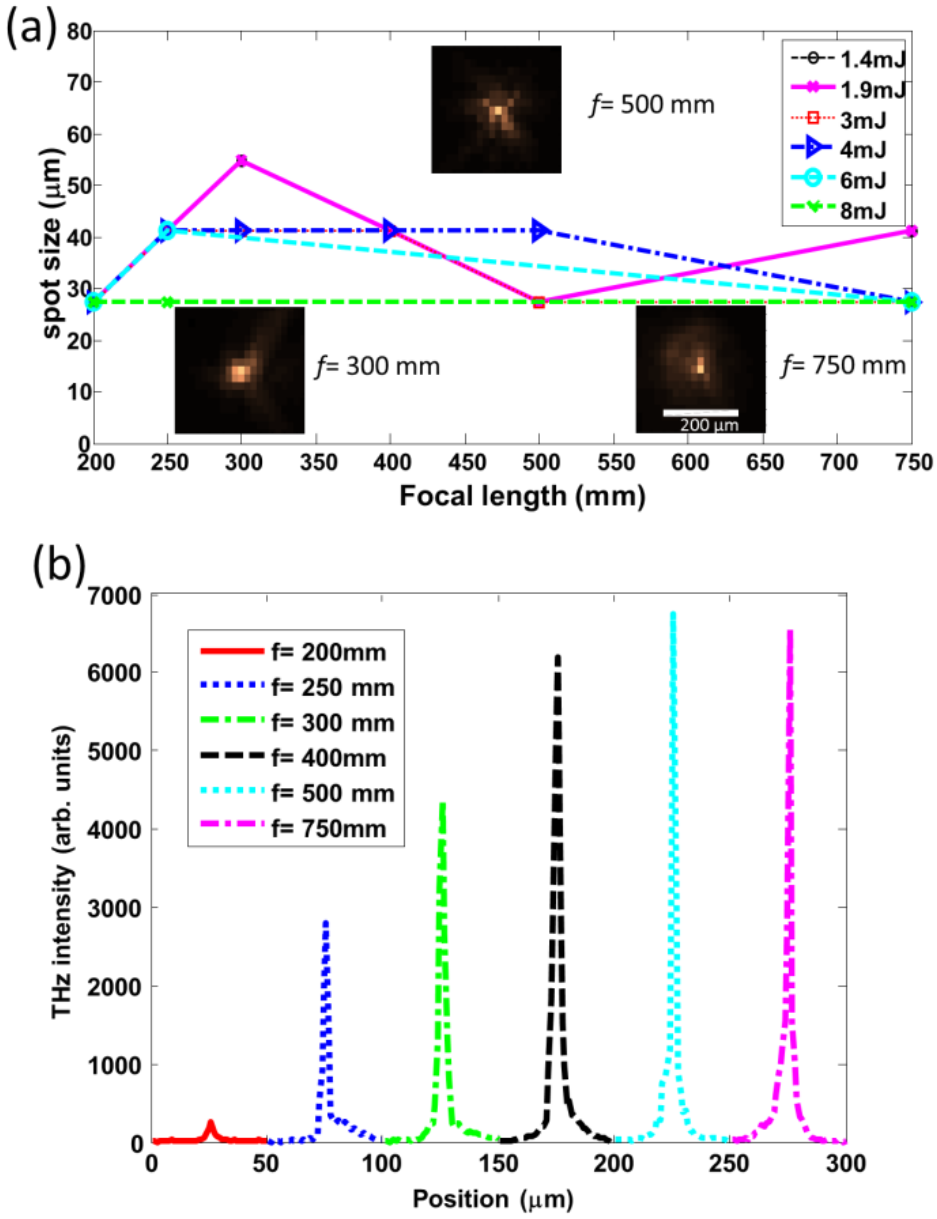

Figure 2.4 (a) Refocused THz beam spot size (FWHM) as a function of lens focal length and laser input energy. The insets are refocused THz profiles obtained with focal length f = 300, 500, and 750 mm. (b) Central lineouts at the refocus, obtained with f = 200~750 mm at 4 mJ of laser energy

2.3.3 THz pulse duration and spectrum measurement

THz waveforms are measured with an Electro-Optic (EO) sampling method using a 100-μm-thickness GaP crystal. Figure 3.5 shows a normalized THz waveform and its corresponding spectrum obtained with f = 750 mm. The spectrum extends up to 15 THz, and this gives an effective pulse duration of ~200 fs, assuming no temporal chirp. This pulse duration is ~2 times longer than the measurement made with an Air Biased Coherent Detection (ABCD) technique in our previous work [91]. This discrepancy arises from strong THz absorption and dispersion in GaP at >10 THz, and this limits our pulse duration measurement in EO sampling.

As a complementary method, various THz bandpass filters (central frequency at 1, 3, 6, 10, 15, 20, 24, and 30 THz, Thorlabs) are used along with pyroelectric detection to confirm the presence of much broader (>30 THz) spectrum. This measurement is shown as a red line with crosses in Fig. 3.5(b). It shows strong high-frequency components (15~30 THz) that could not be detected by EO sampling. As the measurement is limited by the highest bandpass filter (30 THz) used here, the spectrum is expected to extend beyond 30 THz. From this and our previous measurements with ABCD, we can conclude that the actual THz pulse duration can be much shorter than 200 fs.

We note that the THz bandpass filters are gold mesh frequency selective films and provide narrow transmission bandwidths. Our Fourier transform infrared (FTIR) spectroscopy measurements show that the low frequency bandpass filters (1, 3, 6, and 10 THz), however, have undesirable strong transmission (>2 %) at a broad range of high frequencies (>15 THz). Those contributions are removed by incorporating

separate measurements made with high frequency bandpass filters (15, 20, 24 and 30 THz). In addition, the long-pass (7.3 μm cutoff) filter used here limits our detection up to 40 THz.

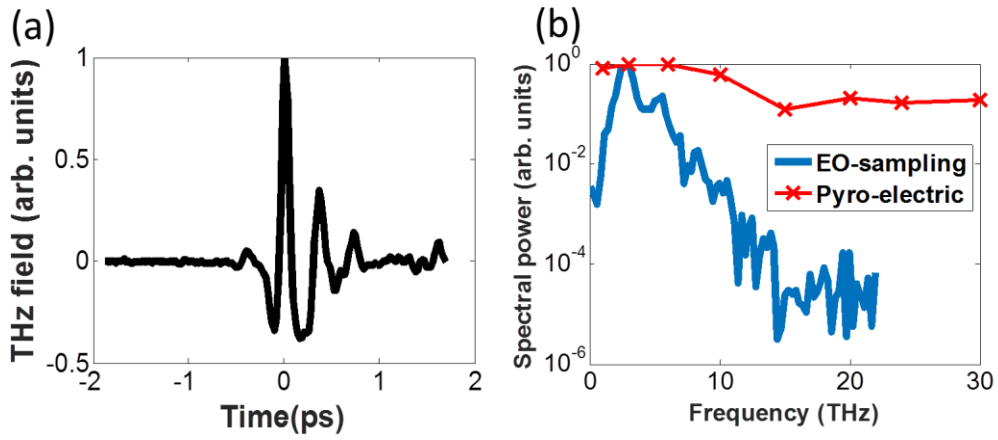

Figure 2.5 (a) THz waveform obtained via EO sampling in a 0.1-mm-thickness GaP crystal. (b) THz spectrum measured by EO-sampling (solid blue line) and pyro-electric detection (red line with crosses)

2.3.4 Study on the THz beam divergence angle

As a supplementary study, the dependence of THz divergence angle on focusing geometry and spectral component is discussed in this section. It is important to know the divergence angle of the THz radiation emitted from the plasma filament in order to produce the smallest, diffraction-limited, THz spot size on the target. This is also necessary to determine the proper size of a refocusing module and its optimal distance from the plasma source.

In general, the divergence angle can be measured by conducting far-field THz beam profiling by 2-D raster scanning with pyroelectric [52] or Golay-cell [82] detectors. These methods take a long time and are vulnerable to shot-to-shot energy

fluctuations during a scan. Instead, a 2-D focal plane array such as a microbolometer camera can be used for snapshot imaging [90-91].

In this section, we perform near and far-field THz imaging and study how different focusing geometry affects the divergence angle of THz radiation. In particular, we measure near and far-field beam profiles with various THz bandpass filters to characterize frequency-dependent THz radiation profiles.

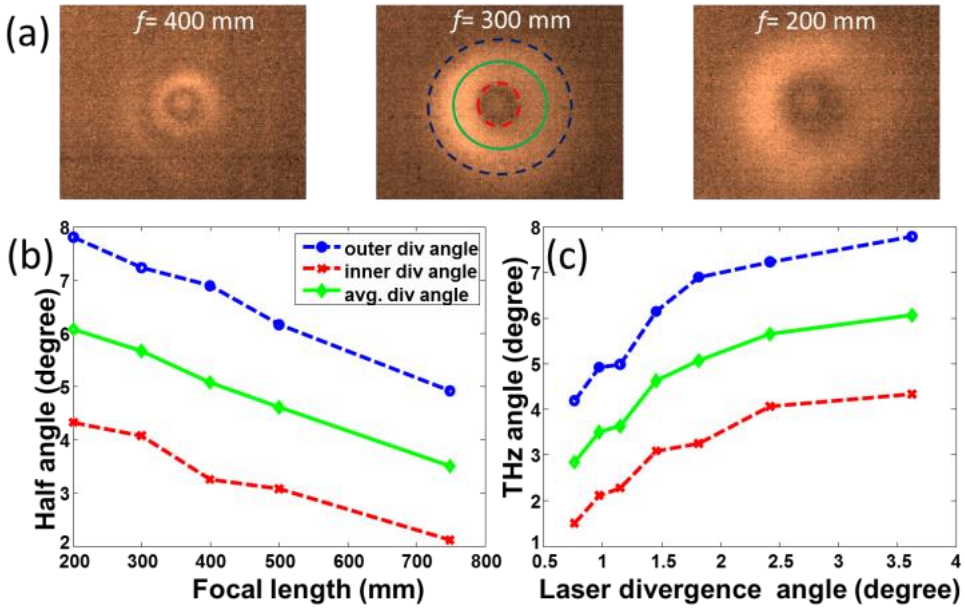

Figure 2.6 (a) THz beam profiles in the far-field resulted from two-color laser focusing with different focal lengths (f = 200, 300, and 400 mm). The THz divergence angles (inner/outer edges and their average) are plotted as a function of the lens focal length in (b) or equivalently of the laser divergence angle in (c).

Figure 2.6 shows that the divergence angle of THz radiation is strongly dependent of laser focusing geometry (f-number). Here, we measure far-field THz beam profiles with the microbolometer camera, when two-color laser pulses are focused by a lens with different focal length (200~1000 mm, see Fig. 2.1).

Figure 2.6(a) shows THz beam profiles obtained with f = 200, 300, and 400 mm. From the focal and far-field THz beam profiles, obtained with different positions of the Ge imaging lens (see Fig. 2.1), we can calculate the THz divergence angle for each focal length. The measured divergence angles are plotted as a function of lens focal length in Fig. 2.6(b), including the divergence angles of both inner (red dashed line) and outer (blue dashed line with circles) edges of conical THz radiation. Figure 2.6(b) shows that the averaged THz divergence angle (green line) almost linearly decreases with increasing focal length of the lens. The divergence angles are replotted as a function of the incident divergence angle of laser (unfocused beam size of ~15 mm) in Fig. 2.6(c). This shows that the THz divergence angle of the inner edge is always greater than that of the incident laser. This indicates that the THz beam is completely separated from the optical beam after its generation.

Also, the divergence angle of THz radiation depends on spectral component as well. To verify this experimentally, THz bandpass filters are used along with the microbolometer to characterize frequency-dependent THz radiation profiles. Figure 2.7 shows THz profiles at 15 THz, 20 THz, and 30 THz, imaged along its propagation direction when focused with f = 750 mm. Here low frequency filters (1, 3, 6, 10 THz) are not used because of their unfavorable transmission at high frequencies (>15 THz), which cannot be simply removed by image reconstruction. In addition, an off-axis parabolic mirror of 4” focal length (instead of 2”) is used to make space for the THz bandpass filter so that it can be placed in between the parabolic mirror and microbolometer. This change results in an increased focal spot size, almost twice bigger than that obtained with the parabolic mirror of 2” focal length.

Figure 2.7 also shows that the THz divergence angle is frequency-dependent. It is measured to be 3.4°, 3.3°, and 3.2° with 15 THz, 20 THz, and 30 THz bandpass filters, respectively. Although the amount of change is small, it is clear that the higher THz frequency component has the smaller divergence angle, consistent with previous reports [52, 82].

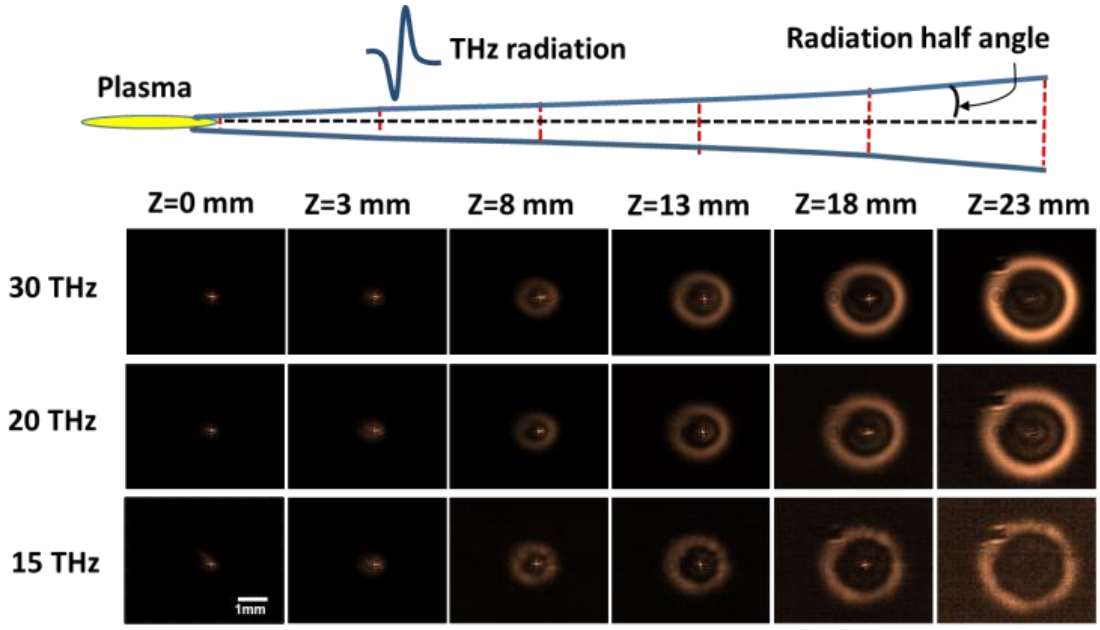

Figure 2.7 THz beam profiles along the propagation direction (from the focal plane z = 0 to z = 23 mm), taken by the microbolometer camera with a narrow-bandpass filter (15, 20 or 30 THz) placed in the beam path

2.4 Conclusion

In this chapter, we have investigated strong THz field generation from two-color laser mixing in air. In particular, we have studied the dependence of output THz energy and refocused spot size on input laser energy and focusing geometry. We find

that long filamentation provides almost twice more THz energy compared to short filamentation under the same laser condition. Contrary to our previous concern [54], near diffraction-limited THz spot size can be achieved at the refocus even with long-length filamentation.

In practice, we have obtained the maximum THz energy of 2.6 μJ with long filamentation, refocused THz spot size down to 43 μm via tight refocusing, and effective pulse duration of 200 fs measured by EO sampling in GaP. These measurements provide the maximum THz field strength of ~16 MV/cm at a 1-kHz repetition rate. As the pulse duration is overestimated due to THz absorption in GaP, the actual field strength could be even higher. With an assumption that the actual pulse duration be comparable to our previous measurement (~100 fs) [91], then the maximum field strength can be as high as 23 MV/cm.

We have also characterized conical THz radiation profiles in both short and long-length filamentation, and find that their divergence angles strongly depends on the focusing geometry. In addition, frequency-dependent THz radiation beam profiles are characterized in long-length filamentation.

Chapter 3 : Terahertz generation from 2D-plasma sheet by cylindrically focused two-color laser filamentation

3.1 Introduction to Terahertz generation from cylindrical focusing

For high-energy THz generation, high-power lasers can be employed to produce plasma filaments. However, it is shown that output THz energy strongly saturates with increasing laser power [54, 58]. This saturation occurs mainly due to ionization-induced defocusing and laser intensity clamping in filamentation [54], resulting in ineffective coupling of laser energy into the plasma. This saturation effect can be reduced by re-distributing the incoming laser energy over a longer plasma length with weaker focusing [54]. An alternative method is to increase the plasma volume in the transverse direction by creating a 2-dimensional (2D) plasma sheet [92].

In this section, we demonstrate scalable terahertz (THz) generation by focusing terawatt, two-color laser pulses in air with a cylindrical lens. This focusing geometry creates a 2-dimensional air plasma sheet, which yields two diverging THz lobe profiles in the far field. This setup can avoid plasma-induced laser defocusing and subsequent THz saturation, previously observed with spherical lens focusing of high-power laser pulses. By expanding the plasma source into a 2-dimensional sheet, cylindrical focusing can lead to scalable THz generation. This scheme provides an energy conversion efficiency of 7×10^{-4}, ~7 times better than spherical lens focusing. The diverging THz lobes are refocused with a combination of cylindrical and parabolic mirrors to produce strong THz fields (>21 MV/cm) at the focal point.

3.2 Experimental setup

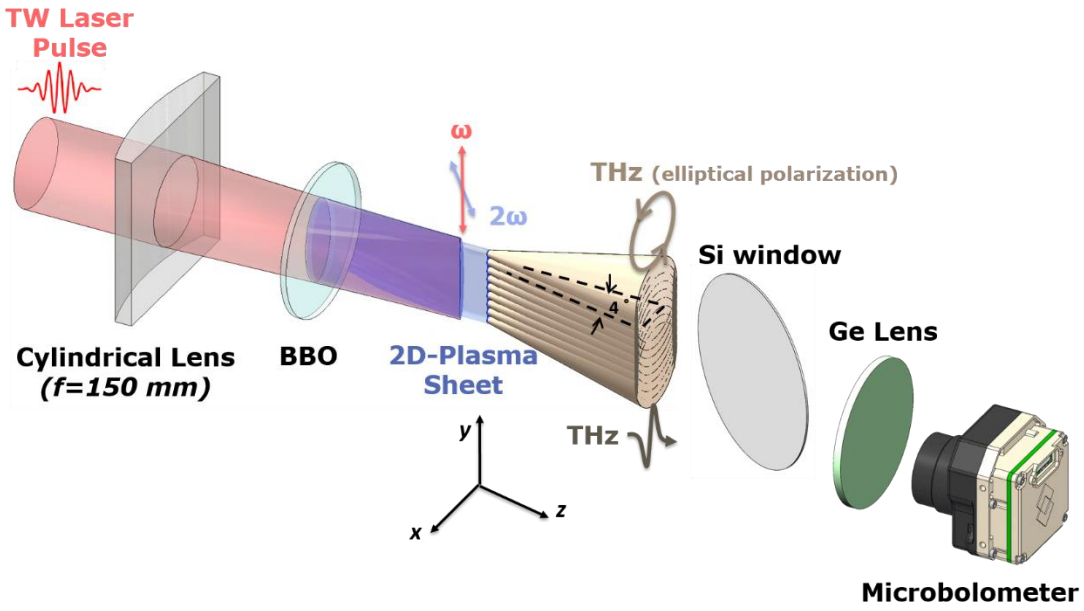

Figure 3.1 Experimental scheme for scalable THz generation from a two-dimensional (2D) plasma sheet created via cylindrical lens focusing. The 2D plasma sheet emits an array of vertically overlapping conical THz beams, resulting in two upright THz lobes in the far field due to interference.

Figure 3.1 shows our schematic of two-color laser pulse focusing in air with a cylindrical lens. A terawatt (TW) laser pulse (wavelength λ = 800 nm, duration τ = 50 fs, energy $E_L \geq$ 50 mJ, repetition rate 10 Hz) is focused by a cylindrical lens of 150 mm focal length. A 100-μm thick beta barium borate (BBO) crystal is placed right after the cylindrical lens to produce a second harmonic (2ω) pulse, which co-propagates with the fundamental frequency pulse (ω). These two pulses are continuously focused in air and produce a 2D plasma sheet at the focus, also emitting a broadband, single-cycle

THz pulse in the forward direction. Here the polarization of the emitted THz radiation is generally elliptical as the two-color pulses are not collinearly polarized [51]. To measure THz radiation profiles, a silicon (Si) wafer is set after the plasma sheet as a window to transmit THz beams only. The Si filter is placed ~115 mm away from the plasma sheet to avoid potential damage and minimize charge carrier generation on the Si filter by the optical beam. Here the Si filter provides THz throughput of ~50%. After the Si filter, a 2”-diameter germanium (Ge) lens of focal length f = 76 mm is placed to image the output THz beam profile onto an uncooled microbolometer camera (FLIR tau2, 17 μm pixel size, 336 × 256 resolution) [91]. Although microbolometer cameras are designed for thermal imaging at 7~14 μm, they can be still used for detecting radiation at much longer wavelengths [91].

3.3 Results and discussion

3.3.1 THz divergence experiments

Figure 3.2 (a) shows a typical THz beam profile imaged near the exit plane of the plasma sheet (z=0). To observe how the beam profile changes along its propagation direction z, the microbolometer position is scanned along z. Figure 3.2(b) shows a sequence of THz beam profiles at z = 0 mm, z = 2.4 mm, z = 3.5 mm, z = 5.0 mm, and z = 5.7 mm after the plasma exit plane. It shows a pattern of two diverging vertical lobes, which can be understood by Huygens's principle. The 2D plasma sheet is considered to have an array of line sources (filaments), which individually emit conical THz beams in the far field (see Fig. 3.1). Constructive interference occurs along the vertical lines of the superimposed cones, and destructive interference occurs elsewhere. This results in two upright THz lobes on the edges. Here the THz lobes diverge with the same angle as in conical radiation (see Fig. 3.1). In our case, the divergence half-angle is measured to be 4°, consistent with previous measurements using spherical focusing [52, 82, 90]. Here the divergence angle is dominantly determined by the Cherenkov-type phase matching for relatively short filament lengths, typically less than ~10 mm as in this experiment.

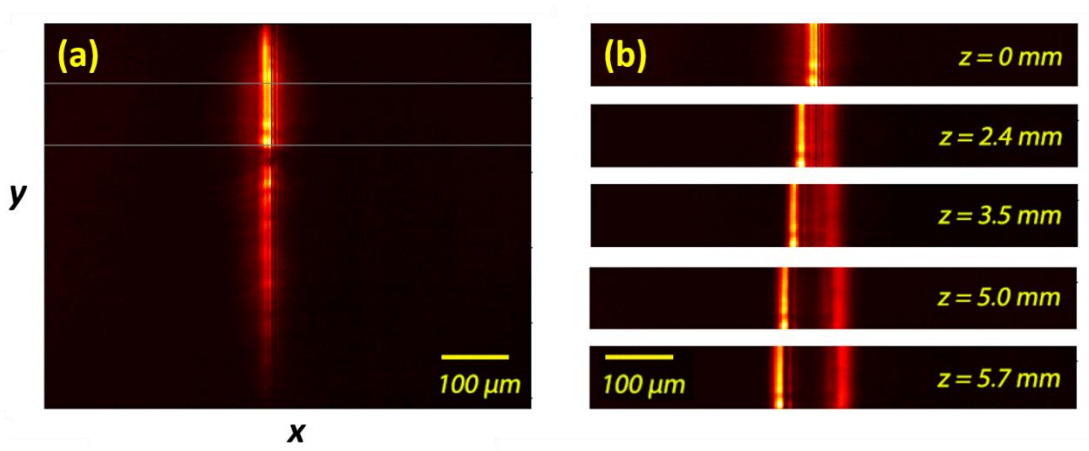

Figure 3.2 THz beam profiles obtained via relay imaging with laser input energy of 30 mJ. The left image, (a), shows a THz beam profile imaged near the plasma sheet (z=0). The right, (b), is the THz beam profiles imaged at z = 0, z = 2.4, z = 3.5, z = 5.0 and z = 5.7 mm along its propagation. All images in (b) are partially cropped for visual guidance.

3.3.2 THz beam characterization by refocusing

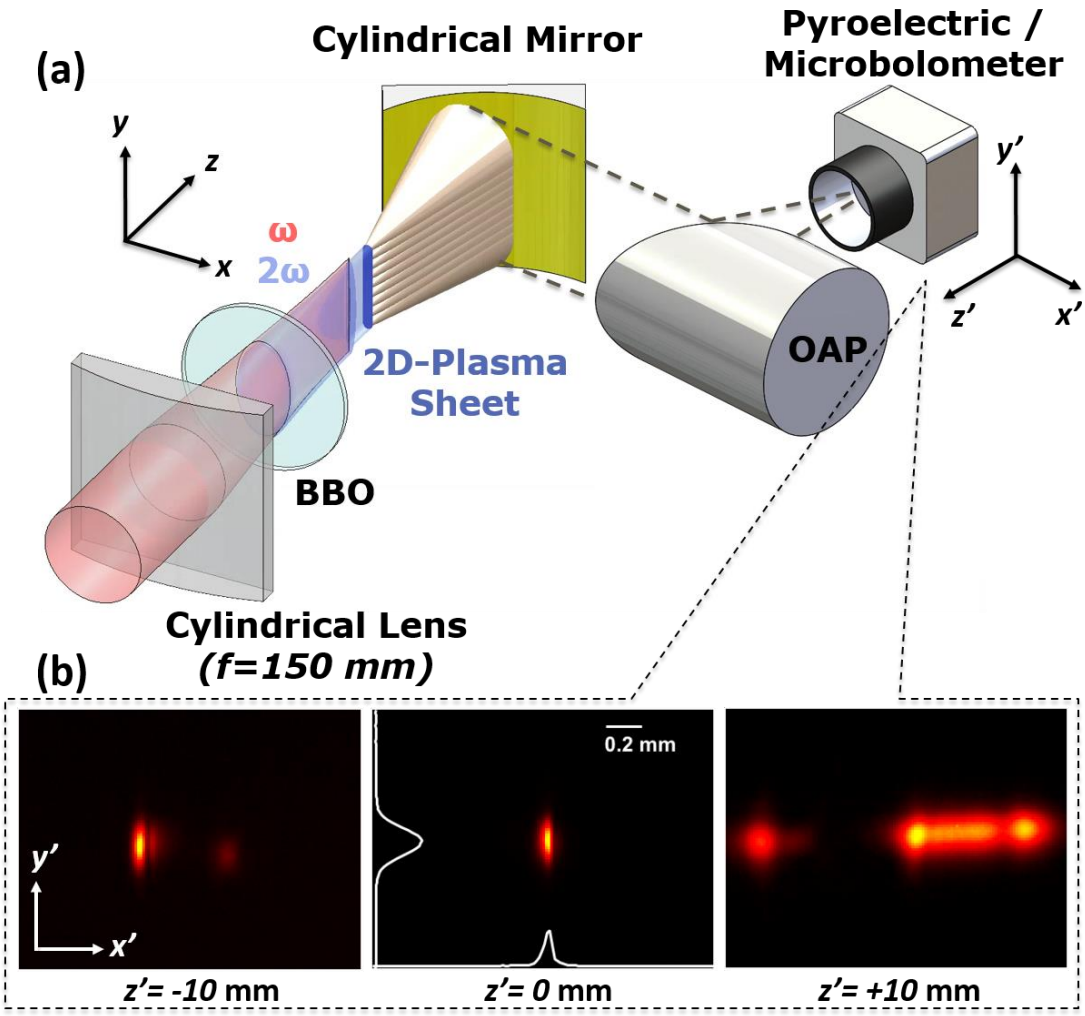

Figure 3.3 (a) THz re-focusing scheme with a combination of a gold-coated concave cylindrical mirror with *f*=175 mm and an off-axis parabolic (OAP) mirror with *f*=152 mm. (b) Re-focused THz beam profiles on the microbolometer when scanned along the beam direction.

For practical applications, such diverging radiation must be refocused to create intense THz fields at a target point. In our case, a combination of a concave cylindrical mirror with f = 175 mm and an off-axis parabolic (OAP) mirror with f = 152 mm is used to refocus THz radiation as shown in Fig. 3.3(a). Here the cylindrical mirror is coated with 200-nm thick gold for efficient THz reflection, and it is tilted ~28° off from

the beam direction to collimate and redirect the diverging THz radiation to the OAP for final refocusing. In addition to a Si window, a 0.4-mm thick high density polyethylene (HDPE) filter placed in the beam path (both not shown in Fig. 3.3(a)) to transmit THz radiation only. Figure 3.3(b) shows refocused THz beam profiles on the microbolometer when scanned along the beam propagation direction (z). It shows two upright THz lobes approaching each other as they propagate (at z′ = −10 mm), then merging (at z′ = 0 mm), and finally moving away from each other (at z′ = 10 mm). At the best focus (z′ = 0 mm), the THz focal spot size is estimated to be $r_{FWHM} = \sqrt{r_x\, r_y}$ = 120 μm, where r_x = 70 μm and r_y = 205 μm in full width at half maximum (FWHM). Here r_x is similar to the typical spot size obtained with spherical focusing [91], but r_y is much larger r_x due to unwanted astigmatism in our refocusing setup. This could be minimized, in principle, by choosing the proper focal length and tilt angle of the cylindrical lens. Also one part of the refocused THz lobes is much larger and brighter than the other one due to aberration caused by the titled cylindrical mirror and possible THz beam clipping in our setup.

After determining the optimal refocusing position, the microbolometer is then replaced with a 9-mm-diameter pyroelectric sensor (QS9-THZ-BL, Gentec-EO Inc) to measure the refocused THz energy. Figure 3.4 shows the output energy as a function of input laser energy. Here, in addition to the Si filter used to block optical beams, 3-mm thick Ge and 1.5-mm thick HDPE filters are used to detect THz radiation at high (0.4~150 THz, solid lines) and low (0.1~10 THz, dashed lines) frequencies, respectively. The red curves represent the output THz energy generated from a plasma sheet by cylindrical lens focusing. In comparison, the blue curves represent a spherical

focusing case with the same focal length f = 150 mm. For low input laser energies (E_L ≤ 15 mJ), spherical focusing yields more THz output compared to cylindrical focusing. This is because the laser intensity on the plasma sheet is not sufficiently high enough to drive strong plasma currents. This is also evident from plasma fluorescence emitted from the plasma sheet (see Fig. 3.5). When the input laser energy is less than 15 mJ, the fluorescence from the plasma sheet and supercontinuum in the forward direction are barely observable. However, when the laser energy exceeds 15 mJ, cylindrical focusing overtakes spherical focusing and yields much more THz output. In the case of spherical focusing, the output energy hardly increases at E_L ≥ 15 mJ, and it finally saturates at ~3.7 μJ. By contrast, the THz energy obtained with cylindrical focusing gradually increases at E_L = 10~15 mJ and then rapidly enhances beyond 20 mJ, ultimately reaching ~31 μJ at E_L = 45 mJ. This value is ~8 times higher than that obtained with spherical focusing (3.7 μJ). Also, the conversion efficiency from laser to THz energy is estimated to be 7×10^{-4} with cylindrical focusing, which is 7 times higher than the typical value (~10^{-4}) in two color laser mixing in air [58, 91]. We note that a much higher value (~10^{-3}) was achieved by using a longer wavelength driver [5] but it typically requires an additional optical parametric amplifier (OPA) system. Here the maximum THz field strength is expected to be ~21 MV/cm at the focal spot, which is obtained from the measured spot size (~120 μm) and estimated pulse duration (~100 fs) [54]. Even though the spot size is not fully optimized (see Fig. 3.3(b)), 21 MV/cm is the highest field strength that has been achieved with two-color laser mixing in air [30-54, 91, 93].

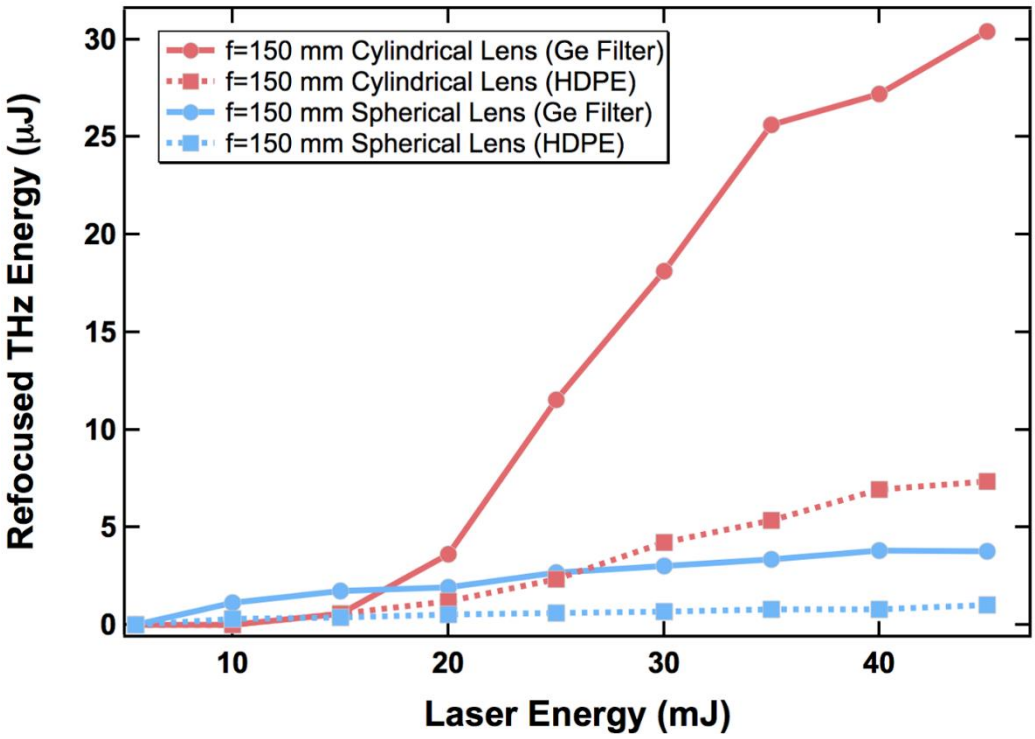

Figure 3.4 Refocused THz beam energy as a function of input laser energy, obtained via cylindrical (red lines) and spherical (blue lines) focusing with the same focal length *f*=150 mm. The THz energy is measured by a pyroelectric detector with a Ge (solid lines) or HDPE (dashed lines) filter placed in front.

3.3.3 Plasma fluorescence imaging

A charge coupled device (CCD) camera with an imaging lens is also set to monitor fluorescence emitted from the 2D plasma sheet. Figure 3.5(a) shows a series of plasma sheet images taken from the side direction. Figure 3.5(b) shows how the fluorescence

brightness varies as a function of laser energy. It shows that the 2D plasma sheet emits more fluorescence light with increasing laser energy, unlike our previous study with spherical focusing where strong saturation was observed even at laser energy of <20 mJ with pulse duration of ~50 fs [54]. Although the fluorescence signal is not linearly proportional to the electron density or laser intensity, the trend shown in Fig. 3.5(b) supports scalable laser-to-THz conversion in cylindrical focusing. This observation is in a good agreement with the energy measurement in Fig. 3.4.

It is interesting to note that the fluorescence images in Fig. 3.5(b) show all continuous intensity distributions along the 2D sheets, not showing any filamentary structure. In general, multiple filamentation can occur when the laser power exceeds 20~30 times the critical power $P_c = \alpha\lambda^2/(4\pi n_0 n_2)$ for self-focusing [68]. Here λ is the wavelength in vacuum, α is a constant that depends on the initial beam intensity distribution ($\alpha \approx 1.9$ is for a Gaussian beam), and $n_0 \approx 1$ and $n_2 \approx 7.8 \times 10^{-24}$ m^2/W are the linear and nonlinear refractive indices, respectively, at λ = 800 nm in atmospheric air [66], and this gives $P_c \approx 12$ GW. For an elliptical beam with a large eccentricity e, the critical power P_c increases further by a factor of $(0.4e/2 + 0.6)$ [67, 68]. With $e \approx$ 100 in our case, the laser power (P_L) is slightly less than the enhanced critical power ($P_L/P_c \approx 0.8$). This indicates that multiple filamentation is not expected in our experimental condition. Moreover, our tight focusing condition (f=150 mm) further inhibits multiple filamentation.

Although multiple filamentation is not observed, its concept can be utilized to explain the maximum THz energy (31 μJ) obtained with cylindrical lens focusing. Assuming each filament has a diameter of ~100 μm [68, 69], the plasma sheet of ~10

mm height and ~3 mm width (see the inset to Fig. 3.5(b)) can be viewed to have an array of ~100 closely packed filaments, with a total length of ~300 mm if all connected in the longitudinal direction. Compared to our previous study [54], where ~7 μJ THz energy was obtained from a ~70 mm long filament created by spherical lens focusing (f = 1 m), the plasma sheet produces a 4.3× longer effective filament length, yielding 4.4× more THz output energy (≈31 μJ). This consistency shows that the source (plasma) volume can be equivalently increased by 2D sheet formation. Similarly, the upper limit of THz output energy can be also estimated. As each filamentary volume can emit THz energy up to 3.7 μJ (see Fig. 3.4), the entire plasma sheet can yield 100 times higher THz energy (~300 μJ) with the current setup but with more input laser energy. Further enhancement can be achieved by simply expanding the input laser beam size with increasing laser energy. We note that this scheme is much simpler that previous approaches where multiple laser beams are used to create an array of multiple filaments

3.3.4 Single Shot THz spectrometer

We report a novel, single-shot method to measure the spectrum of THz radiation emitted from two-color laser focusing in air. Previously, the spectrum was measured by using Electro-Optic Sampling (EOS), Air Biased Coherent Detection (ABCD), or Fourier Transform Infrared spectroscopy (FTIR) [58]. However, these methods typically need multi-shot pump-probe scanning, and thus it takes a long time for data acquisition. This is also vulnerable to shot-to-shot laser energy fluctuations.

For single-shot spectral characterization, cylindrical focusing is adopted to generate a two-dimensional (2-D) plasma sheet, which generates coherent two diverging THz

lobes. Those THz lobes are collected and refocused by a cylindrical mirror onto an uncooled microbolometer 2-D array where the THz beams with different incident angles interfere and generate fringe patterns (see Fig. 3.6(b)). The interference pattern can be analyzed to extract the spectral power of the emitted THz beam (see Fig. 3.6(c)).

3.4 Conclusion

In this chapter, we have demonstrated scalable THz generation via cylindrical focusing of two-color laser pulses in air. This scheme is well suited for high-power (multi-TW) lasers, capable of yielding gigawatt (peak power), high energy (sub-mJ) THz radiation with a relatively compact setup. It is also shown that the diverging THz radiation produced with cylindrical focusing can be properly refocused to create strong THz fields (tens of MV/cm) for further studies on extreme nonlinear THz optics and spectroscopy.

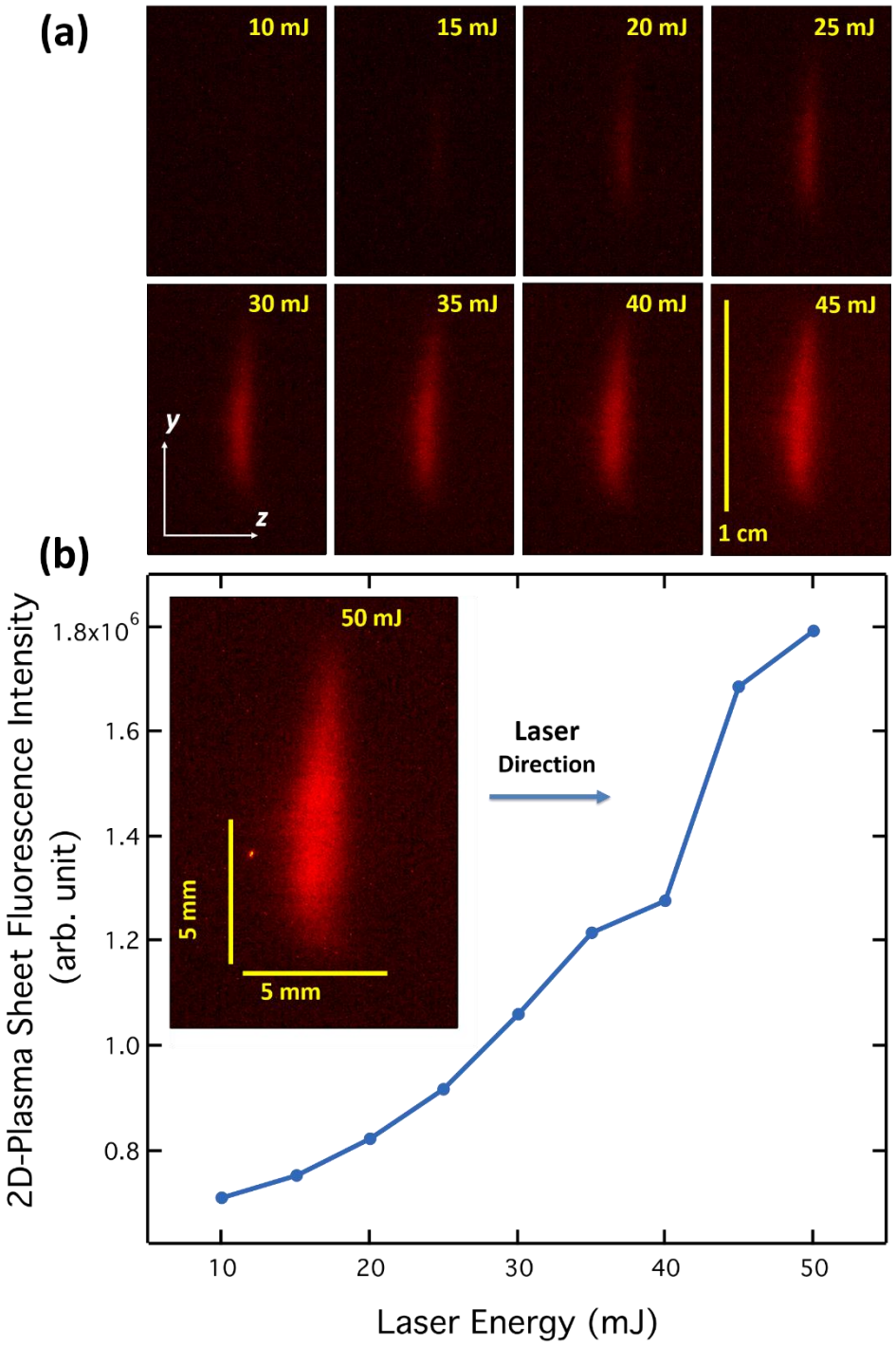

Figure 3.5 (a) A series of 2D plasma sheets imaged from the side (in the yz plane) with increasing laser energy. (b) Plasma fluorescence intensity as a function of laser energy. The inset shows a 2D plasma sheet imaged with laser energy of 50 mJ.

(a)

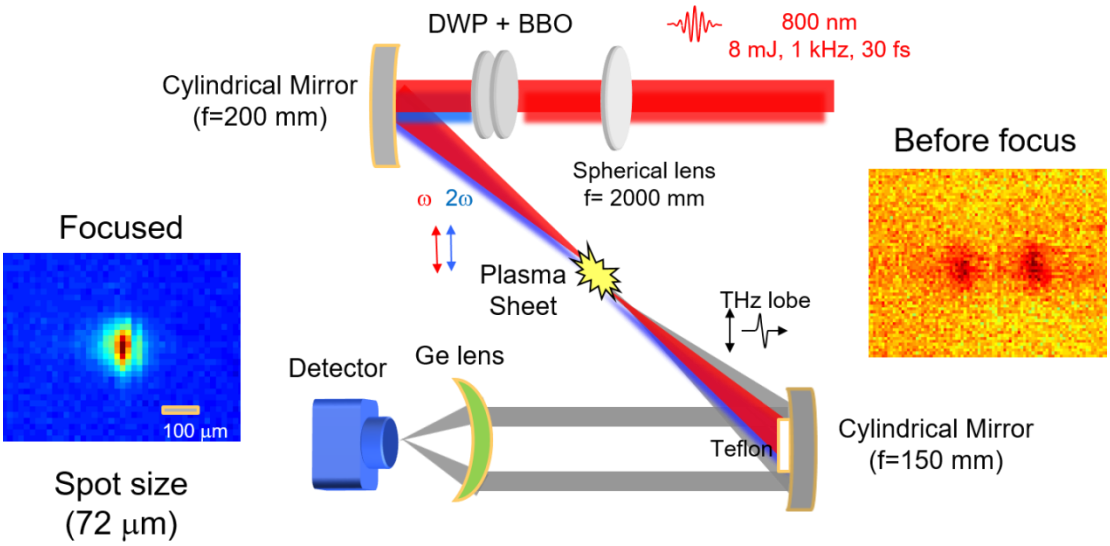

(b)

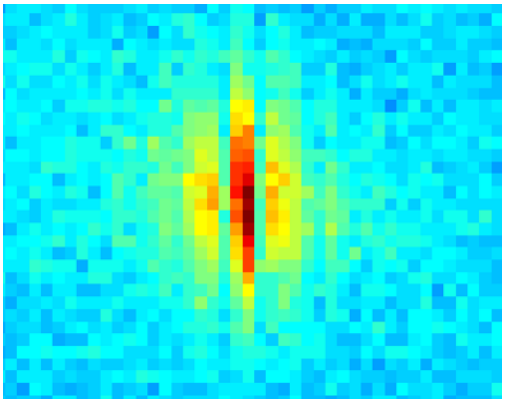

(c)

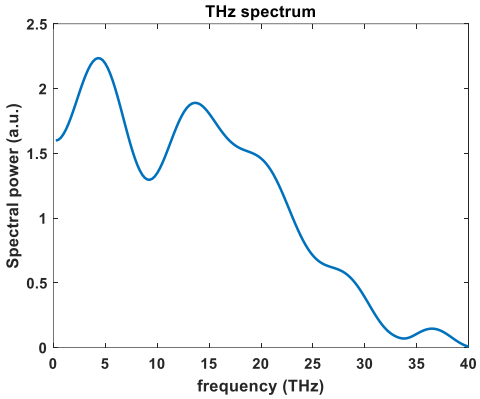

Figure 3.6 (a) System setup for single shot THz spectrometer. A pair of cylindrical mirrors are used to generate air plasma and collimate the generated THz beam. (b) THz fringe patterns formed on a microbolometer 2D array when two coherent THz beams are created. (c) Extracted THz spectrum from the fringe pattern.

Chapter 4 Intense terahertz generation in two-color laser filamentation and interaction with gases

4.1 Introduction

Two-color femtosecond laser mixing in air can produce high-energy (>μJ), high average power (>mW), broadband (0.01~100 THz) radiation [91-93]. In this two-color laser mixing scheme, an ultrashort laser pulse (ω) is focused with its second harmonic (2ω) in air to generate air plasma, and this can emit intense, single-cycle THz radiation in the forward direction. With this scheme, our group has recently generated intense THz fields exceeding 16 MV/cm at 1 kHz repetition rates [93]. We have also observed that long-length filamentation in air can greatly enhance THz output energy. In addition, the THz radiation emitted from long filamentation can be effectively refocused to a small spot size (<50 μm) [93]. However, the conversion efficiency from laser to THz remains relatively low (~10^{-4}) compared to optical rectification in crystals with tilted pulse front excitation (~10^{-3}) or with long-wavelength laser drivers (>10^{-3}).

In this chapter, we investigate long-length filamentation in various types of gases to improve the conversion efficiency in two-color laser mixing. In particular, we study the dependence of THz output yields on gas species and pressure conditions.

4.2 Experimental setup

Figure 4.1 shows our experimental setup for THz generation via two-color laser mixing inside a long gas tube. An 8-mJ, 30-fs, 800-nm, and 1-kHz laser pulse is focused by a long-focal-length lens (f = 1 m) into a gas tube of 1.75 m long. A type-I beta barium borate (BBO) crystal of 100 μm thickness is stacked with a thin (45 μm) dual wavelength (800 nm and 400 nm) half-wave plate and placed inside the gas tube to generate a second harmonic (2ω) pulse polarized parallel with the fundamental frequency (ω) pulse. These ω and 2ω pulses are focused together, generating a long plasma filament in the middle of the gas tube. This plasma filament works as a broadband source of radiation and emits coherent THz pulse in the forward direction. From previous research [91, 93], it is shown that long-length filamentation can effective mitigate plasma induced laser defocusing and give higher output THz energy compared to short-length focusing under the same laser condition. Here, we generate a long filament (~25 cm) by weakly focusing the incident laser beam with a long focal length lens (f = 1 m). To block the optical light and filter out THz radiation, a silicon (Si) window or thick (3 mm) white polyethylene window is placed at the end of the gas tube. The transmitted THz beam is refocused with two different schemes (see Fig. 4.1). One is to refocus by a germanium (Ge) lens of focal length f = 2" (top) and the other is by an off-axis parabolic mirror of focal length f = 2" (bottom). A small spot size (< 50 μm) near the diffraction limit is obtained by both ways. The first setup is more compact and easier to align THz beams, but provides an inherent energy loss of 70% due to Fresnel reflections and THz absorption in Ge. Here the emitted THz energy is measured by a pyro-electric (QS9-THZ-BL, Gentec-EO Inc) or thermopile detector (THz-12-3S-

VP, Gentec-EO Inc). Also, a microbolometer focal plane array (FPA) sensor (tau2, FLIR) is placed at the focus and used to characterize focused THz beam profiles.

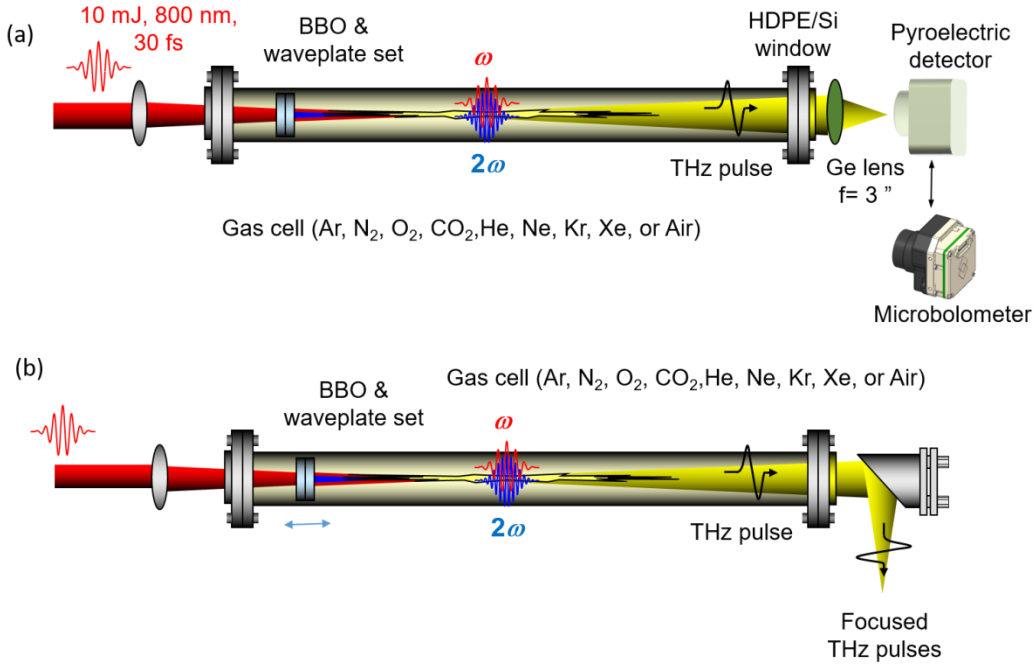

Figure 4.1 . Experimental setup for strong THz generation with long filamentation in a gas cell. Either Ge lens or off-axis parabolic mirror is used to refocus the emitted THz radiation onto a pyroelectric (or thermopile) detector or an uncooled microbolometer for imaging.

4.3 Results and discussion

4.3.1 THz energy pressure scanning with various types of gases

Figure 4.2(a) shows the output THz energy as a function of increasing gas (Ar) pressure at laser energy of 8 mJ. The output yield exhibits a periodic oscillatory behavior over the entire pressure range. The oscillation occurs due to dephasing between two-color (ω and 2ω) pulses when propagating through a density-varying gas.

As the gas pressure (or density) changes, the effective refractive index of the gas also varies for both ω and 2ω. Here the oscillation period is related to the dephasing length l_d, defined as the distance over which the THz radiation emitted along the filament has the same polarity. It is given by

$$l_d = (\lambda/2)(n_\omega - n_{2\omega})^{-1}, \quad (1)$$

where λ is the wavelength at ω and $n_\omega = n_{\omega,gas} + n_{\omega,plasma}$ is the index of refraction at ω. Then the oscillation period is $P = l_{d,1\,\mathrm{atm}}/d$ [atm], where $l_{d,1\,\mathrm{atm}}$ is the dephasing length at 1 atm, and $d = 0.55$ m is the distance between the BBO and the center of the filament. For Ar, $l_{d,1\,\mathrm{atm}} = 0.06$ atm, and the expected oscillation period is $P = 0.054$ atm. Compared to previous work on THz generation in a short-length gas cell [40, 48], our large d gives much faster oscillation periods.

In addition to the oscillations, the output THz energy gradually decreases with increasing pressure. This is due to a group-velocity walk-off between the ω and 2ω pulses. As the pressure increases, the temporal separation between the two pulses increases, prohibiting efficient THz generation. A temporal separation of ~20 fs already occurs in the BBO and half-wave plate, and it increases further as the two pulses propagate in the gas cell.

A beam walk-off can also occur in the transverse direction. It is shown that a high-repetition-rate (kHz) train of filamenting pulses can be self-steered by a gas density gradient created by successive laser heating and resulting buoyant motion of the heated gas [95]. At a 1-kHz repletion rate, this buoyance-induced self-steering can

occur even with sub-mJ of laser energy [95]. This density gradient can separate two-color laser pulses (ω and 2ω) in the transverse direction, where the 2ω pulse refracts more than the ω. This transverse separation increases with the gas pressure. Because of these longitudinal and transverse beam walk-offs, the output THz energy decreases with increasing gas pressure.

The output THz energy is observed to increase almost linearly with the input laser energy for both room air and Ar cases (see Fig. 4.2(b)). With tight refocusing, the emitted THz radiation can be focused into a spot size of <50 μm (see the inset to Fig. 4.2(b)) even in long-length filamentation.

To verify that the damped oscillatory behavior is caused by the dephasing and walk-off effects, we have tested different types of gases for THz generation. Figure 4.3 shows a result of pressure scans obtained with room air, helium (He), neon (Ne), krypton (Kr), xenon (Xe), nitrogen (N_2), oxygen (O_2), and carbon dioxide (CO_2). All gases show clear oscillations but with different oscillation periods. Since Xe is the most dispersive material among the gases we tested, it shows the fastest oscillation period. On the other hand, He is the least dispersive gas, and its oscillation period is the longest among the gases. Table 1 shows our measured and expected values of the oscillation period in atm.

With 8 mJ of laser input energy, we can generate 9.6 μJ of maximum THz energy with low pressure Ar. This provides a conversion efficiency of 1.2×10^{-3} which is more than 10 times greater than conventional two-color laser mixing sources ($\sim 10^{-4}$). To characterize the field strength of the radiation when refocused, we measure the pulse duration with Electro-Optic sampling (EO-sampling). To minimize THz

absorption/dispersion in the sampling crystal and thus to maximize the detectable frequency range, we use thin (100 μm thickness) GaP as a detection crystal.

(a)

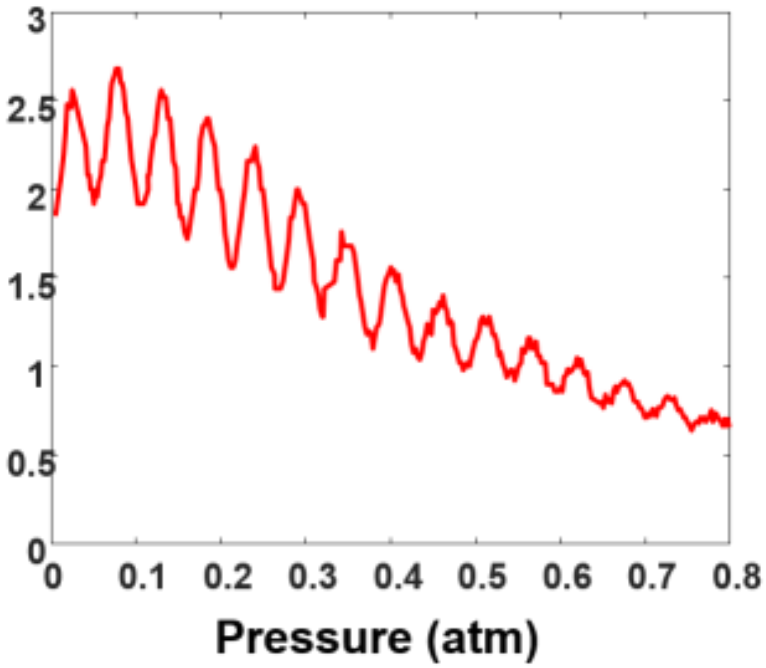

(b)

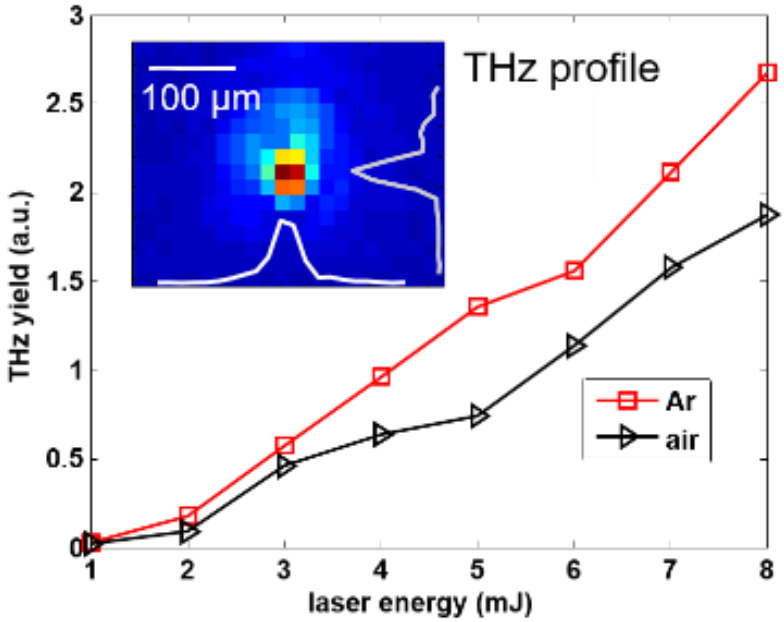

Figure 4.2 (a) THz output signal as a function of Ar pressure inside the gas cell at input laser energy of 8 mJ. (b) THz output signal as a function of laser input energy for Ar at 500 Torr (squares) and room air (triangles). The inset shows a refocused THz beam profile on the microbolometer.

Figure 4.4 shows a measured THz waveform (pulse duration of 200 fs) and the corresponding spectrum obtained by Fourier transformation. Since GaP has strong absorption above 10 THz, the spectrum beyond 10 THz is not captured by EOS. To overcome this limitation, we use a pyro-electric detector along with THz bandpass filters to characterize the higher frequency components of the spectrum (see Fig. 4.4). To measure THz radiation at <40 THz, a THz low frequency pass filter (<40 THz) is placed in front of the pyro-electric detector. In both methods, 8 mJ of laser input energy is used along with Ar gas at 0.05 atm which gives the highest THz output energy. With a combination of the measured THz energy, spot size and pulse duration, we can characterize a maximum THz field of 30 MV/cm at the focus.

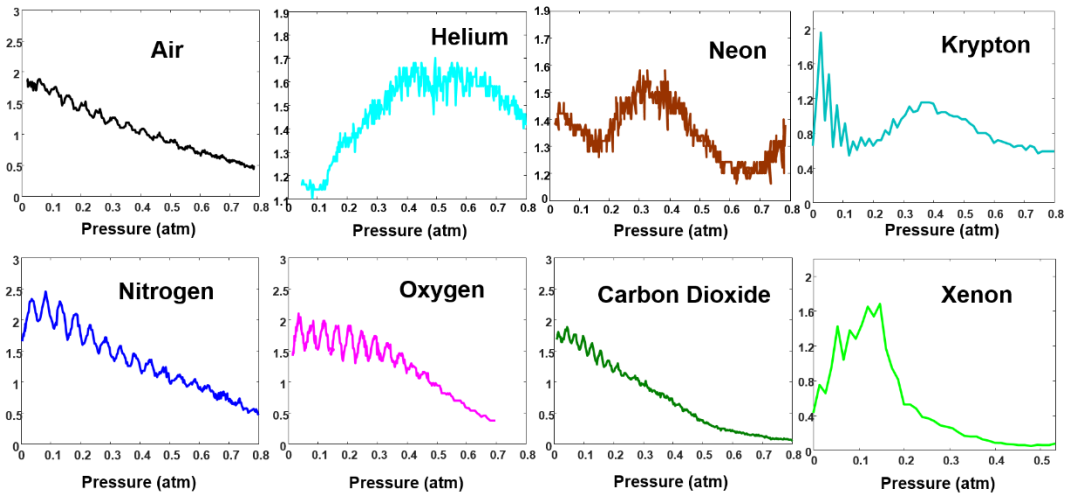

Figure 4.3 THz yield as a function of pressure up to 0.8 atm from different types of gases (air, He, Ne, Kr, N_2, O_2, CO_2, and Xe) at 8 mJ of laser input energy.

Gas	Calculated (atm)	Measured (atm)
Air	0.047	0.047
Nitrogen	0.050	0.049
Oxygen	0.040	0.042
Carbon Dioxide	0.025	0.028
Argon	0.054	0.054
Neon	5.757	5.622
Helium	13.624	13.489

Table 1. Summary of oscillation period of THz yield according to the pressure change among different gases. Theoretical values and experimental values are compared.

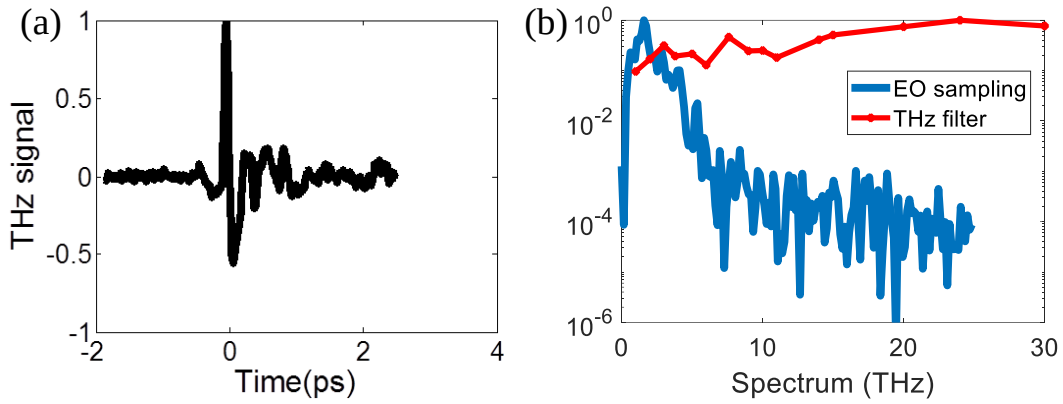

Figure 4.4 (a) THz waveform measured by Electro-Optic Sampling with 100 μm thickness GaP at 8 mJ of laser energy. (b) THz spectrum by its Fourier Transform from the waveform (solid blue) and measured by pyro-electric detector along with THz bandpass filters (solid red).

4.3.2 Plasma fluorescence analysis

As a supplementary experiment, we have investigated fluorescence emitted from plasma filaments created by two-color laser pulses inside the gas cell. Figure 4.5(a) shows fluorescence images taken at various Ar pressures with input laser energy of 6 mJ at 1 kHz. For this imaging, a webcam is used and placed ~0.6 m away from the transparent gas tube. Both output THz energy and fluorescence image are taken at every 0.002 bar increment. A single long filament is formed at 0.02~0.36 bar with a maximum length of ~30 cm. Above 0.4 bar, the filament appears to break into two segments, which is an evidence of plasma defocusing and laser refocusing. Figure 4.5(b) shows the brightness and length of filaments with increasing Ar gas pressure. Here the brightness signal is obtained by considering the entire filament length.

Interestingly, the filament is quite bright at low pressures. It peaks at 0.1 bar and decreases with pressure until it rises at 0.8 bar. Note that at high pressures (>0.7 bar), there are artifacts arising in the signal due to strong supercontinuum generation

and scattering. The reasons why the filament is bright and more THz energy is emitted *at low pressures* are as follows. Firstly, more ionization occurs due to less walk-off between 800 nm and 400 nm pulses at low pressures. Secondly, the filament transverse size becomes large with decreasing pressure [78]. This is because the critical power for filamentation increases with decreasing pressure, but the maximum clamped intensity remains independent of the pressure [78]. All these effects result in more ionized electrons at low pressures.

In addition, clear oscillations are observed in both filament brightness and length at low pressures (0.02~0.5 bar). Their oscillations are in phase with the same period. Like the THz energy shown in Fig. 4.2(a), those oscillations are caused by dispersion between 800 nm and 400 nm as the pressure changes.

All these observations show that low pressure filamentation is favorable for high-energy THz generation.

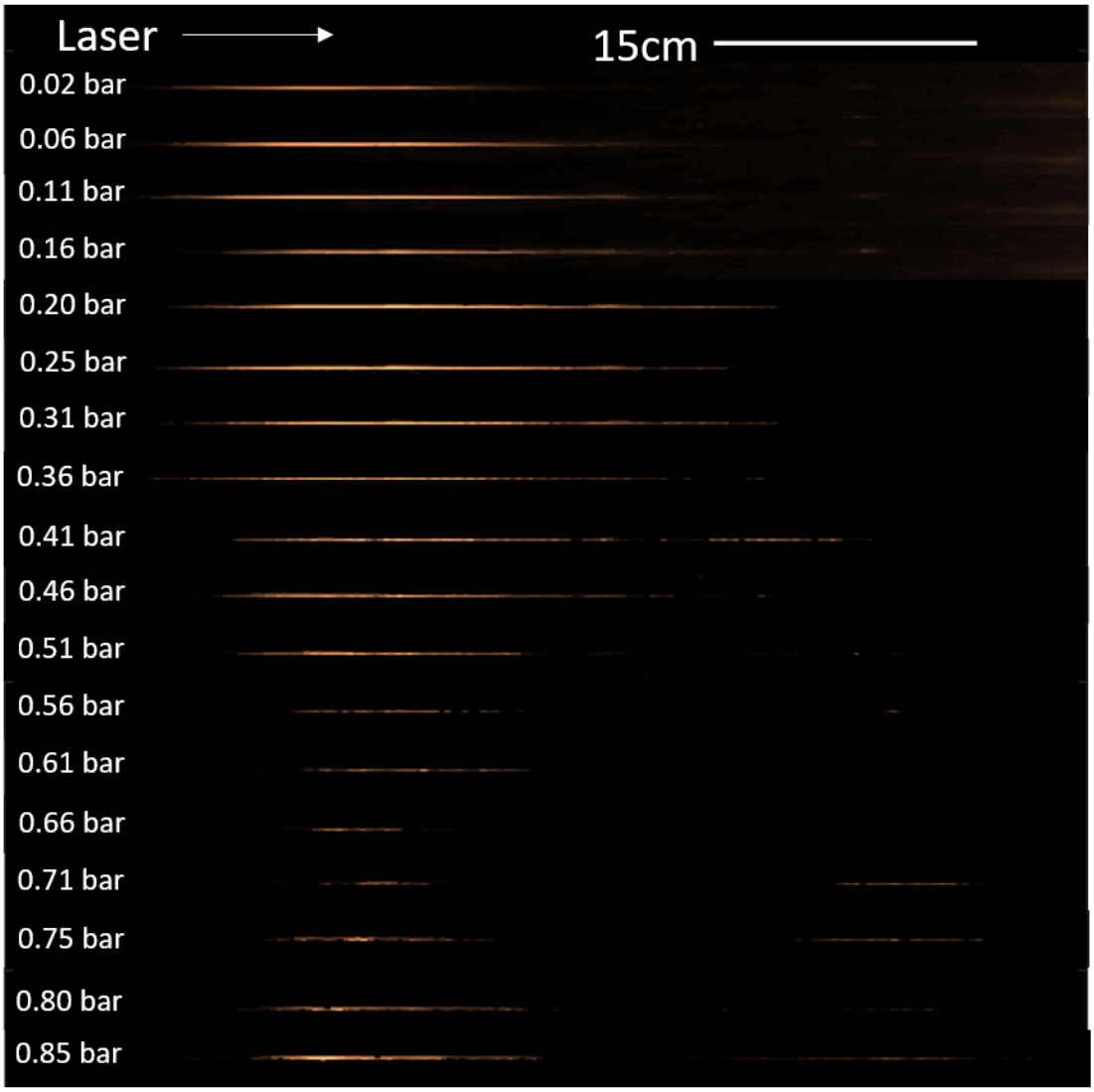
Laser
15cm
0.02 bar
0.06 bar
0.11 bar
0.16 bar
0.20 bar
0.25 bar
0.31 bar
0.36 bar
0.41 bar
0.46 bar
0.51 bar
0.56 bar
0.61 bar
0.66 bar
0.71 bar
0.75 bar
0.80 bar
0.85 bar

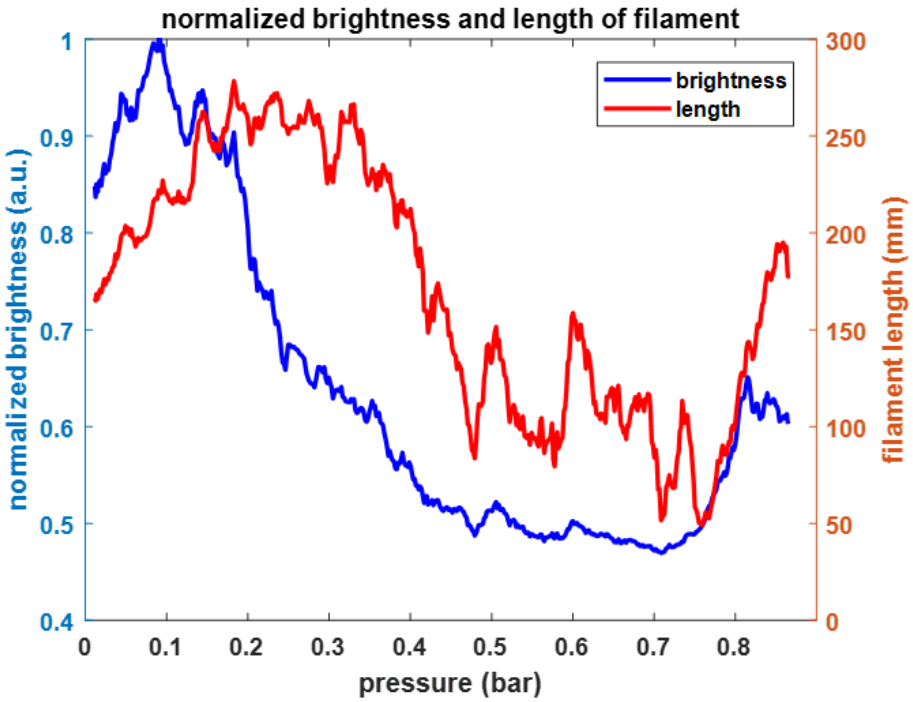

Figure 4.5 (a) Images of plasma fluorescence obtained with 6 mJ of laser input energy at various Ar pressures (top). (b) The brightness of the plasma fluorescence (blue) and the plasma filament length (red) at each pressure.

4.4 Conclusion

In chapter 4, we have discussed intense THz generation with two-color laser filamentation inside a long gas-cell filled with different types of gases. We present a method to generate and characterize high field THz radiation (>30 MV/cm). We increase the output THz energy by generating a long filament (~ 25 cm) as a THz source to mitigate plasma-induced laser defocusing. Also, to minimize the walk-off between the original and second harmonic pulses, we have used a less dispersive gas (Ar) as a source at low pressure (~0.05 atm). With this scheme, we can reach high conversion efficiency (> 10^{-3}).

Chapter 5 : Broadband THz generation from optical rectification in large band-gap crystals

5.1 Introduction to optical rectification

Non-negligible THz radiation can be generated directly from a frequency doubling crystal (BBO) placed in the beam path to generate the second harmonic (400 nm) pulses for two-color laser mixing. This radiation arises due to optical rectification inside the crystal ($\chi^{(2)}$ effect). Figure 5.1 shows two measured THz beam profiles obtained with two-color laser mixing in air. In our conventional two-color laser mixing used in Chapter 2, it is quite difficult to detect THz radiation directly emitted from the BBO crystal ($\chi^{(2)}$ effect) since the radiation from the plasma is much more intense than that from the crystal itself. However, by tilting the BBO crystal in the horizontal direction, we can slightly deviate the beam paths for those two types of radiation, and they become separable near on the focal plane. To verify that the left radiation is not generated from the plasma but from the crystal, we put a Si filter before the plasma and block the optical beam. Then the beam on the right side disappears, but the left side beam still remains. In addition, to see if the left radiation is generated directly from the crystal, we perform two different tests. First, when we remove the BBO from the beam path, we observe that the beam suddenly disappears. This shows that this beam is generated from the crystal itself. Second, to see if this is not from any thermal effect by laser heating, we rotate the angle of the BBO and find out that the beam intensity depends on the angle of the BBO, and the beam completely disappears at a certain angle.

This shows that this radiation is coherent and not from a thermal effect by the laser. In this chapter, we generalize this method to generate and characterize THz radiation directly generated from nonlinear crystals via optical rectification ($\chi^{(2)}$ effect). After testing various types of large bandgap crystals (BBO, GaP, $LiTaO_3$, $LiNbO_3$), we find that x-cut $LiNbO_3$ gives the highest output THz energy. Therefore, we mainly study THz radiation and beam characterization using x-cut $LiNbO_3$ as a THz source. For THz beam characterization, we measure THz energy, beam spot size, pulse duration and spectrum.

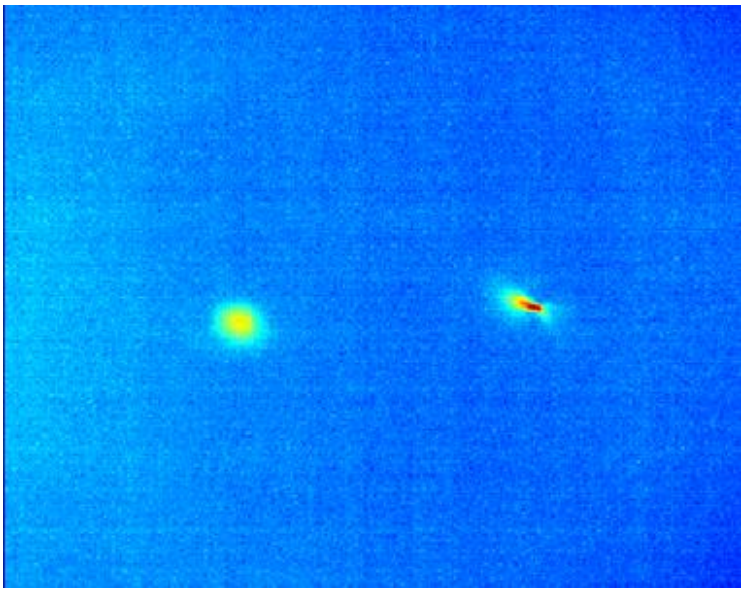

Figure 5.1 THz beams generated from optical rectification inside the BBO crystal (left) and two-color laser mixing form the plasma (right).

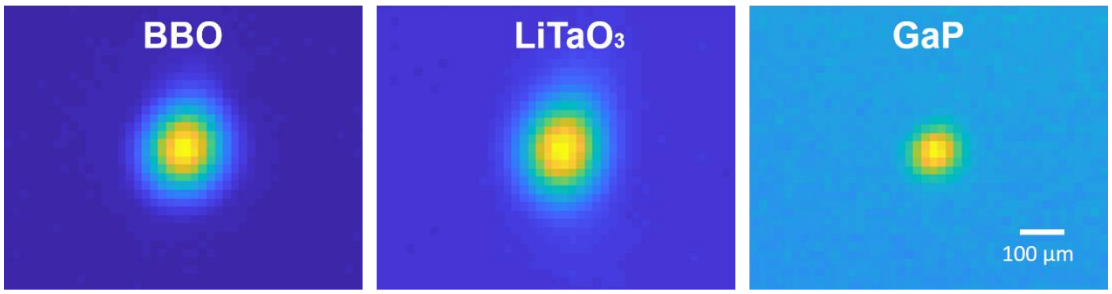

Figure 5.2 Experimental measurement of THz beams directly generated from nonlinear crystals (BBO, LiTaO3, and GaP) via optical rectification.

5.1.1 Experimental setup

We present high energy, broadband terahertz (THz) generation using a planar $LiNbO_3$ (x-cut/y-cut) crystal via optical rectification. Figure 5.3 shows our experimental setup. In this experiment, 800-nm, 8-mJ, 1-kHz, and 30-fs laser pulses are gradually focused by a lens (f=1.5 m) onto a planar $LiNbO_3$ crystal, which works as a THz source. After the sample crystal, a high-density polyethylene (HDPE) filter of 1.5 mm thickness and a Si wafer are placed in the beam path. When the Si wafer is illuminated by light of photon energy greater than the bandgap of Si (1.1 eV), then the valance electrons in Si are excited to the conduction band, generating charge carriers (both electrons and holes). These charge carriers can efficiently screen low-energy THz photons, greatly attenuating THz transmission. We also note that the group velocity of 800 nm pulse is greater than that of THz radiation inside the $LiNbO_3$ crystal. This means that the 800 nm laser pulse arrives first on the Si wafer and generates charge carriers before the THz pulse arrives. Here a HDPE filter is used to attenuate laser intensity and minimize the generation of charge carriers on the Si wafer. By placing a HDPE filter with proper-thickness, we can significantly enhance THz transmission. To minimize charge carrier generation and enhance THz transmission even further, we use an ITO beamsplitter to transmit most of optical laser energy but reflect THz radiation. Only a small portion of optical beam is mixed with THz radiation and passes through the HDPE filter and Si wafer. Therefore, we can minimize the intensity of laser beam

on the Si wafer and thus enhance the transmission of THz radiation. After the Si wafer, the optical beam is fully blocked and only THz components exist. This filtered THz radiation is refocused by an off-axis parabolic mirror of f=4" and detected by a pyro-electric or microbolometer detector. To characterize the spectrum of the radiation, various types of THz bandpass filters are placed in front of the detector.

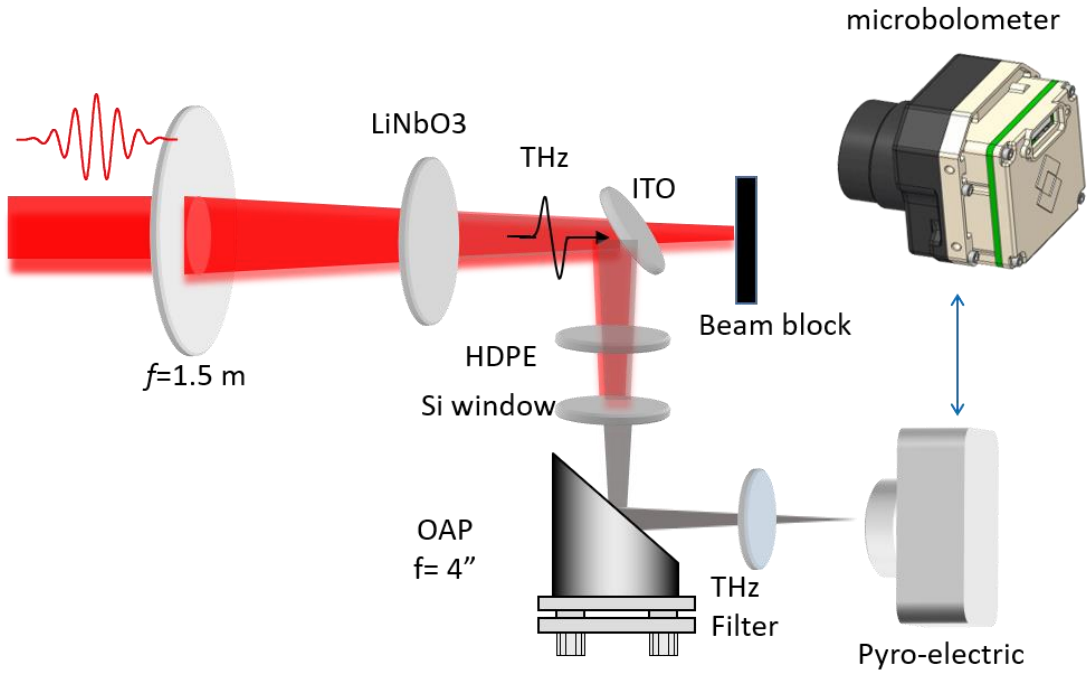

Figure 5.3 System setup for broadband THz generation from optical rectification inside a planar $LiNbO_3$ crystal.

To confirm that the detected radiation is not from a thermal effect, we measure the output THz energy by rotating the $LiNbO_3$ crystal (Fig.5.3). As we can see from Fig. 5.4, there is a strong dependency between the detected THz energy and the angle of the crystal. Also if we get rid of the crystal from the beam path, no signal is detected. Therefore, we can conclude that this signal is generated from the crystal itself and this radiation is coherent. This effect is also observed with other non-centrosymmetric crystals such as BBO and GaP.

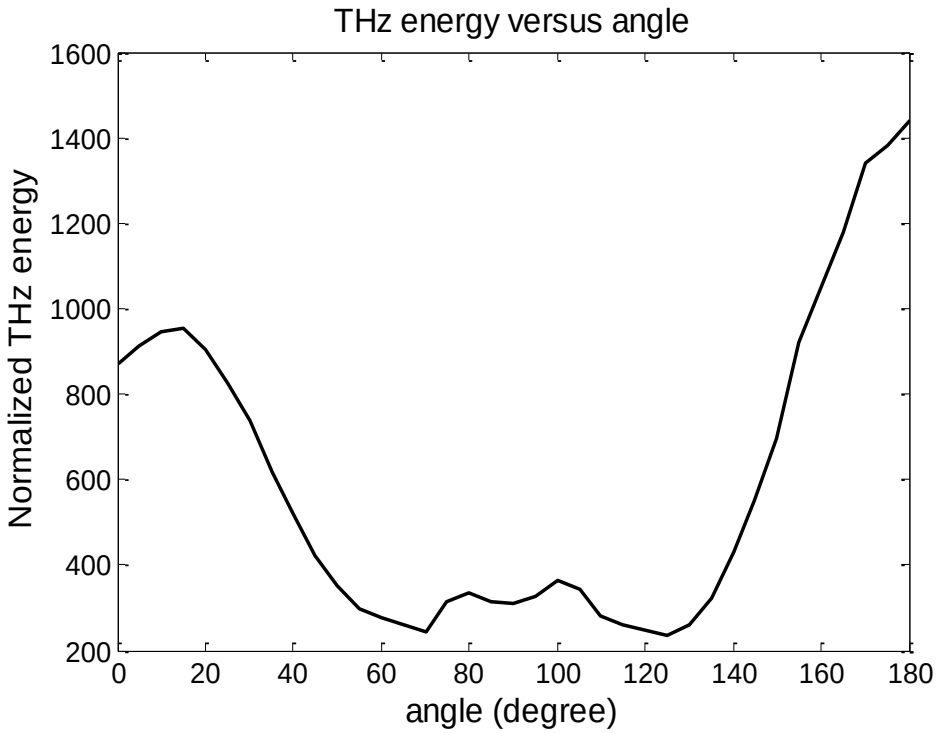

(b)

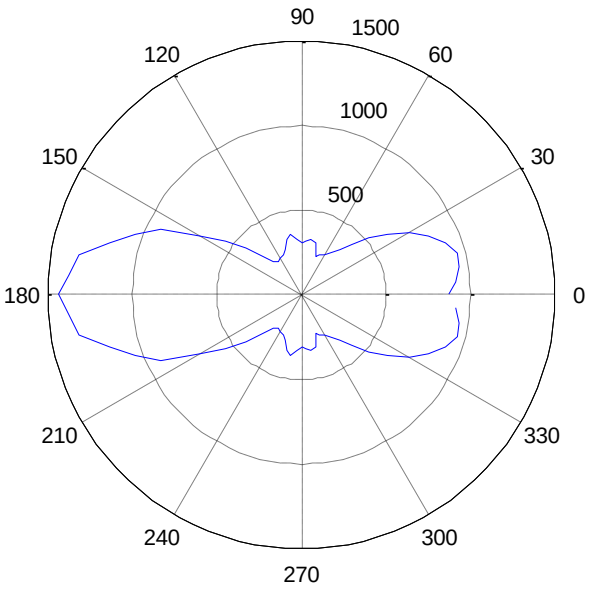

Figure 5.4 Angular scan of THz energy from optical rectification inside planar $LiNbO_3$ in (a) Cartesian coordinates and in (b) polar coordinates.

5.1.2 Broadband THz energy measurement and spectrum characterization

To characterize the radiation, we first measure THz energy with a pyro-electric or thermopile detector. For the experiment performed here, 1-kHz laser pulses are chopped at 10 Hz, and the pyroelectric detector provides a calibration value of 0.03 μJ/V per pulse. With a thermopile detector, we can directly measure THz power with pre-calibrated setting.

To extract the maximum energy from the given setup, we control the laser fluence on the crystal by changing incident laser energy with three different lens positions. We find that the output THz yield is strongly dependent of the input laser fluence on the crystal. Figure 5.5 shows an energy scan result with (a) 0.5-mm thickness and (b) 1-mm thickness x-cut $LiNbO_3$ crystals at three different lens positions. With the thin crystal (0.5 mm thickness), we find out that the higher input laser fluence gives the more output THz yield, and the THz output energy increases with the input laser energy. As a result, we have achieved a maximum THz energy (0.5 μJ) at 8 mJ of laser input energy, and this corresponds to the energy conversion efficiency of 7×10^{-5}. However, in the case of the thick crystal (1 mm thickness), we observe that the output signal saturates with Lens Position 3 when gives the largest laser fluence. The reason for this saturation, in particular with the thick crystal, is due to higher THz absorption inside the crystal. When the beam propagation distance gets longer, then the generated THz beam experiences more attenuation while passing through the crystal. Therefore, for broadband and scalable THz generation, it is favorable to use a thin crystal with high input laser fluence on the crystal surface.

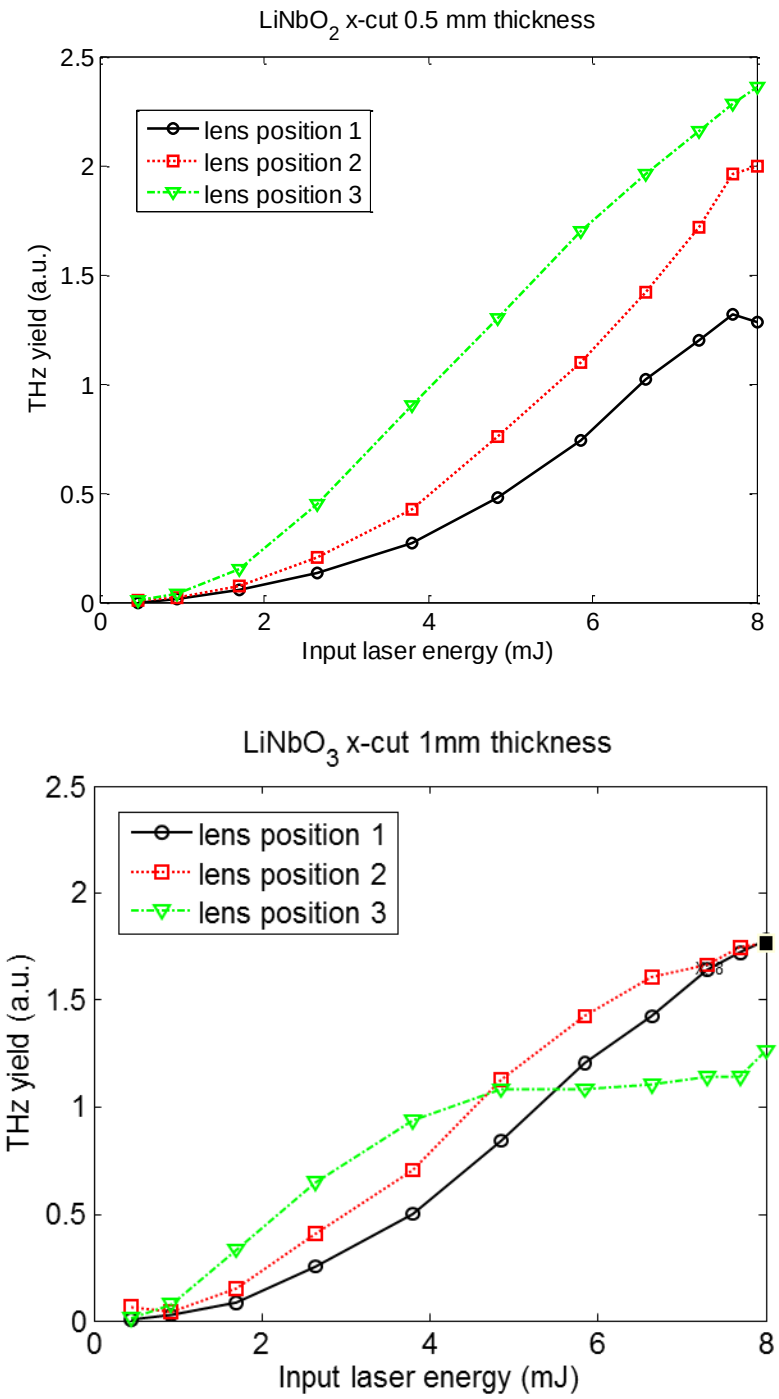

Figure 5.5 Experimental measurement of THz energy with different lens position and input laser energy. Results from different thickness (0.5 mm (top) and 1 mm (bottom)) of $LiNbO_3$ are presented.

In addition, we use THz bandpass filters to characterize the spectrum of 1-30 THz (Fig.5.2). In this experiment, 15 sets of bandpass THz filters (Thorlabs, FB19M series) are individually used to characterize the radiation spectrum. One major issue with the THz filters is that they do not provide ideal bandpass transmission over the entire THz frequency band. Rather they exhibit a large amount of unwanted transmission at both low and high THz frequencies. Therefore, any directly measured value does not represent the real spectral intensity at the given THz filter frequency. Here, we use two different methods (zeroth order and matrix based calculations) to characterize the real THz spectrum with non-ideal THz bandpass filters. Details about these methods are provided in the Appendix B. Figure 5.6 shows the spectral intensity measured with two different cuts ((a) for x-cut and (b) for y-cut), also characterized by applying the zeroth order and matrix based calculations, respectively. Interestingly, there exists a narrow and sharp peak around 15 THz both for x-cut and y-cut, and this was never observed previously. There are some negative values for the matrix based method (red line with circles). This occasionally occurs due to imperfect measurements, and those values can be simply considered to be zero (see Appendix B).

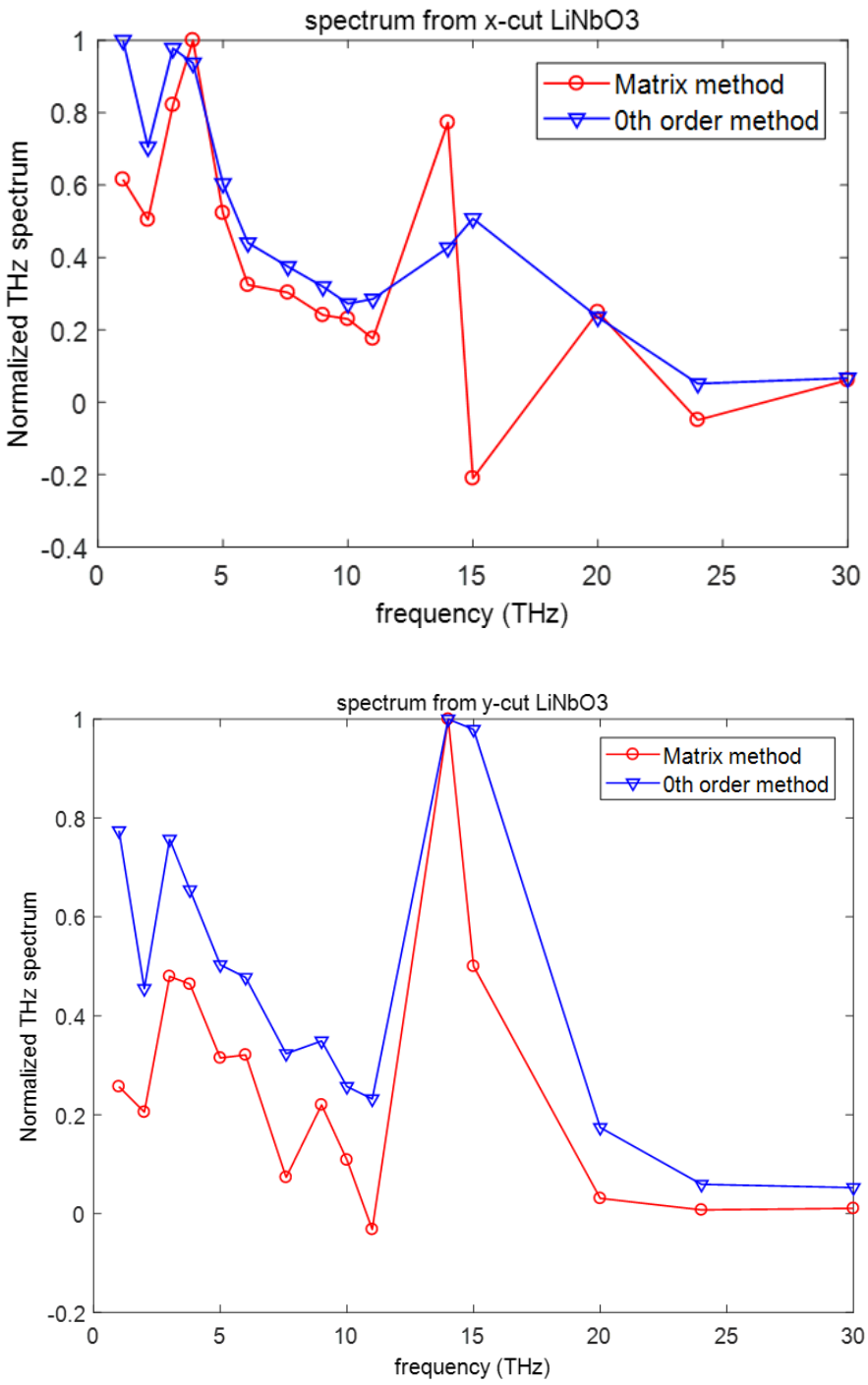

Figure 5.6 Broadband THz spectrum (0~30 THz) extracted from energy measurements along with THz bandpass filters. Two different methods (zeroth order method (blue triangles) and matrix based calculation (red circles)) are applied to x-cut (top) and y-cut (bottom) $LiNbO_3$ crystals.

5.1.3 THz beam spot size measurement

To obtain 2-D THz beam profiles and thus determine THz spot sizes, we used an uncooled microbolometer camera. In this section, we compare the result of THz beam spots obtained with different $LiNbO_3$ thickness and cut at different input laser fluence on the front surface of the crystal. Figure 5.7 shows typical THz beam profiles captured by the microbolometer. As we can see from the figure, the THz beam spot size is not much dependent of the thickness of the crystal but to the lens position. The minimum spot size is about 140 μm, and this is about 3.5 times bigger than that of two-color laser mixing case. The reason why it shows larger spot sizes is because the radiation from optical rectification contains lower frequency components compared to the two color laser mixing case. However, the measured spot size is much smaller than the case of the tilted pulse front scheme. Therefore, we can expect that this radiation contains the higher frequency components and generates the broader range of spectrum than the tilted pulse front scheme.

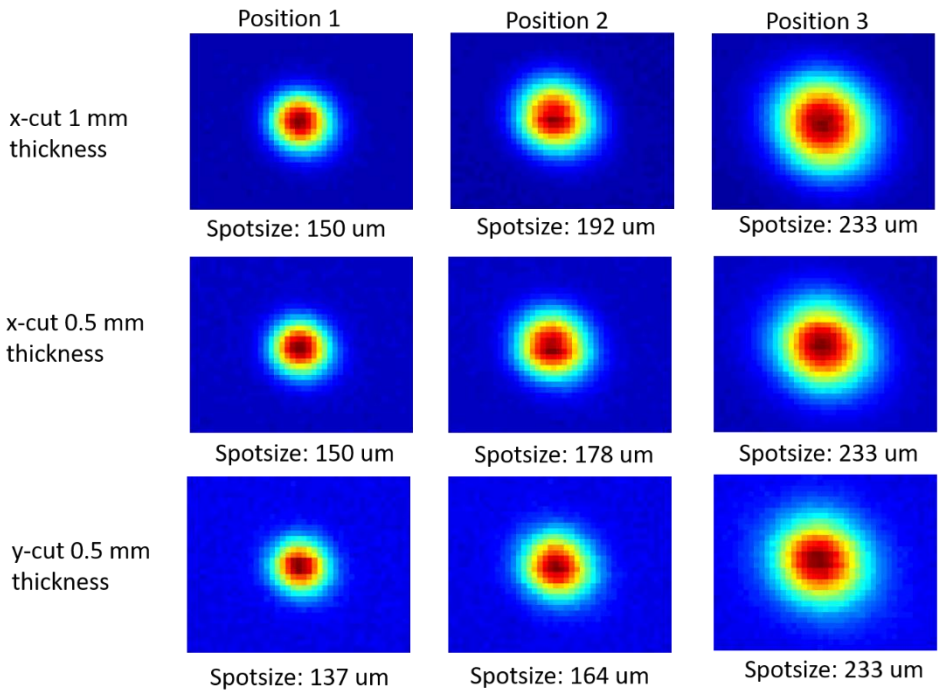

Figure 5.7 Experimental measurement of THz beam profile and spot size at the focus. THz beam spot with different thickness (1 mm and 0.5 mm), different cut (x-cut and y-cut) of $LiNbO_3$ and with different fluences (three different lens positions) are presented.

5.1.4 Pulse waveform and spectrum measurement

The last component to characterize the focused THz field strength is the pulse duration. We can measure a THz waveform via Electro-Optic Sampling (EOS) with a birefringent crystal such as ZnTe or GaP. Since we want to detect broadband THz radiation, we use a thin (100 μm thickness) GaP as a detection crystal to minimize THz absorption/dispersion and thus to maximize the detection bandwidth. EOS is widely used in characterizing broadband THz waves because it can measure THz waveforms in a direct way. Figure 5.8 shows a measured waveform and its corresponding spectrum. Interestingly, the waveform contains two peaks which are apart about 1 ps. The first peak corresponds to the THz pulse generated from the back surface of the crystal and

the other is from the first surface. This is because the group velocity at 800 nm is greater than that at 1~10 THz in $LiNbO_3$. Any THz waves generated in between the two surfaces are cancelled because they are not phase matched. Unfortunately, our GaP based EOS measurement is limited to ~10 THz and thus does not show the spectral peak around 15 THz, previously observed with THz bandpass filters. Therefore, to confirm the spectral peak around 15 THz is real, we need to apply a different scheme which can expand the detection bandwidth to a higher range of spectrum.

For this, we use Fourier-transform infrared spectroscopy (FTIR) with a Michelson type interferometer since this method is less vulnerable to THz absorption and has a much broader detection bandwidth. Figure 5.9 shows a result of FTIR measurement, and we can clearly see a high peak around 15 THz.

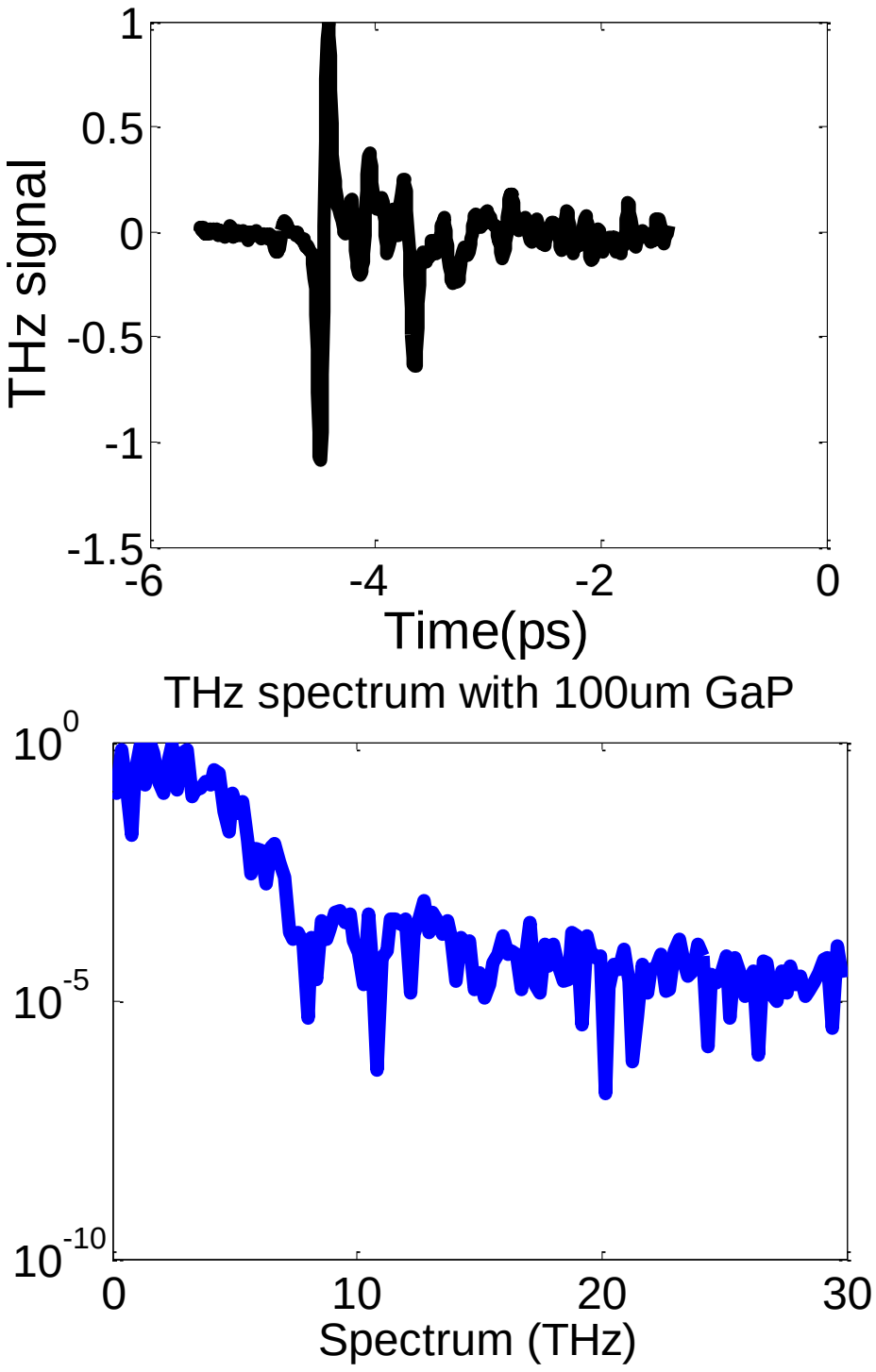

Figure 5.8 THz waveform (top) and its extracted spectrum (bottom) from Electro-Optic Sampling with a thin (100 μm thickness) GaP.

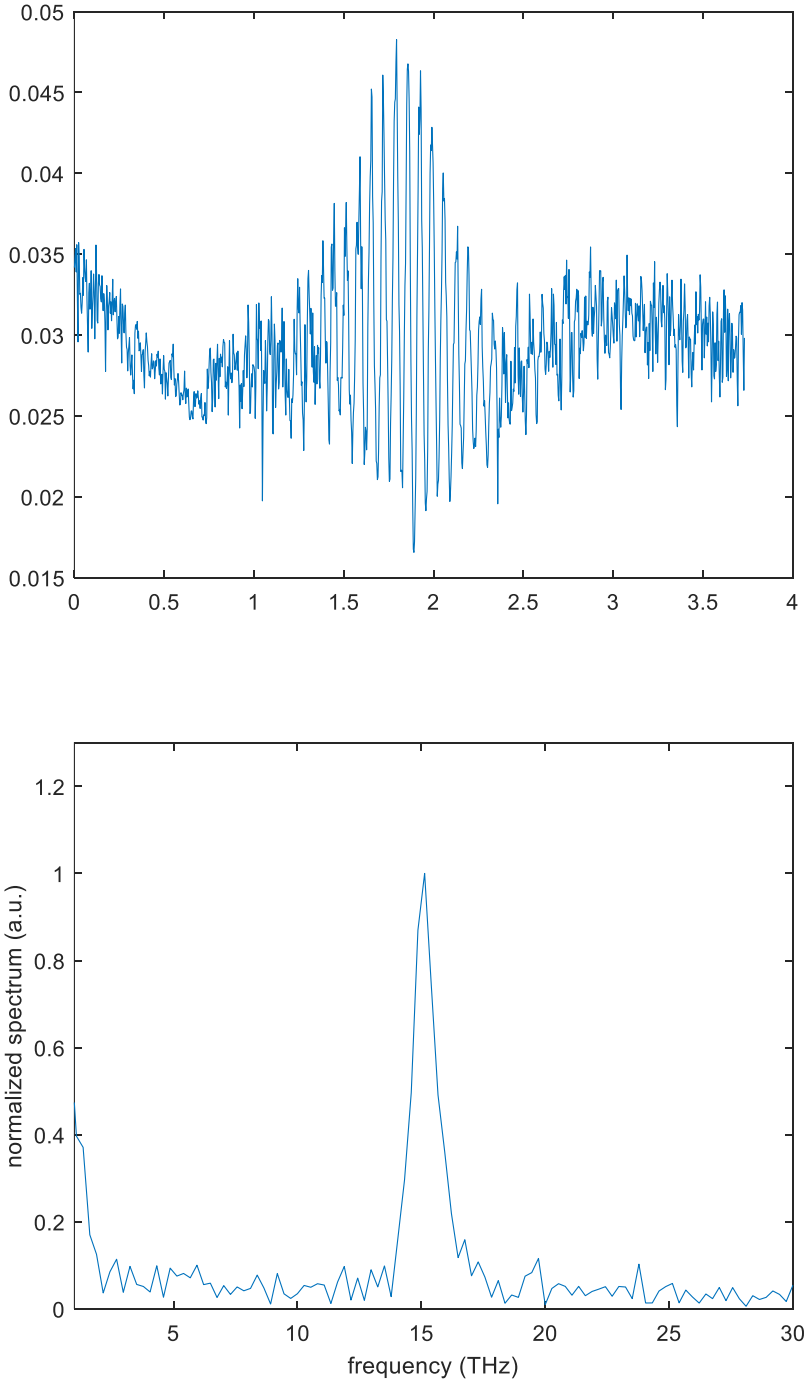

Figure 5.9 THz autocorrelation trace taken with Fourier-transform infrared spectroscopy (FTIR) using a Michelson type interferometer (top) and its corresponding spectrum (bottom).

5.2 Summary of broadband THz generation from large bandgap crystals

As we mentioned, optical rectification from planar $LiNbO_3$ can generate THz radiation at a relatively broad range, covering from 0 to 20 THz. We introduced various ways to characterize this THz beam to calculate the field strength at the focus. At first, we measure output THz energy with pyro-electric/thermopile detectors. With a thin (0.5 mm thickness) x-cut $LiNbO_3$ crystal we observe scalable THz generation even with high laser input energy. From this method, we can generate 0.5 μJ of maximum THz energy with 8 mJ of input laser energy, and the corresponding energy conversion efficiency is about 7×10^{-5}. The conversion efficiency of this non-phase-matched terahertz (THz) generation in planar $LiNbO_3$ is lower compared to two-color laser mixing, but it provides much stable THz outputs.

Second, we can measure the resulting THz beam profile and THz beam spot size by using a microbolometer camera. The minimum THz beam spot size we measured from this scheme is 140 μm, and this value lies between the minimum spot size obtained by the two color laser mixing method (~40 μm) and tilted pulse front scheme (~300 μm). This implies that the radiation bandwidth from this scheme is much broader than the tilted pulse front scheme but narrower than two-color femtosecond filamentation in air.

Third, we characterize the pulse duration of emitted THz pulse and the radiation spectrum by Electro-Optic Sampling. To maximize the detection bandwidth, we use thin (100-μm thickness) GaP as a detection crystal. Interestingly, we see two, single-cycle peaks in the waveform, and those are generated from the front and back surfaces of the crystal, respectively. Each cycle of the peaks has a duration of 200 fs. By

applying a Fourier transform of each pulse, we get a radiation spectrum up to 10 THz. However, this method cannot detect high frequency components (>10 THz) due to THz absorption/dispersion and optical/THz walk-off in the detection crystal. To complement this, we directly measure the output THz energy along with narrowband THz bandpass filters and characterized the higher frequency components. As expected, we can see a narrowband peak around 15 THz which was not detected with Electro-Optic Sampling. To detect even further broadband radiation, a FTIR method is applied. With FTIR, we can detect an even broader range of radiation spectrum and also confirm the presence of the peak around 15 THz.

By combining the results we have measured, we can characterize the field strength (~2 MV/cm) at the focus. Even though this value is much lower than that provided by two-color laser mixing, this scheme can generate much more stable THz radiation with a simpler setup.

Chapter 6 : Summary and outlook for high field THz generation

6.1 Summary and outlook for high field THz generation from two-color laser mixing

In this section, we summarize our work and discuss an outlook for high field THz generation from two-color laser mixing and possible methods for further improvement. From our experimental results, we have proved that long filamentation is favorable for high conversion efficiencies since it helps in suppressing plasma-induced defocusing. By optimizing the filament length, gas species, and gas pressure, we have achieved laser-to-THz conversion efficiency of $>10^{-3}$, ten times greater compared to conventional two-color laser mixing in air. In addition, a small spot size near its diffraction limit (~40 μm) can be obtained by tight focusing even when the plasma filament (THz source) is long. Therefore, a large volume of plasma filament (either longitudinal or transverse) is favorable for high-energy THz generation. According to our experimental data, 8 mJ of laser input energy yields ~9.6 μJ of THz energy with an optimal filament length (~25 cm), proper gas species (less dispersive gas such as Ar), and optimized gas pressure (~0.05 atm for Ar). If we scale up the laser input energy up to 1 J, more than 1 mJ of THz energy can be achieved theoretically. Then the corresponding field strength at the focus will approach 300 MV/cm at the focus if the same spot size and pulse duration are maintained. However, the maximum achievable THz energy is restricted by the longitudinal and transverse walk-offs between two-color laser pulses, especially when we use a long filament as a source. For instance, if two 50 fs laser pulses of wavelength 800 nm and 400 nm propagate

together in air, those pulses will totally get separated in time after about 4 m of propagation [52]. This dispersion limits the output THz energy fundamentally. Also, from our experiment, we can see a huge oscillation as the pressure changes. This behavior is more evident at low pressures. Even though a low-pressure gas yield low electron density (thus less current surge for THz generation), it has a benefit of providing less walk-off. Since we are using long filamentation as a source, this walk-off effect is a critical factor in obtaining high output THz energy. At the same time, we do not fully utilize the advantage of producing a strong THz source at high gas pressures. Therefore, with a proper control of the walk-off between two pulses even in the high pressure regime, it is possible to increase the output THz energy even more.

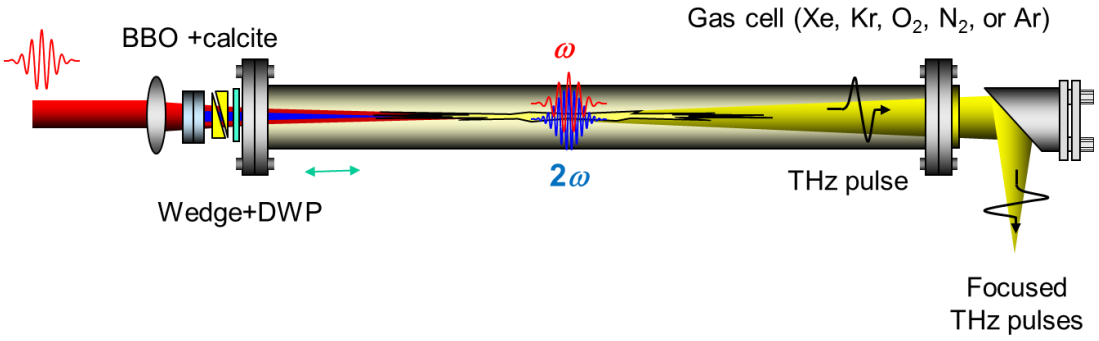

Figure 6.1 Experimental setup for high field THz generation inside a long gas cell. The separation between the two-color pulses (800 nm and 400 nm) can be effectively controlled by adding a calcite window which provides a pre-compensated negative walk-off and two movable wedged windows (fused silica) providing both phase and positive walk-off controls.

Figure 6.1 shows a proposed setup for high field THz generation. Here the relative phase and walk-off between 800 nm and 400 nm (produced by the first BBO) is controlled in the following manner. First, the BBO and waveplate are located out of the gas cell for a fine control of the crystal angles (tilt and azimuth). A calcite window

is placed right after the BBO to compensate the walk-off caused by the BBO and also to pre-compensate additional walk-offs to be induced by the gas cell window and two window wedges. One of the wedges can be translated in the transverse direction to control both the relative phase and walk-off between 800 nm and 400 nm for optimal THz generation even at high gas pressure (0.1~1 atm). Based on our previous results with short-length focusing, we anticipate a dramatic enhancement of THz output energy with noble gases at relatively high pressure [39,48,74].

6.2 Summary and outlook for intense THz generation from optical rectification

THz generation from optical rectification has been widely used among the scientists since it can be implemented with a simple setup. In most cases, however, the generated radiation spectrum is limited < 3THz. However, in our scheme, we use a thin (0.5 mm), large bandgap crystal to minimize THz absorption/dispersion inside the crystal and to withstand high incident laser power. Especially, we find that $LiNbO_3$ can generate intense THz radiation with relative high efficiency approaching 10^{-4} and bandwidth ranging up to 20 THz.

The maximum output THz energy we have achieved is about 0.5 μJ, but this is much lower than the typical energy produced by the tilted pulse front or two-color laser mixing methods with the same laser input energy. For efficient phase matching at ~1 THz in $LiNbO_3$, a lot of researchers use a prism shape of $LiNbO_3$ with tilted pulse front excitation. However, high dispersion and absorption inside the $LiNbO_3$ prism broadens the pulse duration and limits the spectra of the generated radiation. In addition, lack of high frequency components induces a large spot size at the focus, and this works as a

disadvantage in producing high THz fields. In addition, a large sized prism is necessary for scalable THz generation, but its fabrication is not easy.

In order to make an energy scalable THz emitter, we design contact gratings on the first surface of a $LiNbO_3$ crystal as shown in Figure 6.2. Figure 6.2 is our proposed design of contact gratings on the surface of a $LiNbO_3$ crystal. A normal incident 800 nm laser beam is diffracted by the grooves and tilted at a favorable phase matching angle (63.4 degree for 1 THz). The main advantage of this scheme lies on simplicity and energy scalability. The optimal fluence for THz generation in $LiNbO_3$ is ~0.03 J/cm^2 (see Chapter 5). So a 3"-diamter $LiNbO_3$ wafer, currently available, can handle input laser energy up to 10 J. Also, since this method is similar to the tilted pulse front method using a $LiNbO_3$ prism, we anticipate high conversion efficiency ($>10^{-3}$) and high field strengths (> 100 MV/ cm) when 1 J of laser input energy is applied. Petawatt (PW) laser can result in tens of mJ THz radiation. However, our preliminary finite-difference time-domain (FDTD) simulation shows that the diffraction efficiency into $m = \pm 1$ becomes extremely low (<6%) when the diffraction angle is forced to be 64°. This angle of diffraction is necessary for efficient THz generation at 1 THz, but this diffraction condition makes the groove spacing extremely small (two times less than the incident laser wavelength). This drops the diffraction efficiency greatly.

An alternative method is also proposed to improve the diffraction efficiency (see Fig. 6.2). Instead of the contact gratings, periodic prism-like mirrors are fabricated on the surface of $LiNbO_3$. The incident laser beam is split and reflected by the cleaved surface via total internal reflection at an angle of 64°. As each beamlet is smaller than the expected THz wavelength (1 THz = 300 μm), the THz radiation emitted from each

beamlet is coherent and all phased matched in the forward direction. This is analogous to optical Cherenkov radiation. Because of the geometry necessary to produce a large diffraction angle (64°), there is an inherent laser energy loss (~50%) in this scheme. However, this value is significantly larger than 6% predicted with the contact grating design. One disadvantage, however, is related to its fabrication because $LiNbO_3$ is not easy to machine. We are considering both femtosecond laser microfabrication and precision CNC (Computer Numerical Control) machining to fabricate such microstructures on the surface of a large (3") diameter $LiNbO_3$ wafer. This method can produce scalable THz energy and potentially generate tens to hundreds of mJ of THz radiation with a sub-picosecond PW laser.

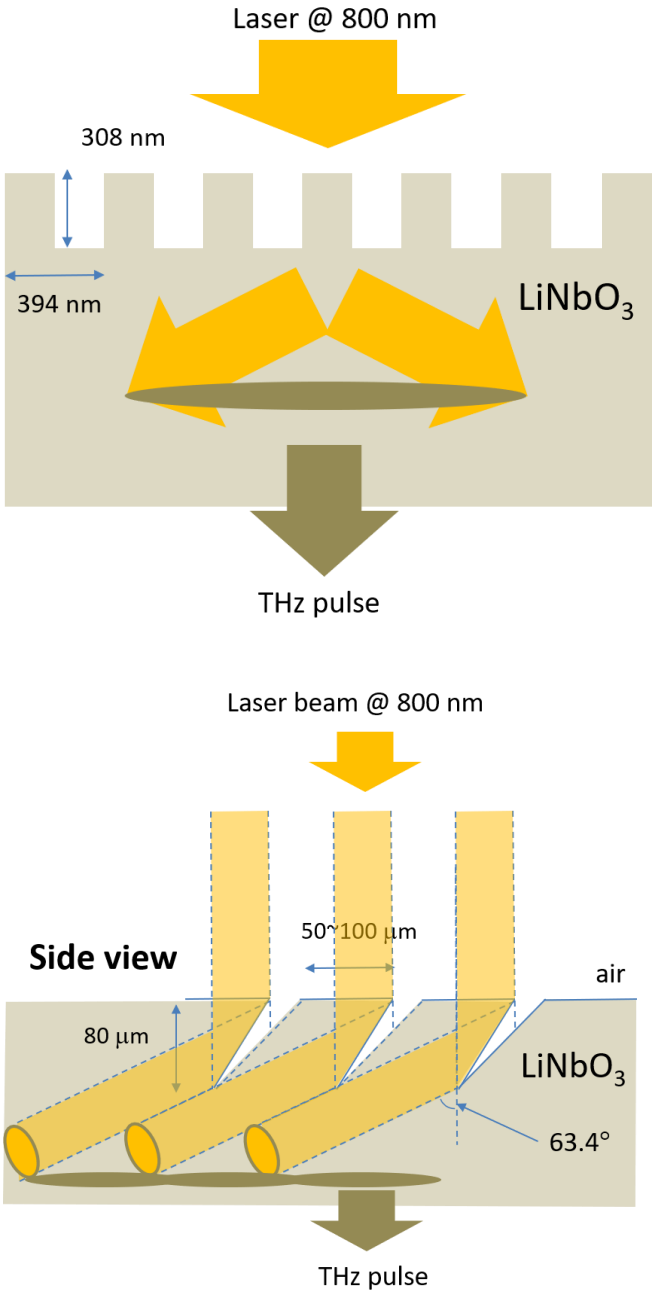

Figure 6.2 Proposed design of contact grating for intense THz generation in optical rectification inside planar $LiNbO_3$

Appendix A : Uncooled microbolometer camera and real-time data taking software

A.1 Introduction to microbolometer

The imaging system used in this dissertation is based on an uncooled microbolometer camera (tau2) made by FLIR which is shown in Figure A.1.1 (c). A microbolometer is a focal plane array (FPA) consisting of many pixel-sized sensors to obtain 2-D thermal information. Figure A.1(a) shows a cross-sectional diagram of one pixel. As we can see from the figure, the absorbing material is the first element for detecting incident thermal radiation. Typically, Vanadium Oxide (VOx) or amorphous silicon is widely used for the absorbing materials, and tau2 is based on Vanadium Oxide. When heated by thermal radiation, the resistance in the absorbing material changes, and this material is connected, through the metal leg, to the bottom layer (silicon substrate) which has a readout integrated circuit (ROIC). A reflector (metal mirror) is placed beneath the absorbing material (VOx) to redirect the radiation which pass through the absorbing material and maximize absorption as much as possible. In addition, a sacrificial layer is deposited to generate a gap to thermally isolate the absorbing material from the ROIC. In summary, thermal radiation heats up the absorbing material, simultaneously changing the resistance of the absorbing material. This change is measured by the ROIC.

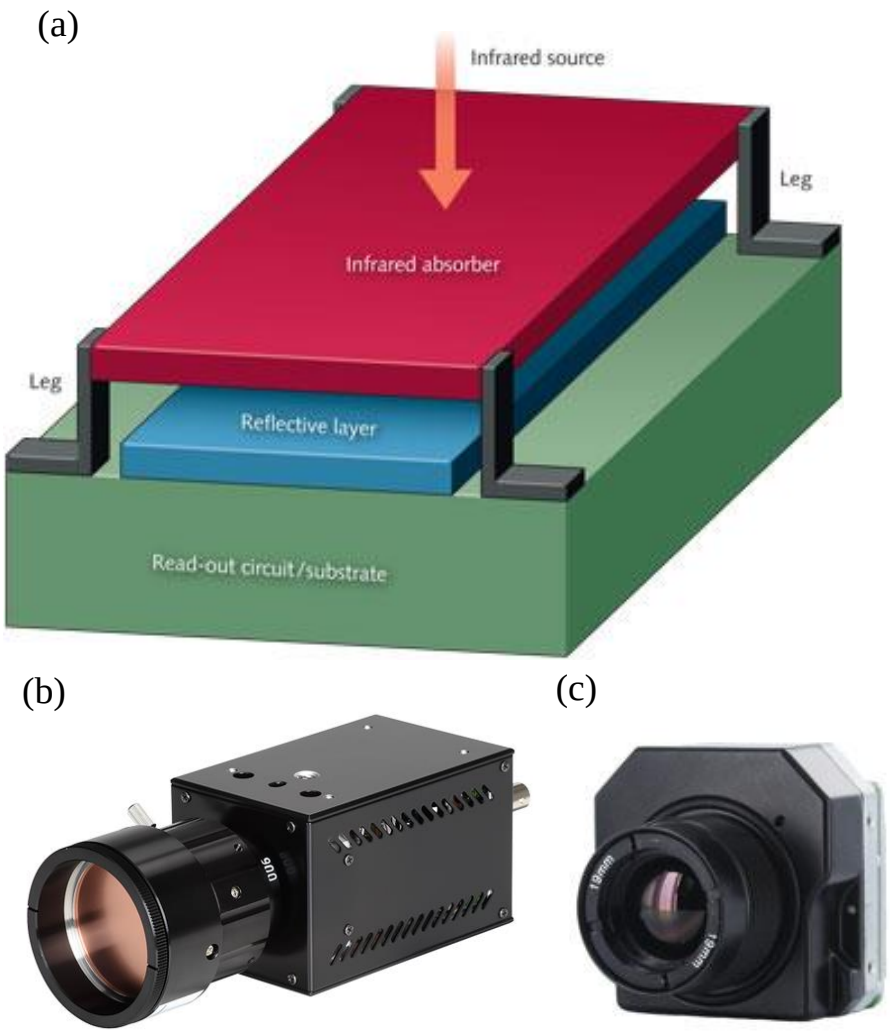

Figure A.1 (a) Diagram of typical microbolometer pixel system consisting of an infrared absorber, reflective layer, leg, and read-out circuit/substrate. (b) THz camera manufactured by NEC. (c) The microbolometer camera (Tau 2, FLIR) used in this dissertation.

With a special coating on the IR absorber, one can optimize thermal absorption at the THz range (1~3 THz). This kind of camera is already developed by a Japanese company NEC, and it is shown in Figure A.1 (b). However, because of this special coating the camera costs a lot (>$50,000). Here we use a cost-effective microbolometer camera (FLIR, tau2) which does not have any special coating for better absorption at THz frequencies. To test if this camera can be used for THz detection, we have

measured its spectral response by using THz bandpass filters. Here we used a pyro-electric detector as a calibration reference because it a flat spectral response curve over the entire THz region.

Figure A.2 shows our measured response curve (blue line with crosses) along with the spectral response characterized by the manufacturing company of the microbolometer, FLIR (red dashed line). Here our measured value is set to be matched with the FLIR data at ~30 THz. The low frequency response around 1~3 THz shows higher values than at 6 THz, and this is attributed to a non-flat spectral response at low frequencies in pyroelectric detection.

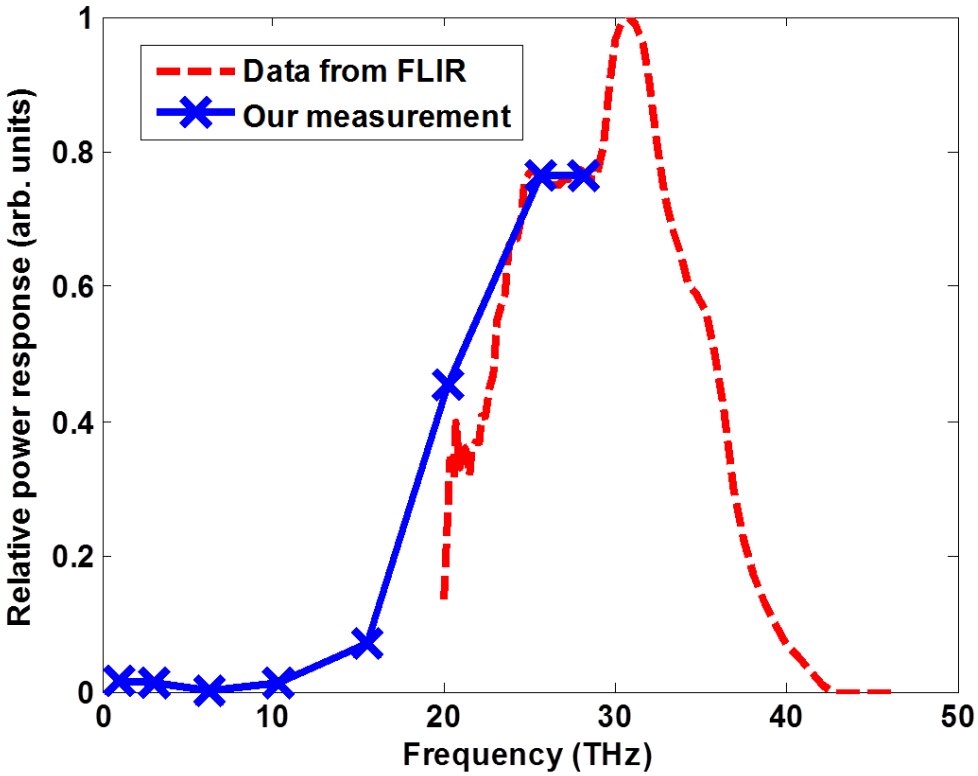

Figure A.2 Spectral response of the microbolometer used in this experiment, measured by a combination of pyroelectric and

microbolometer detection using THz bandpass filters (blue line with crosses) and separately obtained from the FLIR website (red dashed line).

A.2 Real-time data taking

In this section, we introduce a software program for real-time data taking with our microbolometer camera (FLIR, tau2). Tau 2 is provided with its own GUI program for data taking. With this GUI program, it is possible to obtain two different types of data (8-bit bitmap image file and 14-bit raw data file) by its image capturing function. However, this GUI program is not user friendly. The GUI program itself does not provide any real time monitoring system, and there is no way to check the quality of 14-bit data while capturing the image. Also, it takes a long time (> 30 seconds) to capture, retrieve and save a single image with the provided GUI program. Furthermore, it does not provide any multiple snapshot function as well. Therefore, there is a need to develop our own software and user-friendly GUI for fast data saving, real-time monitoring and multiple snapshots. For this, we use a camera link cable for fast communication between the camera and the PC. And, for programmable control, we use a PCIe-frame grabber along with this camera-link communication.

This GUI consists of three windows (Preview, Display, and Control Windows) as shown in Figure A.3. First, the Preview Window is the one with the black screen with a blinking green line. This window displays the 2-D data with real-time streaming, and the green line is the position where we choose a lineout for display. To change the position of the lineout, we can click on the position of interest inside the black screen, and then the green line will be moved to the new position. The display window will show the lineout of the new position from then.

Display Window is the one right below the Preview Window. This window consists of two real-time graphs. The left one is a real-time lineout of the region that green line indicates, and the right one displays the maximum value in the lineout as a function of time. So, we can monitor the trend of intensity variations at the line of interest both in spatially and temporally. Also, at the top of the window, current maximum intensity values and the largest maximum intensity values up to current are displayed and compared. So, this is very useful to check THz intensity variations in time and space.

The last window is Control Window. We can set and clear the parameter values for the experiment and can also save the image data as a MATLAB data file. When we press the save button, then the position value, laser energy, date you measured, and the time you saved the data are all included in the file name. Therefore, we can easily find out the latest data and/or organize the data in order of time. In addition, we can set the number of frames for taking and it is possible to take multiple shots by one click. When data is saved, the newly generated file name is displayed on the command prompt

(a)

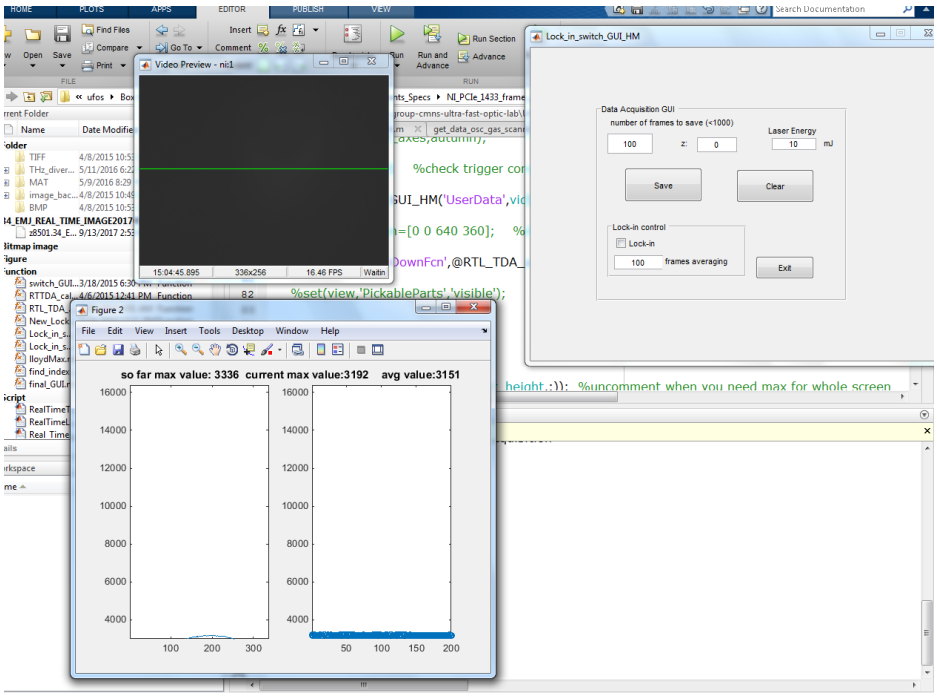

(b)

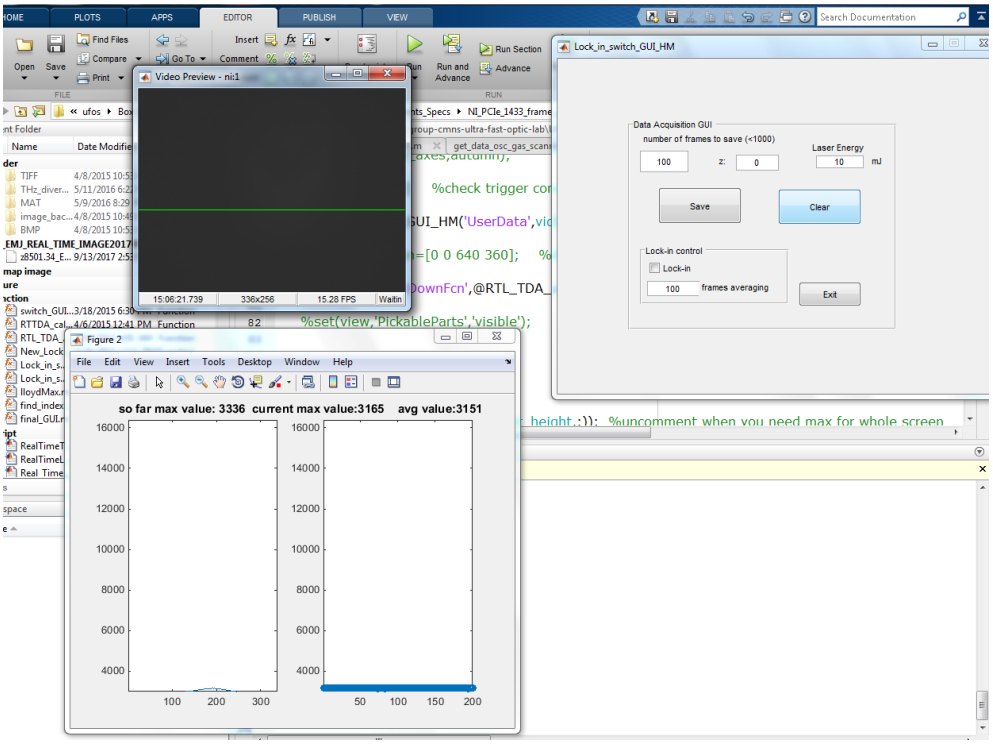

Figure A.3 Real time data taking mode with different lineout position. ((a) center of the image and (b) lower part of the image)

A.3 Real-Time Lock-in Imaging

Figure A.4(a) shows our schematic of implemented lock-in imaging. The 1-kHz trigger signal generated from the laser is divided to produce a 30-Hz signal by a frequency divider. The divided signal is fed into the optical chopper and the frame grabber. The chopper blocks and unblocks the THz beam at 10 Hz, and the frame grabber captures 20 frames per second. This provides 10 pairs of blocked and unblocked images per second, and then the difference images (14-bit, 336 × 256 pixels, 17 μm pitch) are computed and averaged for a variable period (0.1~1 second), and displayed for real-time THz imaging. For example, Figure A.4(b) shows a raw image obtained without lock-in detection, whereas Figure A.4(c) shows an image averaged over 100 frames with lock-in detection. This lock-in method greatly improves the signal-to-noise ratio in characterizing low energy THz beams, in particular, at low THz frequencies.

(a)

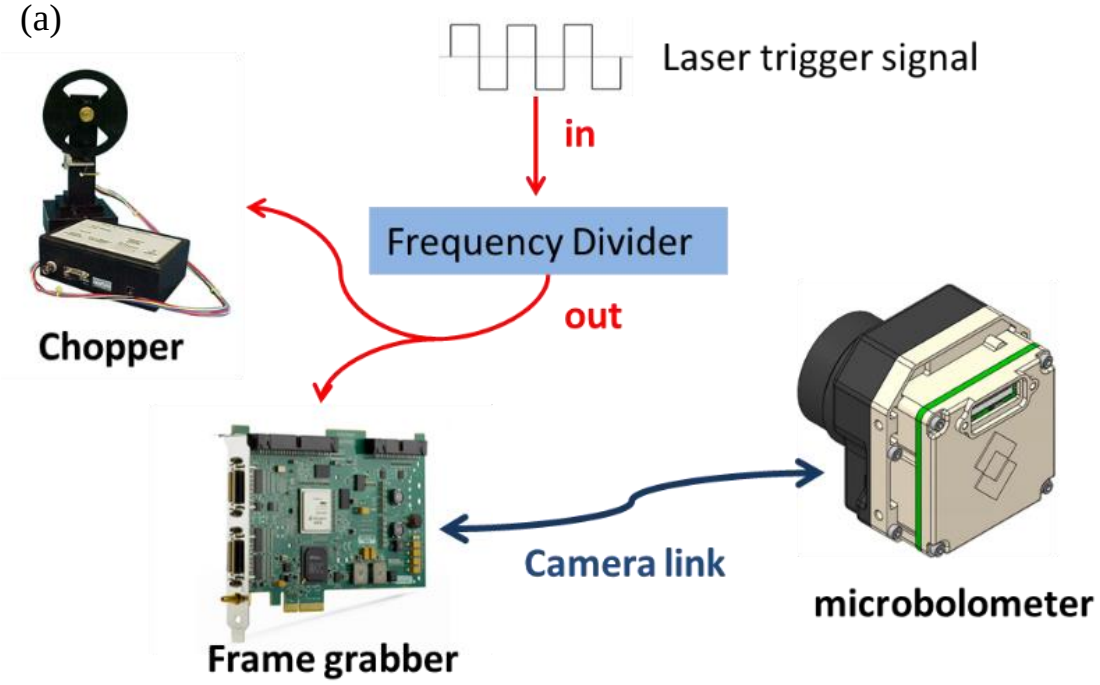

(b) (c)

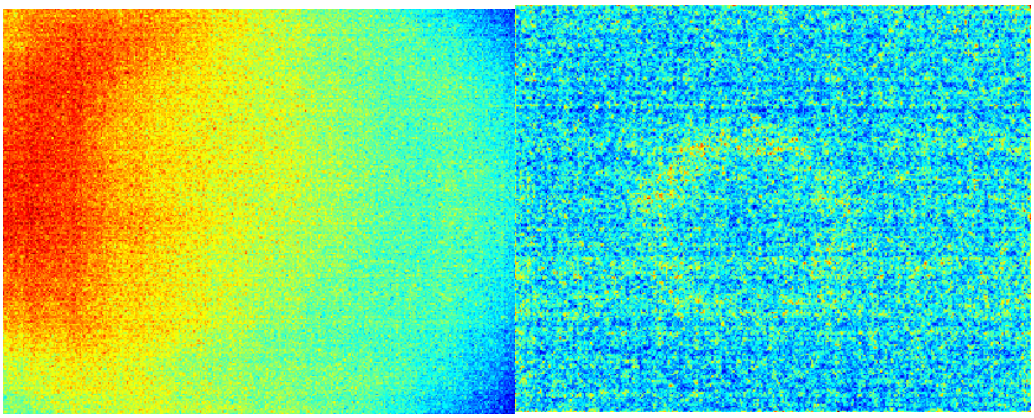

Figure A.4 (a) Schematic of real-time THz lock-in imaging. (b) THz beam profile obtained without lock-in imaging, dominated by strong background thermal radiation. (c) Image obtained by averaging 100 frames with lock-in under the same laser condition as in (b)

Figure A.5 shows our GUI software for real-time lock-in imaging. Once the Lock-in check box inside the lock-in control panel is checked, the mode changes from real-time data taking to lock-in imaging. In the lock-in imaging mode, different from the real-time data taking mode, the Preview Window is totally disabled and the blinking green line for lineout selection disappears. Therefore, 1D information such as line-out is no more available in the lock-in imaging mode. Instead, two different 2D-images will be showed in the Display Window. One is the raw data which is the first frame image taken by the microbolometer, and the other is the averaged data obtained with a lock-in imaging algorithm. The number of frames for averaging can be set once we type and hit ENTER on the text box which is located inside the lock-in control panel. Whenever a new value is updated, the microbolometer dumps the existing data inside the buffer and starts taking new data and applying its lock-in imaging algorithm with newly updated average frame numbers. In Figure A.5, the left image in the display window is the final processed data and the right one is the first raw image data taken

from the microbolometer. Here, the order of image can be swapped according to the varying trigger timing. Therefore, left image does not always have to be the final processed image. This can go to the right side and the raw image data can come to the left.

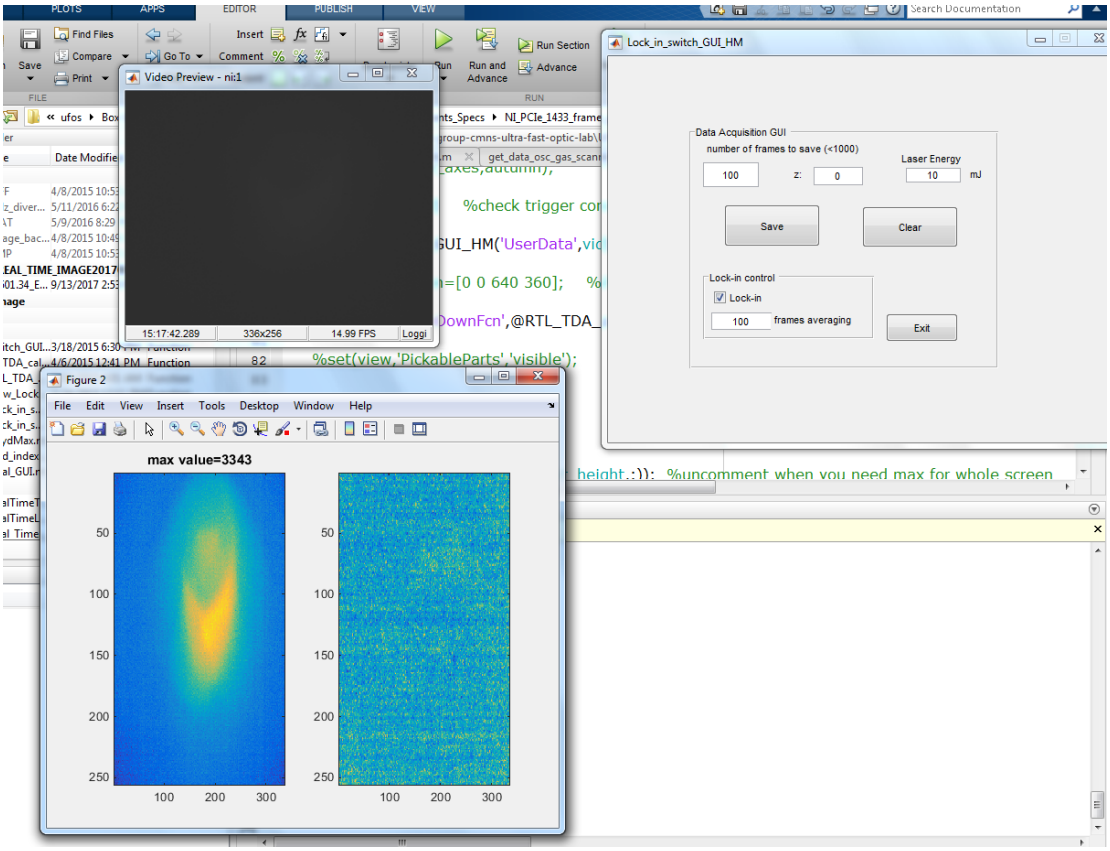

Figure A.5 Screen capture of software program for real-time lock-in imaging mode. Black screen on the top is disabled Preview Window. The one at the bottom is the Display Window. This shows a locked-in image (left) and the snapshot of the first raw image when the trigger signal is applied (right). It also shows the maximum value from the raw image data as well. The window on the top right is the Control Window which can save images and adjust the averaging number of frames.

Appendix B : Spectrum calibration with THz bandpass filters

B.1 Introduction to THz bandpass filter

Terahertz bandpass filters can be used for spectral measurements. These filters provide high-spectral-resolution filtering at various center frequencies ranging from 0.5 to 30 THz. With decent transmission at the center frequency (> 85%), these filters are fabricated from gold-mesh frequency-selective surfaces designed to reject out-of-band radiation primarily by reflection and destructive interference [7]. Figure B.1 (a) shows a typical structure of THz bandpass filter. The cross-absent pattern of these filters is a continuous mesh with a pattern of crosses etched away from the gold layer using photolithography. While a simple wire-grid mesh acts as a shortpass filter, blocking radiation with wavelengths larger than the grid size, the cross-absent mesh selects a specific band of wavelengths [7].

However, due to imperfect fabrication, each THz bandpass filter contains its unwanted transmission at the stopband as shown from Figure B.1 (b). Since the passband is much narrower than the stop band, energy passed through the stop band can not be ignored once accumulated over the broad range. Therefore, for the correct spectrum characterization, we need a calibration method to compensate the unwanted

transmission from the broad range of stop band.

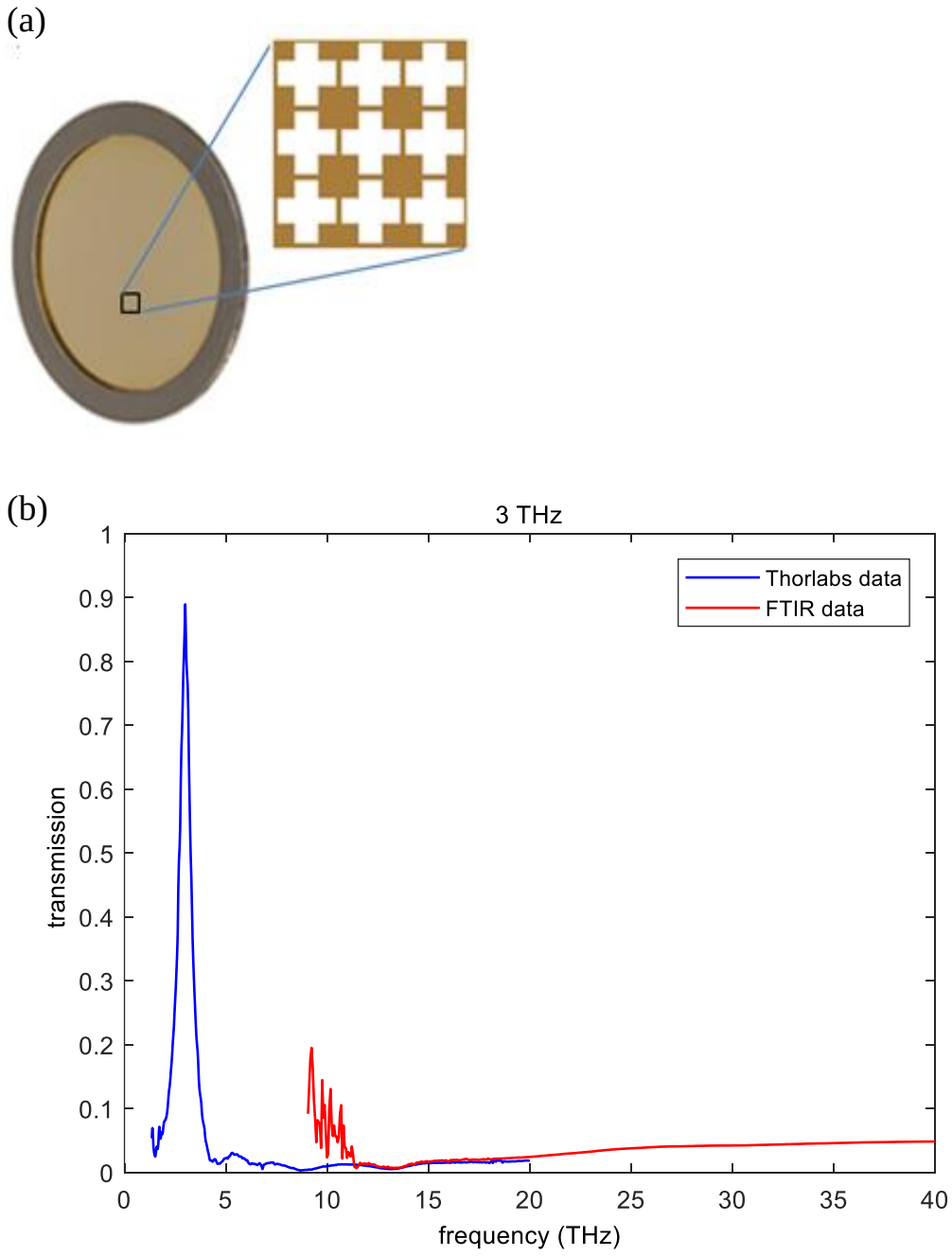

Figure B.1 (a) Typical structure of gold-mesh THz band pass filter. The size of the cross patterns and the gap between the patterns determines the central frequency, bandwidth, and the stopband frequency. (b) THz transmission curve for 3 THz bandpass filter. Blue line is the data provided by the vendor (Thorlabs) and red line is the extension by our FTIR measurement data

B.2 Spectrum calculation with THz bandpass filter along with pyro-electric detector

For spectrum characterization we use 15 bandpass filters along with our pyro-electric detector. As we can see from Fig. B.2 (a), most of the range of our interest (0~40 THz) can be covered by combination of 15 sets of filters. For the higher frequency components, we can cut-off and ignore them by placing the long pass filter in front of the THz bandpass filters. The long pass filter is a specially coated Ge filter which is designed for cut-offing high frequency components (>40 THz).

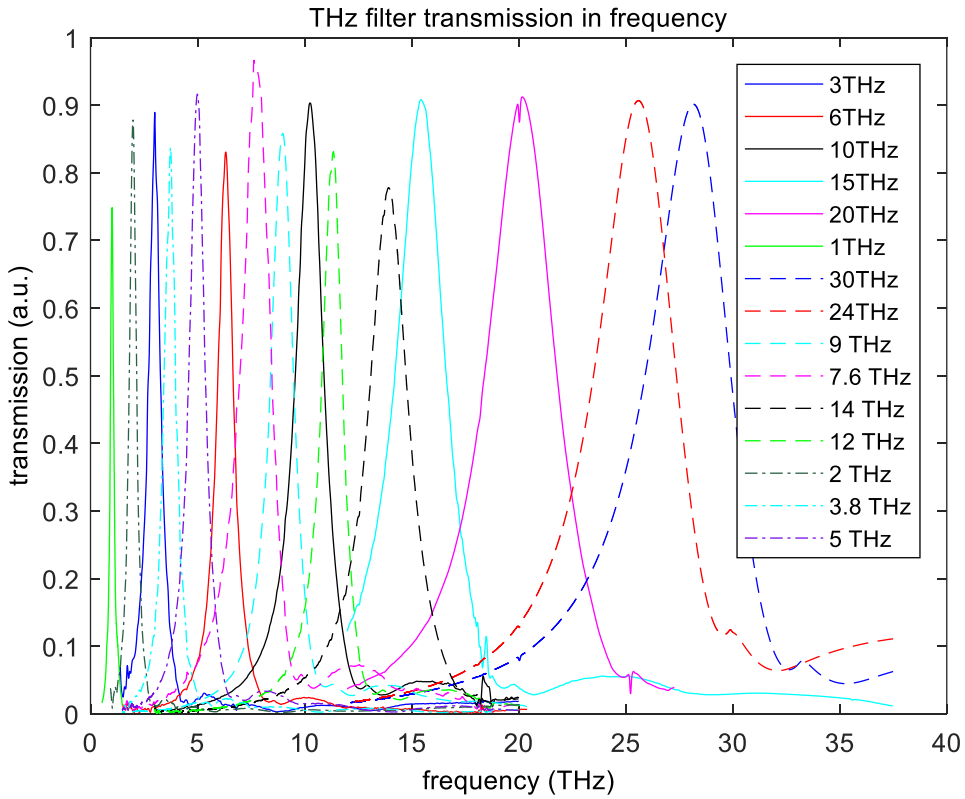

Figure B.2 Spectrum plots of 15 THz bandpass filters we use for the experiment. All together can cover 0~ 40 THz.

However, as mentioned in the previous section, each THz filter has its own undesirable transmission at the stop band and it is quite difficult to eliminate this

component by placing additional filters. Therefore, in this chapter, we propose two different ways of compensating the unwanted transmission over the stop band. In the first method, called the zeroth order approach because of its simplicity, we measure a pyro electric voltage V_k with a THz bandpass filter centered at frequency k. The spectrum at k (S_k) is proportional to V_k. For a given S_k, the value of V_k becomes large when the transmission area, height (h_k) × width (w_k), of the filter gets large. Therefore, we can estimate that S_k is inverse proportional to h_k and w_k as $S_k \propto \frac{V_k}{h_k w_k}$. In this zeroth order method, we can characterize the relative transmission spectral power at frequency k by dividing V_k with h_k, and w_k.

The second method involves a matrix to solve an inverse problem. In this method, we divide the whole spectrum range (0~40 THz) into 15 bins, where each bin corresponds to each filter. For filter i, the transmission at frequency at j is given by A_{ij}, which is related to V_k and S_k as follows.

$$\begin{bmatrix} V_1 \\ \vdots \\ V_{15} \end{bmatrix} = \begin{bmatrix} A_{1,1} & \cdots & A_{1,15} \\ \vdots & \ddots & \vdots \\ A_{15,1} & \cdots & A_{15,15} \end{bmatrix} \begin{bmatrix} S_1 \\ \vdots \\ S_{15} \end{bmatrix}$$

We can get the spectrum S_k by applying the inverse of the matrix to the left hand side (measured V_k). Sometimes negative S_k values can be retrieved while solving an inverse matrix equation. In practice, those negative values can be approximated to be zero.

Bibliography

1. G. A. Mourou, C. P. J. Barry, and M. D. Perry, "Ultrahigh-Intensity Lasers: Physics of the Extreme on a Tabletop," Physics Today **51**, 22–28 (1998).
2. C. Rulliere, *Femtosecond Laser Pulses - Principles and Experiments, 2nd* ed. (Springer, USA, 2005).
3. I.F. Akyildiz, J.M. Jornet, C. Han, "Terahertz band: Next frontier for wireless communications", Physical Communication, **12**, 16-32 (2014)
4. H. Hirori , A. Doi , F. Blanchard , and K. Tanaka , "Single-cycle terahertz pulses with amplitude exceeding 1 MV/cm generated by optical rectification in LiNbO3",Appl. Phys. Lett. **98**, 091106 (2011).
5. Mostafa Shalaby, Carlo Vicario, Karunanithi Thirupugalmani, Srinivasan Brahadeeswaran, and Christoph P. Hauri , "Intense THz source based on BNA organic crystal pumped at Ti:sapphire wavelength ",Optics. Lett. **41**, 001777 (2016)
6. S. G. Ganichev and W. Prettl, *Intense Terahertz Excitation of Semiconductors* (Oxford University Press, USA, 2006).
7. Y.-S. Lee, *Principles of Terahertz Science and Technology*, 1st ed. (Springer, USA, 2008).
8. BR Labs, http://www.br-labs.com/divisions/terahertz/.
9. M. Tonouchi, “Cutting-edge terahertz technology,” Nat. Photon **1**, 97–105 (2007).
10. D. Grischkowsky, S. Keiding, M. van Exter, and C. Fattinger, "Far-infrared time-domain spectroscopy with terahertz beams of dielectrics and semiconductors," J. Opt. Soc. Am. B **7**, 2006–2015 (1990).
11. MPSD-CMD, http://mpsd-cmd.cfel.de/research-met-thz-intensethz.html.
12. B. B. Hu and M. C. Nuss, "Imaging with terahertz waves," Opt. Lett. **20**, 1716–1718 (1995).

13. K. Kawase, Y. Ogawa, Y. Watanabe, and H. Inoue, "Non-destructive terahertz imaging of illicit drugs using spectral fingerprints," Opt. Express **11**, 2549–2554 (2003).
14. J. B. Jackson, M. Mourou, J. F. Whitaker, I. N. Duling III, S. L. Williamson, M. Menu, and G. A. Mourou, "Terahertz imaging for non-destructive evaluation of mural paintings," Opt. Comm. **281**, 527–532 (2008).
15. H. Hamster, A. Sullivan, S. Gordon, W. White, and R. W. Falcone, "Subpicosecond, electromagnetic pulses from intense laser-plasma interaction," Phys. Rev. Lett. **71**, 2725 (1993).
16. W. P. Leemans, C. G. R. Geddes, J. Faure, C. Tóth, J. Van Tilborg, C. B. Schroeder, E. Esarey, G. Fubiani, D. Auerbach, B. Marcelis, M. A. Carnahan, R. A. Kaindl, J. Byrd, and M. C. Martin, "Observation of terahertz emission from a laser-plasma accelerated electron bunch crossing a plasma-vacuum boundary.," Phys. Rev. Lett. **91**, 074802 (2003).
17. J. Hebling, K.-L. Yeh, M. C. Hoffmann, B. Bartal, and K. A. Nelson, "Generation of high-power terahertz pulses by tilted-pulse-front excitation and their application possibilities," J. Opt. Soc. Am. B **25**, B6–B19 (2008).
18. M. C. Hoffmann, J. Hebling, H. Y. Hwang, K.-L. Yeh, and K. A. Nelson, "THz-pump/THz-probe spectroscopy of semiconductors at high field strengths [Invited]," J. Opt. Soc. Am. B **26**, A29–A34 (2009).
19. P. Gaal, K. Reimann, M. Woerner, T. Elsaesser, R. Hey, and K. H. Ploog, "Nonlinear Terahertz Response of n-Type GaAs," Phys. Rev. Lett. **96**, 187402 (2006).
20. Y. Shen, T. Watanabe, D. A. Arena, C.-C. Kao, J. B. Murphy, T. Y. Tsang, X. J. Wang, and G. L. Carr, "Nonlinear Cross-Phase Modulation with Intense Single-Cycle Terahertz Pulses," Phys. Rev. Lett. **99**, 043901 (2007).
21. J. Hebling, K.-L. Yeh, K. A. Nelson, and M. C. Hoffmann, "High-Power THz Generation, THz Nonlinear Optics, and THz Nonlinear Spectroscopy," IEEE Journal of Selected Topics in Quantum Electronics **14**, 345 –353 (2008).
22. M. C. Hoffmann, N. C. Brandt, H. Y. Hwang, K.-L. Yeh, and K. A. Nelson, "Terahertz Kerr effect," Appl. Phys. Lett. **95**, 231105 1–3 (2009).

23. G. L. Carr, M. C. Martin, W. R. McKinney, K. Jordan, G. R. Neil, and G. P. Williams, "High-power terahertz radiation from relativistic electrons," Nature **420**, 153–156 (2002).
24. A. Sell, A. Leitenstorfer, and R. Huber, "Phase locked generation and field-resolved detection of widely tunable terahertz pulses with amplitudes exceeding 100 MV/cm" ,Opt. Lett. 33, 2767 (2008)..
25. O. Schubert, M. Hohenleutner, F. Langer, B. Urbanek, C. Lange, U. Huttner, D. Golde, T. Meier, M. Kira, S. W. Koch, and R. Huber, "sub-cycle control of terahertz high-harmonic generation by dynamical Bloch oscillations",Nature Photon. 8, 119 (2014).
26. Z. Wu, A. S. Fisher, J. Goodfellow, M. Fuchs, D. Daranciang, M. Hogan, H. Loos, and A. Lindenberg, " Intense terahertz pulses from SLAC electron beams using coherent transition radiation",Rev. Sci. Instrum. 84, 022701 (2013)..
27. A. G. Stepanov, S. Henin, Y. Petit, L. Bonacina, J. Kasparian, and J.-P. Wolf, "Erratum to: Mobile source of high-energy single-cycle terahertz pulses" Appl. Phys. B 115, 293 (2014).
28. S. L. Dexheimer, *Terahertz Spectroscopy: Principles and Applications*, 1st ed. (CRC Press, 2007).
29. J. A. Fülöp, L. Pálfalvi, S. Klingebiel, G. Almási, F. Krausz, S. Karsch, and J. Hebling, "Generation of sub-mJ terahertz pulses by optical rectification," Opt. Lett. **37**, 557–559 (2012).
30. E. Matsubara, M. Nagai, and M. Ashida, "Ultrabroadband coherent electric field from far infrared to 200 THz using air plasma induced by 10 fs pulses," Appl. Phys. Lett. **101**, 011105 1–4 (2012).
31. D. J. Cook and R. M. Hochstrasser, "Intense terahertz pulses by four-wave rectification in air," Opt. Lett. **25**, 1210–1212 (2000).
32. T. Bartel, P. Gaal, K. Reimann, M. Woerner, and T. Elsaesser, "Generation of single-cycle THz transients with high electric-field amplitudes," Opt. Lett. **30**, 2805–2807 (2005).
33. M. Kresz, T. Loffler, M. D. Thomson, R. Dorner, H. Gimpel, K. Zrost, T. Ergler, R. Moshammer, U. Morgner, J. Ullrich, and H. G. Roskos,

"Determination of the carrier-envelope phase of few-cycle laser pulses with terahertz-emission spectroscopy," Nat Phys **2**, 327–331 (2006).

34. M. Kress, T. Löffler, S. Eden, M. Thomson, and H. G. Roskos, "Terahertz-pulse generation by photoionization of air with laser pulses composed of both fundamental and second-harmonic waves," Opt. Lett. **29**, 1120–1122 (2004).
35. X. Xie, J. Dai, and X.-C. Zhang, "Coherent Control of THz Wave Generation in Ambient Air," Phys. Rev. Lett. **96**, 075005 (2006).
36. Y. Chen, M. Yamaguchi, M. Wang, and X.-C. Zhang, "Terahertz pulse generation from noble gases," Appl. Phys. Lett. **91**, 251116 1–3 (2007).
37. J. Dai, N. Karpowicz, and X.-C. Zhang, "Coherent Polarization Control of Terahertz Waves Generated from Two-Color Laser-Induced Gas Plasma," Phys. Rev. Lett. **103**, 023001 (2009).
38. H. Wen and A. M. Lindenberg, "Coherent Terahertz Polarization Control through Manipulation of Electron Trajectories," Phys. Rev. Lett. **103**, 023902 (2009).
39. F. Blanchard, G. Sharma, X. Ropagnol, L. Razzari, R. Morandotti, and T. Ozaki, "Improved terahertz two-color plasma sources pumped by high intensity laser beam," Opt. Express **17**, 6044–6052 (2009).
40. G. Rodriguez and G. L. Dakovski, "Scaling behavior of ultrafast two-color terahertz generation in plasma gas targets: energy and pressure dependence," Opt. Express **18**, 15130–15143 (2010).
41. T.-J. Wang, J.-F. Daigle, Y. Chen, C. Marceau, F. Théberge, M. Châteauneuf, J. Dubois, and S. l. Chin, "High energy THz generation from meter-long two-color filaments in air," Laser Phys. Lett. **7**, 517–521 (2010).
42. T.-J. Wang, C. Marceau, S. Yuan, Y. Chen, Q. Wang, F. Théberge, M. Châteauneuf, J. Dubois, and S. l. Chin, "External focusing effect on terahertz emission from a two-color femtosecond laser-induced filament in air," Laser Phys. Lett. **8**, 57–61 (2011).
43. F. Blanchard, G. Sharma, L. Razzari, X. Ropagnol, H.-C. Bandulet, F. Vidal, R. Morandotti, J.-C. Kieffer, T. Ozaki, H. Tiedje, H. Haugen, M. Reid, and F.

Hegmann, "Generation of Intense Terahertz Radiation via Optical Methods," IEEE Journal of Selected Topics in Quantum Electronics **17**, 5–16 (2011).

44. M. C. Hoffmann and J. A. Fülöp, "Intense ultrashort terahertz pulses: generation and applications," Journal of Physics D: Applied Physics **44**, 083001 (2011).
45. Jianming Dai, B. Clough, I-Chen Ho, Xiaofei Lu, Jingle Liu, and Xi-Cheng Zhang, "Recent Progresses in Terahertz Wave Air Photonics," IEEE Transactions on Terahertz Science and Technology **1**, 274–281 (2011).
46. Y. Minami, T. Kurihara, K. Yamaguchi, M. Nakajima, and T. Suemoto, "High-power THz wave generation in plasma induced by polarization adjusted two-color laser pulses," Appl. Phys. Lett. **102**, 041105–1–4 (2013).
47. K.-Y. Kim, J. H. Glownia, A. J. Taylor, and G. Rodriguez, "Terahertz emission from ultrafast ionizing air in symmetry-broken laser fields," Opt. Express **15**, 4577–4584 (2007).
48. K.-Y. Kim, A. J. Taylor, J. H. Glownia, and G. Rodriguez, "Coherent control of terahertz supercontinuum generation in ultrafast laser-gas interactions," Nat Photon **2**, 605–609 (2008).
49. K.-Y. Kim, "Generation of coherent terahertz radiation in ultrafast laser-gas interactions," Phys. Plasmas **16**, 056706 (2009).
50. K.-Y. Kim, J. H. Glownia, A. J. Taylor, and G. Rodriguez, "High-Power Broadband Terahertz Generation via Two-Color Photoionization in Gases," IEEE Journal of Quantum Electronics **48**, 797 –805 (2012).
51. T. I. Oh, Y. S. You, and K. Y. Kim, "Two-dimensional plasma current and optimized terahertz generation in two-color photoionization," Opt. Express **20**, 19778–19786 (2012).
52. Y. S. You, T. I. Oh, and K. Y. Kim, "Off-Axis Phase-Matched Terahertz Emission from Two-Color Laser-Induced Plasma Filaments," Phys. Rev. Lett. **109**, 183902 (2012).
53. Y. S. You, T. I. Oh, and K.-Y. Kim, "Mechanism of elliptically polarized terahertz generation in two-color laser filamentation," Opt. Lett. **38**, 1034–1036 (2013).

54. T. I. Oh, Y. S. You, and K.-Y. Kim, “Scaling and Saturation of High-Power Terahertz Radiation Generation in Two-Color Laser Filamentation,” Appl. Phys. Lett. **102,** 201113 (2013).
55. K.-Y. Kim, Ph.D. Dissertation, “Measurement of ultrafast dynamics in the interaction of intense laser pulses with gases, atomic clusters, and plasmas,” University of Maryland (2003).
56. M. V. Ammosov, N. B. Delone, and V. P. Kraĭnov, "Tunnel ionization of complex atoms and of atomic ions in an alternating electromagnetic field," Soviet Physics - JETP **64**, 1191–1194 (1986).
57. V. S. Popov, "Tunnel and multiphoton ionization of atoms and ions in a strong laser field (Keldysh theory)," Phys.-Usp. **47**, 855 (2004).
58. T. I. Oh, Y. S. You, N. Jhajj, E. Rosenthal, H. M. Milchberg, and K. Y. Kim, "Intense terahertz generation in two-color laser filamentation: energy scaling with terawatt laser systems", New J. Phys. 15, 075002 (2013).
59. G. Rodriguez, A. R. Valenzuela, B. Yellampalle, M. J. Schmitt, and K.-Y. Kim, "In-line holographic imaging and electron density extraction of ultrafast ionized air filaments," J. Opt. Soc. Am. B **25**, 1988–1997 (2008).
60. X. Lu and X.-C. Zhang, "Generation of Elliptically Polarized Terahertz Waves from Laser-Induced Plasma with Double Helix Electrodes," Phys. Rev. Lett. **108**, 123903 (2012).
61. V. B. Gildenburg and N. V. Vvedenskii, "Optical-to-THz Wave Conversion via Excitation of Plasma Oscillations in the Tunneling-Ionization Process," Phys. Rev. Lett. **98**, 245002 (2007).
62. T. -J. Wang, C. Marceau, S. Yuan, Y. Chen, Q. Wang, F. Theberge, M. Chateauneuf, J. Dubois, S. L. Chin, “External focusing effect on terahertz emission from a two-color femtosecond laser-induced filament in air,” *Laser Phys. Lett*, vol. 8, no. 1, pp. 57–61, (2011).
63. A. A. Silaev and N. V. Vvedenskii, "Residual-Current Excitation in Plasmas Produced by Few-Cycle Laser Pulses," Phys. Rev. Lett. **102**, 115005 (2009).
64. A. Couairon and A. Mysyrowicz, "Femtosecond filamentation in transparent media," Physics Reports **441**, 47–189 (2007).

65. S. L. Chin, T.-J. Wang, C. Marceau, J. Wu, J. S. Liu, O. Kosareva, N. Panov, Y. P. Chen, J.-F. Daigle, S. Yuan, A. Azarm, W. W. Liu, T. Seideman, H. P. Zeng, M. Richardson, R. Li, and Z. Z. Xu, "Advances in intense femtosecond laser filamentation in air," Laser Phys. **22**, 1–53 (2012).
66. G. Fibich and A. L. Gaeta, "Critical power for self-focusing in bulk media and in hollow waveguides",Opt. Lett. 25, 335 (2000).
67. J. K. Wahlstrand, Y.-H. Cheng, and H. M. Milchberg, "Absolute measurement of the transient optical nonlinearity in N_2, O_2, N_2O and Ar", Phys. Rev. A 85, 043820 (2012)
68. T. D. Grow and A. L. Gaeta, "Dependence of multiple filamentation on beam ellipticity", Opt. Express 13, 4594 (2005).
69. B. Shim, S. E. Schrauth, L. T. Vuong, Y. Okawachi, and A. L. Gaeta, "Dynamics of elliptical beams in the anomalous group-velocity dispersion regime", Opt. Express 19, 9139 (2011).
70. J. K. Wahlstrand, Y.-H. Cheng, and H. M. Milchberg, "Absolute measurement of the transient optical nonlinearity in N_2, O_2, N_2O, and Ar," Phys. Rev. A **85**, (2012).
71. K.-L. Yeh, M. C. Hoffmann, J. Hebling, and K. A. Nelson, "Generation of 10 μJ ultrashort terahertz pulses by optical rectification," Appl. Phys. Lett. **90**, 171121 1–3 (2007).
72. F. Blanchard, L. Razzari, H. C. Bandulet, G. Sharma, R. Morandotti, J. C. Kieffer, T. Ozaki, M. Reid, H. F. Tiedje, H. K. Haugen, and F. A. Hegmann, "Generation of 1.5 μJ single-cycle terahertz pulses by optical rectification from a large aperture ZnTe crystal," Opt. Express **15**, 13212–13220 (2007).
73. A. G. Stepanov, L. Bonacina, S. V. Chekalin, and J.-P. Wolf, "Generation of 30 μJ single-cycle terahertz pulses at 100 Hz repetition rate by optical rectification," Opt. Lett. **33**, 2497–2499 (2008).
74. H. Zhong, N. Karpowicz, and X.-C. Zhang, "Terahertz emission profile from laser-induced air plasma," Appl. Phys. Lett. **88**, 261103 1–3 (2006).

75. L. Bergé, S. Skupin, C. Köhler, I. Babushkin, and J. Herrmann, "3D Numerical Simulations of THz Generation by Two-Color Laser Filaments," Phys. Rev. Lett. **110**, 073901 (2013).
76. C. D'Amico, A. Houard, M. Franco, B. Prade, A. Mysyrowicz, A. Couairon, and V. T. Tikhonchuk, "Conical Forward THz Emission from Femtosecond-Laser-Beam Filamentation in Air," Phys. Rev. Lett. **98**, 235002 (2007).
77. I. Babushkin, S. Skupin, A. Husakou, C. Köhler, E. Cabrera-Granado, L. Bergé, and J. Herrmann, "Tailoring THz radiation by controlling tunnel photoionization events in gases," New J. Phys. **13** 123029 (2011).
78. S. Hosseini, O. Kosareva, N. Panov, V.P. Kandidov, A. Azarm, J.-F. Daigle, A.B. Savel'ev, T.-J. Wang, and S.L. Chin, Laser Phys. Lett. **9**, 868 (2012)
79. C. Köhler, E. Cabrera-Granado, I. Babushkin, L. Bergé, J. Herrmann, and S. Skupin, "Directionality of terahertz emission from photoinduced gas plasmas," Opt. Lett. **36**, 3166–3168 (2011).
80. Y.-H. Chen, S. Varma, T. M. Antonsen, and H. M. Milchberg, "Direct Measurement of the Electron Density of Extended Femtosecond Laser Pulse-Induced Filaments," Phys. Rev. Lett. **105**, 215005 (2010).
81. K. Y. Kim, V. Kumarappan, and H. M. Milchberg, "Measurement of the average size and density of clusters in a gas jet," Appl. Phys. Lett. **83**, 3210–3212 (2003).
82. V. Blank, M. D. Thomson, and H. G. Roskos, "Spatio-spectral characteristics of ultra-broadband THz emission from two-colour photoexcited gas plasmas and their impact for nonlinear spectroscopy," *New J. Phys.*, vol. 15, no. 7, 075023, (2013).
83. R. W. Boyd, *Nonlinear Optics, Third Edition*, 3rd ed. (Academic Press, 2008).
84. Q. Wu and X.-C. Zhang, "Free-space electro-optic sampling of terahertz beams," Appl. Phys. Lett. **67**, 3523–3525 (1995).
85. J. Dai, X. Xie, and X.-C. Zhang, "Detection of Broadband Terahertz Waves with a Laser-Induced Plasma in Gases," Phys. Rev. Lett. **97**, 103903 (2006).

86. I.-C. Ho, X. Guo, and X.-C. Zhang, "Design and performance of reflective terahertz air-biased-coherent-detection for time-domain spectroscopy," Opt Express **18**, 2872–2883 (2010).
87. J. P. Palastro, T. M. Antonsen, and H. M. Milchberg, "Compression, spectral broadening, and collimation in multiple, femtosecond pulse filamentation in atmosphere," Phys. Rev. A **86**, 033834 (2012).
88. D. Zhang, Z. Lü, C. Meng, X. Du, Z. Zhou, Z. Zhao, and J. Yuan, "Synchronizing Terahertz Wave Generation with Attosecond Bursts," Phys. Rev. Lett. **109**, 243002 (2012).
89. L. A. Johnson, J. P. Palastro, T. M. Antonsen, and K. Y. Kim, **"**THz generation by optical Cherenkov emission from ionizing two-color laser pulses" *Phys. Rev. A*, vol. 88, no. 6, pp. 063804-1–063804-9, (2013).
90. P. Klarskov, A. Strikwerda, K. Iwaszczuk, P. U. Jepsen, "Experimental three-dimensional beam profiling and modeling of a terahertz beam generated from a two-color air plasma", *New J. of Phys.*, vol.15, no. 7, pp. 075012-1–075012-13, 2013.
91. T. I. Oh, Y. J. Yoo, Y. S. You, and K. Y. Kim, "Generation of strong terahertz fields exceeding 8 MV/cm at 1 kHz and real-time beam profiling," *Appl. Phys. Lett.*, vol. 105, no. 4, pp. 041103-1–041103-4, (2014).
92. D. Kuk, Y. J. Yoo, E. W. Rosenthal, N. Jhajj, H. M. Milchberg and K. Y. Kim, "Generation of scalable terahertz radiation from cylindrically focused two-color laser pulses in air," *Appl. Phys. Lett.*, vol. 108, no. 12, pp. 121106-1–121106-5, (2016).
93. Y. J. Yoo, D. Kuk, Z. Zhong, and K. Y. Kim, "Generation and characterization of strong terahertz fields from kHz laser filamentation," IEEE J. Selected Topics in Quantum Electron., vol. 23, pp. 8501007-1/7, (2017).
94. A. Lee, and Q. Hu, "Real-time continuous-wave terahertz imaging by use of a microbolometer focal-plane array," *Opt. Lett.*, vol. 30, no. 19, pp. 2563–2565, (2005).

95. N. Jhajj, Y.-H. Cheng, J. K. Wahlstrand, and H. M. Milchberg, " Optical beam dynamics in a gas repetitively heated by femtosecond filaments", Opt. Express **21**, 28980 (2013).